SLAC-R-483
UC-414

Strange Particle Production in Hadronic Z^0 Decays *

Kenneth G. Baird III

Stanford Linear Accelerator Center
Stanford University
Stanford, California 94309

April 1996

Prepared for the Department of Energy
under contract number DE-AC03-76SF00515

Printed in the United States of America. Available from the National Technical Information Service, U.S. Department of Commerce, 5285 Port Royal Road, Springfield, Virginia 22161.

*Ph.D. thesis, Rutgers University

SLAC-483

Strange Particle Production in Hadronic Z^0 Decays

by Kenneth George Baird III

A dissertation submitted to the

Graduate School— New Brunswick

Rutgers, The State University of New Jersey

in partial fulfillment of the requirements

for the degree of

Doctor of Philosophy

Graduate Program in Physics and Astronomy

Written under the direction of

R.J. Plano

and approved by

_____

_____

_____

_____

_____

New Brunswick, New Jersey

January, 1996

Work supported by Department of Energy contract DE–AC03–76SF00515.

ABSTRACT

A study has been made of neutral strange baryons and pseudoscalar mesons produced in hadronic decays of the weak gauge boson Z^0. The experiment was performed at the Stanford Linear Accelerator Center, which has the unique capability of colliding highly polarized electrons with unpolarized positrons. Overall production rates and spectra of the K^0 and the $\Lambda^0\,(+\bar{\Lambda}^0)$ were measured and compared with other experiments as well as with Quantum Chromodynamics calculations. The combination of the small, stable beam spots produced by the SLAC Linear Collider (SLC) and the precision vertexing capabilities of the SLC Large Detector (SLD) permitted the separation of the hadronic events into three quark flavor-enriched samples. An unfolding was performed to obtain flavor-pure samples, and for the first time measurements were made of K^0 and $\Lambda^0\,(+\bar{\Lambda}^0)$ production rates and spectra in uds, c, and b quark events at the Z^0 pole. This measurement revealed significant production differences. Utilizing the large quark production asymmetry due to the polarized electron beam, high-purity quark and antiquark jet samples were obtained. The first measurement of production differences of the Λ^0 baryon in quark and antiquark jets was performed, which provided clear evidence for a leading particle effect at high momenta.

Acknowledgements

I knew that Experimental High Energy Physics is a collaborative business, but I hadn't realized that this description would apply to the writing of my thesis! Thanks to Dave Muller, Phil Burrows, Tom Pavel, and Stephane Willocq for their help in the analysis, and their help in putting together this document with endless proof-reading, suggestions, and encouragement.

While being a graduate student, a large fraction of my time was spent working on various hardware projects. I've greatly enjoyed this, both for the work itself and for the large number of people with whom I've had the pleasure of working. My thanks to the "Machine Shop Gang" (Val Myrnyj, Billy Schneider, Eric Paduch, Ernie Erskine, and Arvid Knutsen) for the tremendous attention they gave to the ECRID Mirror Project. Also, thanks to John Doroshenko and Gary Word - I'm really glad that we had a chance to work together. My thanks to the Engineers and Techs at SLAC who put up with me (Rick "Gabe" Gabrielson, Steve Grimaldi, Scott Geary, Matt McCulloch, Bob Reif, Don McShurley, Paul Stiles and Malcolm Lewis) and the CRID collaborators that kept me out of trouble (Jeff Snyder, Jim Shank, Tom Weber, Jerry Va'vra, Blair Ratcliff, Sumit Sen, Mike Sokoloff, Michael Schneider, Scott Whitaker, Bob Wilson, Randy Johnson, Brian Meadows, John Coller, Steve Manly and Charlie Baltay).

My thanks and best wishes go to Homer Neal and Tom Junk for all the time they spent answering my questions. Thanks also to Su Dong for clearing up a major mystery for me, and to Mike Strauss for the many interesting discussions that we had. Thanks to Mike Hildreth and Jingchen Zhou for providing me with several wonderful figures.

I want to thank the "FNA Crowd" (Ray, Steve, John, Greg, Anthony, Michelle, Stephane, Carrie, Craig, and Angelica) for the many pleasant evenings that we've spent together. It really made my trips out to SLAC more enjoyable, and was one of the

reasons that I wanted to move here.

Last, but not least, I'd like to thank my Rutgers' SLD colleagues (Dick Plano, Mohan Kalelkar, Pete Stamer, and Pieter Jacques) for their patience, encouragement, and assistance. We've had a lot of fun working together, and I hope that it'll continue for years to come.

This work was supported in part by grants from the National Science Foundation.

Dedication

This work is dedicated to my parents,

Betty and Ken Baird,

and to my wife,

Annette.

Without your love, help, and support, this wouldn't have been possible.

Thank You All!

Table of Contents

List of Tables

List of Figures

Chapter 1

Introduction

A feature of Quantum Chromodynamics (QCD) [1], the prevalent theory of strong interactions between elementary particles, is the confinement of fundamental particles (quarks) into observed hadrons, such as the proton and neutron. Quarks produced in high energy collisions (such as the quark and antiquark in $e^+e^- \rightarrow Z^0 \rightarrow q\bar{q}$) are observed as a number of hadrons, which at high energies are grouped into "jets". The production of final state hadrons from such initial partons is currently believed to proceed in three stages. The first stage involves the radiation of gluons from the primary quark and antiquark, which in turn radiate gluons or split into $q\bar{q}$ pairs until their virtual mass approaches the hadron mass scale. Such a "parton shower" is calculable in perturbative QCD, for example in the Modified Leading Logarithm Approximation [2]. The next stage, in which these soft partons turn into "primary" hadrons, is not understood quantitatively, although several hadronization models exist. The ansatz of Local Parton-Hadron Duality (LPHD) [2], namely that the distribution for a given hadron species is directly proportional to the parton distribution at some appropriate virtuality, allows the prediction of the shapes of primary hadron momentum spectra, and of the energy- and mass-dependences of their peaks.

The third stage, in which unstable primary hadrons decay into final state hadrons, complicates the interpretation of inclusive measurements. It is desirable to remove the effects of these decays when comparing with the predictions of QCD+LPHD. Additional complications arise in jets initiated by heavy quarks (which are not included in available calculations) since $c-$ and $b-$quarks are known to yield leading heavy hadrons which carry a large fraction of the beam energy (thus restricting the energy available to other primary particles) and decay into a number of secondary particles.

Measurements of the production rates and spectra of identified particles are useful for constraining hadronization models and testing the predictions of QCD+LPHD. Several such measurements have been reported in e^+e^- annihilation, and QCD+LPHD has been successful in describing the shape and energy dependence of inclusive momentum spectra as well as those of identified charged and neutral hadrons [3]. At a given enter-of-mass energy $\sqrt{s}$, the spectrum for identified pions peaks at a higher value of $\xi = \ln(\sqrt{s}/2p)$ (where p is particle momentum) than the spectra of higher mass particle types; however, little mass dependence is observed between these other species.

Previous measurements have used samples of jets initiated by equal numbers of primary quarks and antiquarks. Comparison of the spectrum of a given particle produced in pure quark jets with that in pure anti-quark jets would provide additional information on the hadronization process. Baryons are particularly useful for this as a baryon can contain a primary quark but an antibaryon cannot.

In this analysis, we present the measurement of K^0 and $\Lambda^0/\bar{\Lambda}^0$ production in hadronic Z^0 decays collected by the SLC Large Detector (SLD). The analysis is based upon the approximately 150,000 hadronic events obtained in runs of the SLAC Linear Collider (SLC) between 1993 and 1995. We measure production rates and momentum spectra in a "global" sample of all hadronic events and also in high-purity samples of "light" (uds) and "b" ($b\bar{b}$) events, and in a lower-purity sample of "c" ($c\bar{c}$) events. The light sample is largely free from effects of heavy quark production and decay, but contains decay products of other unstable primary hadrons. In addition, by utilizing the large quark production asymmetry in polar angle induced by the SLC electron beam polarization, we compare for the first time the Λ baryon spectrum from a high-purity sample of light quark jets with that from a similarly pure sample of light anti-quark jets.

This thesis is organized as follows: Chapter 2 contains a brief overview of the Standard Model of the electroweak and strong interactions, discussions of hadronization models, and analytical predictions for particle distributions. Chapters 3 and 4 discuss the major components of the SLD detector and some specific details of the EndCap CRID subsytem. Chapter 5 introduces the reader to the criteria used to record data

events, and the selection cuts used to obtain pure hadronic samples. Here the techniques used to obtained flavor-tagged samples are described, along with the procedures used to obtain high-purity quark and anti-quark samples. Chapter 6 discusses in detail the techniques used to obtain clean K^0 and $\Lambda^0/\bar{\Lambda}^0$ samples, correct for detector effects, and calculate production rates and spectra in the "global" Z^0 decay sample. In Chapter 7 these techniques are combined with the flavor and quark-jet tagging procedures to obtain spectra in flavor- and quark-pure samples. The experimental results are summarized in Chapter 8.

Chapter 2

The Standard Model

In this analysis, the special capabilities of the SLAC Linear Collider/SLC Large Detector (SLC/SLD) will be used to study the hadronization process in Z^0 decays. After a brief review of the electroweak physics pertinent to this analysis, we will provide an overview of the theory of strong interactions (QCD). Models of the hadronization process will be discussed, along with some analytic predictions of hadron distributions.

2.1 The Standard Model of the Electroweak Interaction (EW)

The theory of electroweak (EW) interactions was developed by Glashow, Weinberg, and Salam [4]. They successfully unified electromagnetic theory and the theory of weak interactions in the framework of a gauge theory invariant under transformations of the group $SU(2)_L \otimes U(1)$. Transformations of the group $U(1)$ correspond to phase transformations, and transformations of the group $SU(2)_L$ correspond to arbitrary rotations of isospin doublets. In this theory the left-handed quarks and leptons are arranged into isospin doublets, while the right-handed quarks and leptons are arranged in isospin singlet states.

This gauge theory has the advantage that the gauge bosons occur naturally by requiring invariance under local gauge transformations, and the theory is renormalizable (i.e. calculable to all orders). However, these gauge bosons are massless while the mediators of the weak interactions must be massive to account for the short range nature of the weak interactions. In the EW theory this problem is resolved by the introduction of scalar fields that spontaneously break the $SU(2)_L \otimes U(1)$ symmetry and provide the weak vector bosons with mass while leaving the photon massless. The source of the mechanism, the Higgs boson, has not yet been experimentally observed.

The EW model has three parameters, not counting the mass of the Higgs boson, and the fermion masses and mixing angles [5]. One useful parameterization is:

- The fine structure constant $\alpha = 1/137.036$, determined from the quantum Hall effect.
- The Fermi coupling constant $G_F = 1.16639 \times 10^{-5}$ GeV^{-2}, determined from the lifetime of the muon.
- The Weinberg angle, or more conventionally $\sin^2\theta_W$. This is measured directly by SLD (discussed below), or from a combination of measurements for the mass of the Z^0, other Z^0-pole observables, the W mass, and neutral current processes.

The fine structure constant is a measure of the electromagnetic coupling strength; the Fermi coupling constant is a measure of the weak coupling strength; and $\sin^2\theta_W$ is the mixing angle between the EW gauge fields that results in the physical bosons: γ, $W^\pm$, and Z^0.

In the process $e^+e^- \to f\bar{f}$ (where f is a final state fermion), there are two known neutral gauge bosons that may be exchanged: the photon and the Z^0. The lowest-order Feynman diagrams for these processes are shown in Figure 2.1. The cross section, σ, is proportional to the square of the sum of the two matrix elements represented by these diagrams, $|\mathcal{M}_\gamma + \mathcal{M}_Z|^2$. Thus there are three terms to consider: a purely electromagnetic term, a purely weak term, and an interference term.

The total cross section for $e^+e^- \to$ *hadrons* as a function of the center-of-mass energy ($\sqrt{s}$) is shown in Figure 2.2. The Z^0 pole is clearly evident. Around the Z^0 mass, the effects of the electromagnetic term can be safely neglected, as the weak term dominates by a factor of ~ 800. Additionally, the $\gamma - Z$ interference term is very small. Thus we are left with the Z^0 exchange term.

For unpolarized positrons and longitudinally polarized electrons (the experimental conditions produced by the SLAC Linear Collider), the Born cross section (in the massless fermion limit) for $e^+e^- \to f\bar{f}$ at the Z^0 pole can be expressed by

$$\frac{d\sigma}{d\Omega} = K(v_e^2 + a_e^2)(v_f^2 + a_f^2)[(1 - A_e P_e)(1 + \cos^2\theta) + 2A_f(A_e - P_e)\cos\theta]. \qquad (2.1)$$

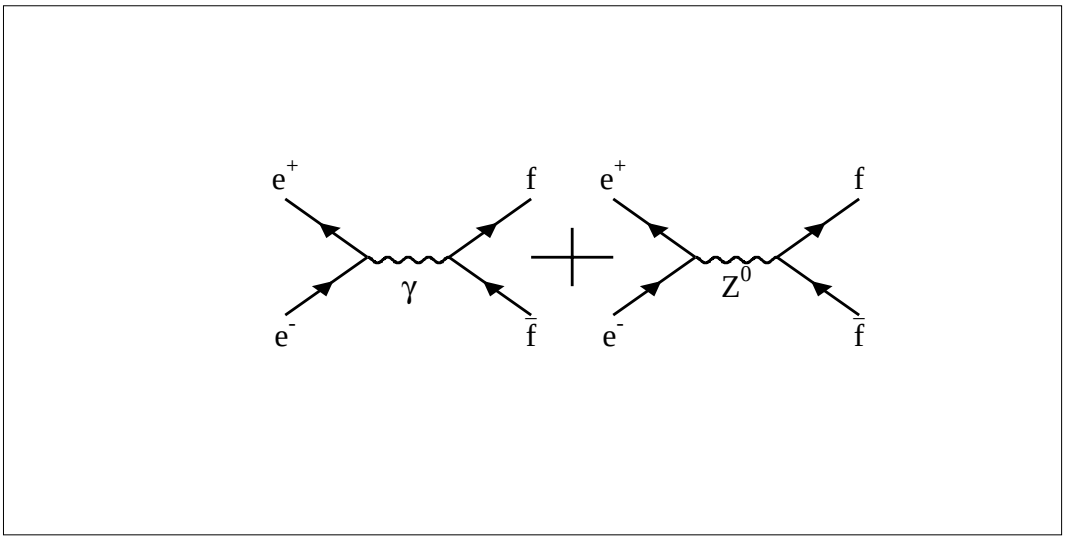

Figure 2.1: The tree level Feynman diagrams representing $e^+e^- \to f\bar{f}$.

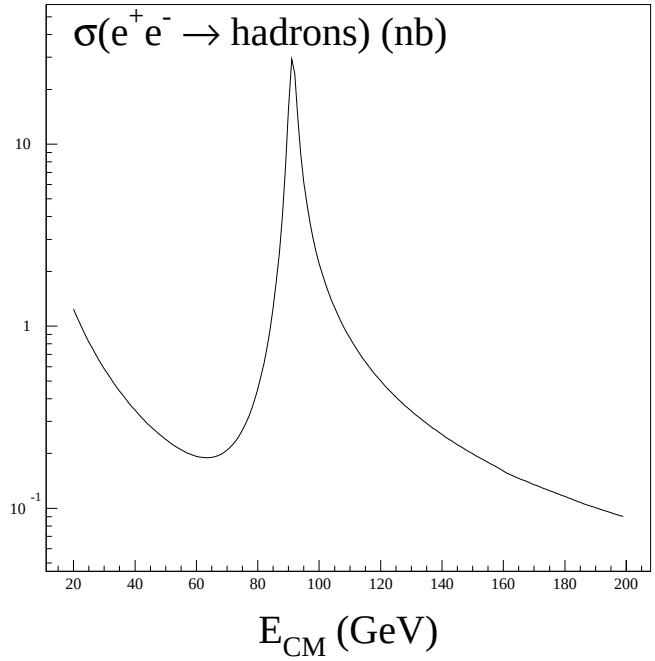

Figure 2.2: The $e^+e^- \to$ *hadrons* cross-section as a function of E_{cm}.

Here, P_e is the signed longitudinal polarization of the electron ($P_e > 0$ for right-handed electrons), v_f and a_f denote the vector and axial-vector couplings of the Z^0 to fermions f (a_e and v_e are the couplings specifically to electrons), and θ is the angle of the final state fermion f with respect to the initial state electron beam. The quantity A_f is defined as

$$A_f = \frac{2v_f a_f}{v_f^2 + a_f^2}, \tag{2.2}$$

and the coefficient

$$K = \frac{\alpha^2}{4\sin^4 2\theta_w} \frac{s}{(s - M_z^2)^2 + ,_z^2 s^2/M_z^2} \tag{2.3}$$

with α being the electromagnetic fine structure constant, and $s = E_{cm}^2$. M_z and $,_z$ are the mass and total decay width of the Z^0 boson, respectively. The deviation of the quantity A_f from zero is a measure of parity violation in the $Z^0 f\bar{f}$ coupling. Table 2.1 lists the Standard Model vector and axial-vector couplings of the Z^0 to different fermions, and Table 2.2 lists some experimentally-determined properties of the Z^0 [5]. As will be discussed in the next section, various asymmetries can be formed from Equation 2.1 to perform stringent tests of EW theory. For portions of this analysis, we will use the polar angle dependence of Equation 2.1 in order to perform QCD studies that rely on the high degree of electron-beam polarization unique to SLC/SLD.

$a_f = T_f^3$		
$v_f = T_f^3 - 2\sin^2\theta_W Q_f$		
fermion	a_f	v_f
ν_e, ν_ν, ν_τ	$+\frac{1}{2}$	$+\frac{1}{2}$
e^-, μ^-, τ^-	$-\frac{1}{2}$	$-\frac{1}{2} + 2\sin^2\theta_W$
u, c, t	$+\frac{1}{2}$	$+\frac{1}{2} - \frac{4}{3}\sin^2\theta_W$
d, s, b	$-\frac{1}{2}$	$-\frac{1}{2} + \frac{2}{3}\sin^2\theta_W$

Table 2.1: The vector and axial vector couplings for fermions to the Z^0 gauge boson. Q_f is the charge of the fermion, and T_f^3 is the third component of the weak isospin for the fermion.

2.1.1 Electroweak Asymmetries

The current theory of EW interactions has been remarkably successful at making predictions which have been verified in the laboratory. As a search for "physics beyond the

Z^0 Mass (M_Z)	91.187 ± 0.007 GeV/c^2
Z^0 Decay Width (, $_Z$)	2.490 ± 0.007 GeV
Z^0 decay branching fractions	
e^+e^-	$(3.366 \pm 0.008)\%$
$\mu^+\mu^-$	$(3.367 \pm 0.013)\%$
$\tau^+\tau^-$	$(3.360 \pm 0.015)\%$
invisible	$(20.01 \pm 0.16)\%$
hadrons	$(69.90 \pm 0.15)\%$
$(u\bar{u} + c\bar{c})/2$	$(9.7 \pm 1.8)\%$
$(d\bar{d} + s\bar{s} + b\bar{b})/3$	$(16.8 \pm 1.2)\%$
$c\bar{c}$	$(11.9 \pm 1.4)\%$
$b\bar{b}$	$(15.45 \pm 0.21)\%$

Table 2.2: Properties of the Z^0 Boson.

standard model", precision measurements of EW parameters are being made in hopes of finding inconsistencies which would indicate a breakdown of the current theory. One powerful technique for making precise measurements is to form asymmetries, or ratios of cross-sections that are insensitive to detailed knowledge of the detector efficiency and beam luminosity.

The Left-Right Asymmetry A_{LR}

The premier asymmetry measured at the SLD is the Left-Right Asymmetry, A_{LR} [6, 7]. The longitudinal polarization of the electron beams allows us to directly examine the parity violation in Z^0 production by forming the quantity

$$A_{LR} = \frac{\sigma(e^+e^-_L \to Z^0 \to f\bar{f}) - \sigma(e^+e^-_R \to Z^0 \to f\bar{f})}{\sigma(e^+e^-_L \to Z^0 \to f\bar{f}) + \sigma(e^+e^-_R \to Z^0 \to f\bar{f})}. \tag{2.4}$$

Here, the polarization of the final states is not measured. Using Equations 2.1-2.2 and the quantities listed in Table 2.1, we see that A_{LR} is directly related to the Weinberg angle $\sin^2\theta_W$ (setting $P_e = 1$):

$$A_{LR} = A_e = \frac{2v_e a_e}{v_e^2 + a_e^2} = \frac{2[1 - 4\sin^2\theta_W^{eff}(M_Z^2)]}{1 + [1 - 4\sin^2\theta_W^{eff}(M_Z^2)]}. \tag{2.5}$$

The relationship of $\sin^2\theta_W^{eff}(M_Z^2)$ to $\sin^2\theta_W$ is analogous to that of the measured electron charge $e(Q^2)$ to the "bare" electron charge e_0 in QED calculations, namely a

number of radiative correction diagrams are needed to "dress" the bare quantity[1]. For arbitrary beam polarization $|P_e|$,

$$A_{LR}^{meas} = |P_e| A_{LR} = \frac{N_L - N_R}{N_L + N_R}, \tag{2.6}$$

where $N_L(N_R)$ is the number of measured Z^0 decays produced using left(right)-handed electron beams. For this quantity, the asymmetry for 100% polarized electron beams is ~ 0.16, assuming a $\sin^2\theta_W$ value of ~ 0.23.

Experimentally, A_{LR} is a very convenient asymmetry to measure. There is no dependence on the final state fermion couplings, so all final state fermions (from s-channel exchange) can be used to measure A_{LR}, and thus the statistical power of A_{LR} is very high. Also, as long as symmetric detector acceptance limits are chosen, A_{LR} is insensitive to final state corrections such as those due to QCD [6]. Lastly, as long as the detector response to fermions and anti-fermions is the same, A_{LR} is independent of detector acceptance.

The SLD Collaboration has performed three measurements of A_{LR}, based upon the 1992, 1993, and 1994-95 physics runs. The combined preliminary results for A_{LR} and for $\sin^2\theta_W^{eff}(M_Z^2)$ (after radiative corrections) are [9]:

$$A_{LR} = 0.1551 \pm 0.0040 \tag{2.7}$$

$$\sin^2\theta_W^{eff}(M_Z^2) = 0.23049 \pm 0.00050, \tag{2.8}$$

making this the single most precise measurement of $\sin^2\theta_W^{eff}(M_Z^2)$ in the world.

The Forward-Backward Asymmetries A_{FB}^f and $\tilde{A}_{FB}^f$

Unlike the Left-Right Asymmetry A_{LR}, the Forward-Backward Asymmetry A_{FB}^f provides information on both the initial state coupling to electrons and the final state couplings to fermions of type f. We define

$$A_{FB}^f = \frac{\sigma_F^f - \sigma_B^f}{\sigma_F^f + \sigma_B^f} = \frac{3}{4} A_e A_f, \tag{2.9}$$

[1] The discussion of these corrections is outside the scope of this text. A detailed discussion is found in [8].

where e.g. $\sigma_F^f = \sigma^f(\cos\theta > 0) = \int_0^1 d(\cos\theta)\frac{d\sigma}{d\cos\theta}$. As the product $A_e A_f$ is measured, one can not disentangle the intial and final state couplings from this asymmetry alone.

With polarized electron beams, a double asymmetry may be formed:

$$\tilde{A}_{FB}^f = \frac{(\sigma_F^L + \sigma_B^R) - (\sigma_F^R + \sigma_B^L)}{(\sigma_F^L + \sigma_B^R) + (\sigma_F^R + \sigma_B^L)} = \frac{3}{4}|P_e|A_f. \tag{2.10}$$

Here, $\sigma_F^{L(R)} = \int_0^1 d(\cos\theta)\frac{d\sigma_{L(R)}}{d\cos\theta}$ for left(right)-handed electron beams. Thus by using longitudinally polarized electron beams, the coupling of the Z^0 boson to the final state fermion is directly accessible. The angular dependence of this "left-right forward-backward asymmetry" [10] is

$$\tilde{A}_{FB}^f(\cos\theta) = |P_e|A_f\frac{2\cos\theta}{1+\cos^2\theta}. \tag{2.11}$$

Measurements of $\tilde{A}_{FB}^b$ and $\tilde{A}_{FB}^c$ have been performed at SLD [11, 12], taking advantage of the fact that the heavy quark hadronizes into a jet with a single heavy hadron, which then can be detected by its weak decay. Measurements of $\tilde{A}_{FB}^q$ ($q = u, d, s$) are more problematic due to the difficulty in separating the particle containing the primary light quark from the large numbers of hadronization particles (discussed below) that contain the same quark flavor.

For QCD studies, the large polar-angle asymmetry of quarks versus anti-quarks (Fig. 2.3) obtained with highly polarized electron beams can be exploited to perform detailed tests of the hadronization process. Quark jet tagging techniques utilizing this asymmetry will be discussed in Chapter 5.

2.2 The Standard Model of the Strong Interaction (QCD)

The foundations of the theory of strong interactions were developed independently by Gell-Mann and Zweig [13], when they introduced the quark model of hadrons. This model, based upon an SU(3) (flavor) symmetry of spin-$\frac{1}{2}$ fractionally charged particles (the u,d, and s quarks), postulated that all hadrons had a quark sub-structure. The existence of particles such as the Ω^- baryon proved to be difficult for this model, as it required a totally symmetric quark state (sss) which is forbidden by the Pauli exclusion principle. The addition of a quantum number *color* was postulated by Han

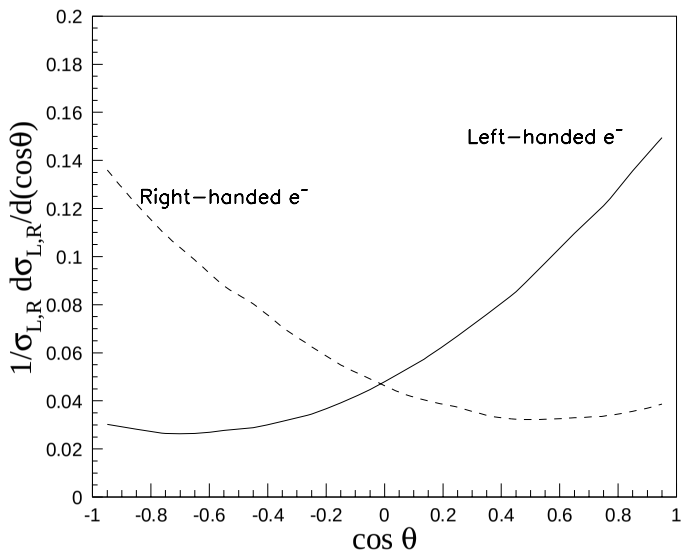

Figure 2.3: The polar angle dependence of the production cross section of quarks for left-handed and right-handed electron beams. Final state left-handed fermions tend to follow in the same direction as the initial state left-handed particles.

and Nambu [14] in order to solve this mystery. The discovery in 1968 of the scaling of structure functions in the SLAC-MIT deep inelastic electron scattering (DIS) experiments [15] provided the first evidence for the physical existence of quarks.

The theory of Quantum Chromodynamics (QCD) [1] is a local non-Abelian gauge field theory of colored quarks and gluons, collectively called partons. The quarks are point-like spin-$\frac{1}{2}$ particles with fractional electric charge that also carry a "color" charge. They come in six "flavors" (u, d, s, c, b, t) and three colors (conventionally labeled as r, g, b). The gluons are the force-mediating particles between the color-charged objects, in the same manner as the photons are the force-mediating particles between electrically-charged objects. Unlike photons, the gluons are themselves carriers of charge (color), and thus gluon-gluon couplings are allowed. This theory has the desired property of *asymptotic freedom* – i.e. it explains the experimentally observed behavior of quarks acting quasi-freely at small distances, but interacting strongly at large distances [4], so that only *colorless* bound quark states (eg. $q\bar{q}$, qqq) are observed.

Quarks produced in high energy collisions manifest themselves as collimated showers of hadrons, referred to as "jets". Jets were first observed at SPEAR [16] in $e^+e^- \to q\bar{q} \to$

2 jet events. It was here that independent confirmation of the spin-1/2 nature of quarks was made, based upon the angular distribution of the jets. Gluons were first observed at TASSO [17] where events with three jets were interpreted at $e^+e^- \rightarrow q\bar{q}g$; an example of a three jet event obtained at SLD is shown in Figure 2.4. For these high energy interactions, the underlying parton behavior may be studied by making measurements of the jet observables, such as number, energy, and event orientation [18, 19]. Such observables can be calculated in perturbative QCD, as this is the regime where the strong coupling constant between partons, α_s, is small ($\alpha_s << 1$). Thus the partons are behaving quasi-freely.

For lower energy interactions, α_s becomes large, and thus the calculations of quark interactions become difficult (i.e. they are non-perturbative). The process of hadronization, where quarks "dress" themselves into jets of colorless hadrons, takes place at very low momentum transfers – $\mathcal{O}(500\text{ MeV})$ – at which point the calculations are essentially impossible. Therefore several models of the hadronization process have been developed, and will be discussed below. The study of specific particle production in these jets may serve to increase our understanding of this non perturbative process.

2.2.1 Hadron Production in e^+e^- Collisions

One of the cleanest methods for studying hadron production is in e^+e^- annihilation events. At the Z^0 energies, the initial state is very well understood, and the backgrounds are heavily suppressed. The process of $e^+e^- \rightarrow$ *hadrons* is conventionally regarded [20] to proceed via the first three stages shown in Figure 2.5. These stages are discussed below.

Phase 1 is the *perturbative phase.* The first portion of this phase, the production of a $q\bar{q}$ pair, has been discussed in Section 2.1. The lowest order $e^+e^- \rightarrow q\bar{q}$ diagram (Fig. 2.6(a)) is modified by QCD to first order by the emission of a gluon (Fig. 2.6(b)). The cross section for this may be written [21] :

$$\frac{d\sigma^2}{dx_1 dx_2} = \sigma_0 \frac{2\alpha_s}{3\pi} \frac{{x_1}^2 + {x_2}^2}{(1-x_1)(1-x_2)}, \tag{2.12}$$

where σ_0 is the tree level cross section for $e^+e^- \rightarrow q\bar{q}$ (the integral of Eqn. 2.1), and x_i

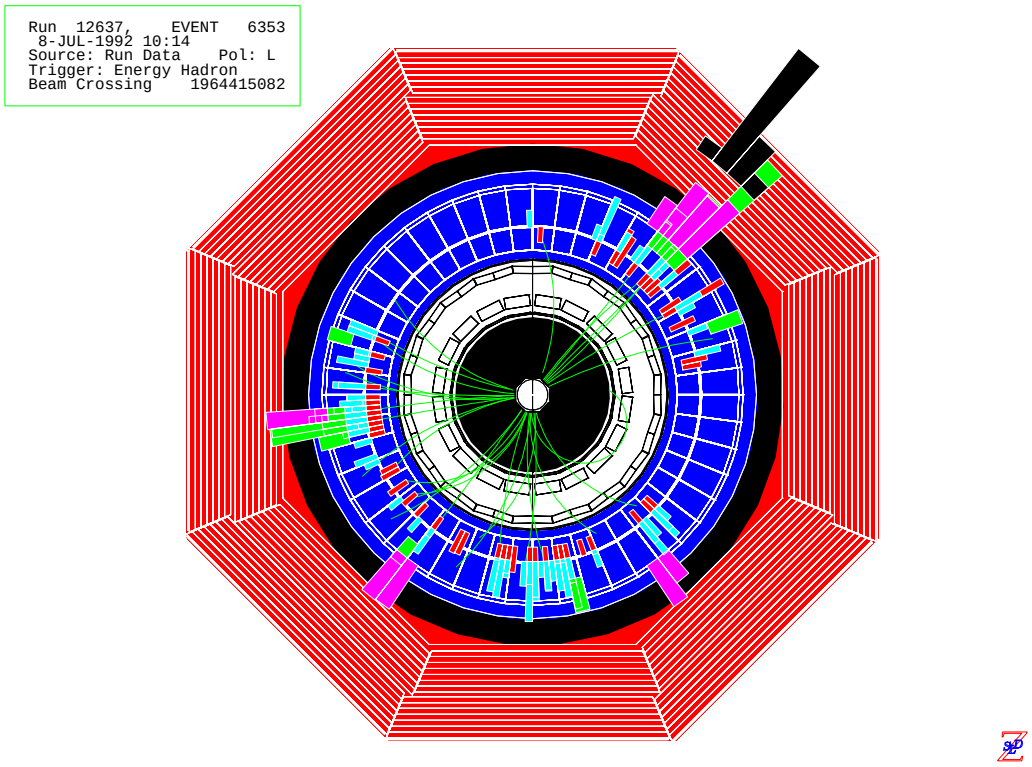

Figure 2.4: A 3-jet event recorded by SLD, viewed along the electron-beam axis. The dashed lines originating in the center of this figure are charged tracks measured by the tracking chambers, discussed in the next chapter.

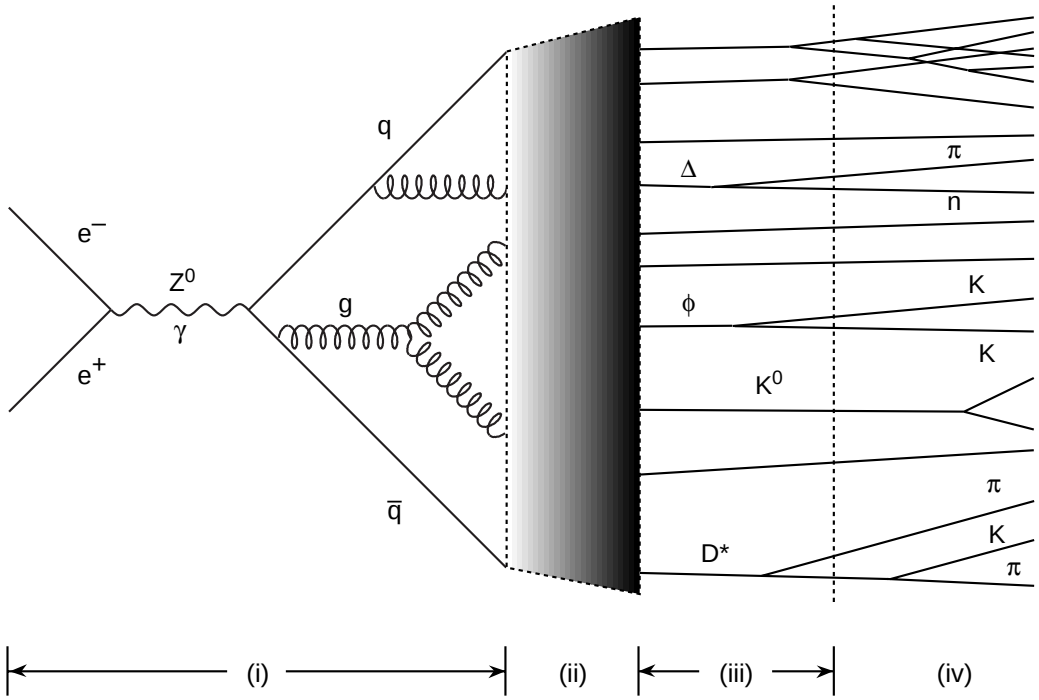

Figure 2.5: The three main phases of the $e^+e^- \rightarrow$ *hadrons* process (the perturbative, hadronization, and decay phases). In phase (iv) the final state particles are measured.

is the scaled energy of parton i:

$$x_i = 2E_i/\sqrt{s}; \qquad \text{where} \tag{2.13}$$
$$x_1 < x_2 < x_3 \quad \textit{and} \quad \sum x_i = 2.$$

Equation 2.12 is clearly divergent for $x_1, x_2 \rightarrow 1$; however these singularities are cancelled by corresponding poles in the $e^+e^- \rightarrow q\bar{q}$ cross section when first order virtual corrections are included. In second order perturbative QCD, two additional processes are allowed: $e^+e^- \rightarrow q\bar{q}gg$ and $e^+e^- \rightarrow q\bar{q}q'\bar{q}'$ (Fig. 2.6(c)). These cross sections have been calculated by several groups [22, 23]; their results are in good agreement with one another.

For configurations beyond 4 partons in the final state, or for virtual corrections to fewer parton final states, the cross section calculations quickly become unwieldy due to the large number of Feynman diagrams involved. One approach to this problem involves *Parton Showers* (PS).

In the PS approach, the production of partons is viewed as the successive branching

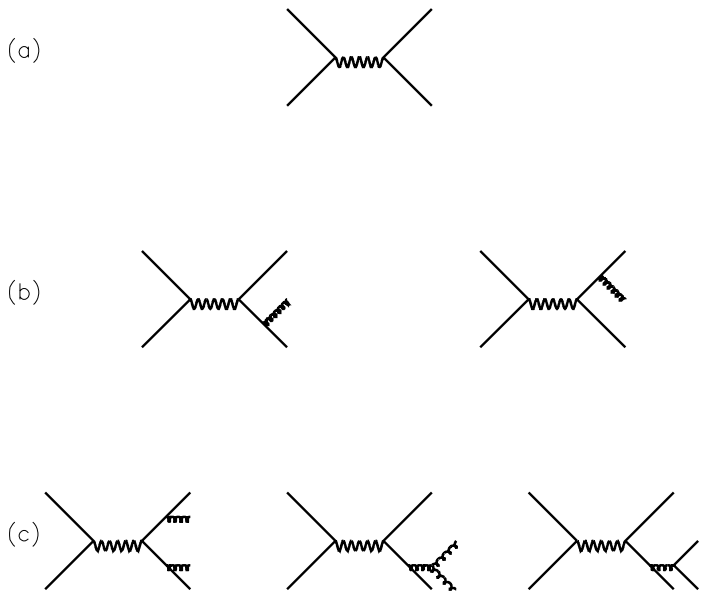

Figure 2.6: Example tree-level Feynman diagrams for (a) $q\bar{q}$ production, (b) the $\mathcal{O}(\alpha_s)$ production of $q\bar{q}g$, and (c) the $\mathcal{O}({\alpha_s}^2)$ production of $q\bar{q}gg$ and $q\bar{q}q'\bar{q}'$.

of partons: $q \rightarrow qg$, $g \rightarrow gg$, or $g \rightarrow q\bar{q}$. In the splitting process $a \rightarrow bc$, z is the fraction of the parent's 4-momentum carried away by daughter b (thus daughter c has a momentum fraction $1-z$). The probability $\mathcal{P}$ that a branching $a \rightarrow bc$ will take place during a small interval dt of a "generalized evolution parameter " (such as Q^2) is given by the Altarelli-Parisi equations [24]

$$\frac{d\mathcal{P}_{a\rightarrow bc}(z)}{dt} = \int dz \frac{\alpha_s(q^2)}{2\pi} \mathcal{P}_{a\rightarrow bc}(z), \; where \tag{2.14}$$

$$\mathcal{P}_{q\rightarrow qg}(z) = \frac{4}{3}\frac{1+z^2}{1-z}, \tag{2.15}$$

$$\mathcal{P}_{g\rightarrow gg}(z) = 6(\frac{1-z}{z} + \frac{z}{1-z} + z(1-z)), \tag{2.16}$$

$$\mathcal{P}_{g\rightarrow q\bar{q}}(z) = \frac{1}{2}(z^2 + (1-z)^2). \tag{2.17}$$

By applying the Altarelli-Parisi equations in a probabilistic iterative manner, a "Parton Shower" is produced (Fig. 2.7). In order to avoid singular regions of the splitting kernels, and thus excessive production of soft partons, a cutoff parameter $Q_0 = \mathcal{O}(1GeV)$ is used to terminate the showering when all the partons are below this energy. This cutoff parameter corresponds to requiring a minimum effective mass of the parton.

Phase 2 is the *hadronization phase.* Due to its non-perturbative nature, this process, also referred to as fragmentation, has yet to be calculated in QCD. Thus, several phenomonological models have been developed to describe the process by which a number of colored partons form colorless hadrons. The three main "schools" of fragmentation models are: independent fragmentation, string fragmentation, and cluster fragmentation. These categories are not mutually exclusive; some models have components of each.

Independent Fragmentation (IF) dates back to the early 1970's, and was suggested as a "toy model" by Field and Feynman [25]. While initially popular due to the availability of Monte Carlo programs [26], this model is almost never used in current e^+e^- experiments. It assumes that the fragmentation of any system of partons can be described as an *incoherent* sum of independent fragmentation processes, i.e. every parton fragments independently. A consequence of this is that at the end of the fragmentation chain, neither energy, momentum, nor flavor is necessarily conserved. To remedy this,

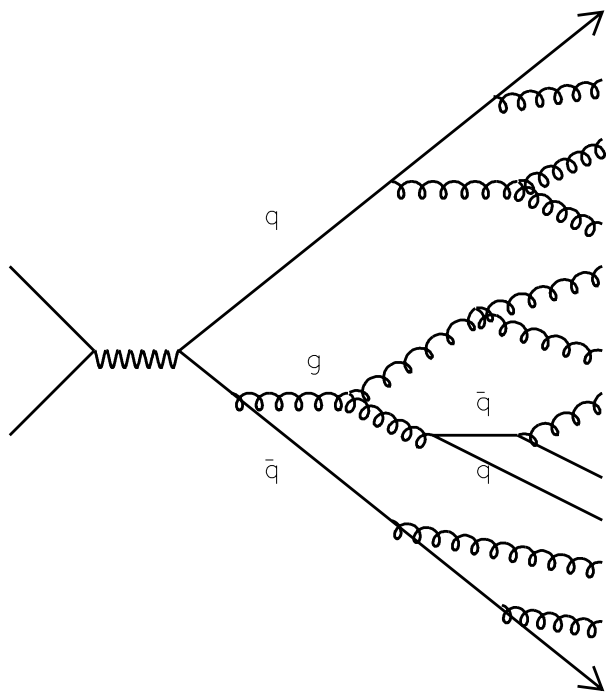

Figure 2.7: A schematic of a Parton Shower.

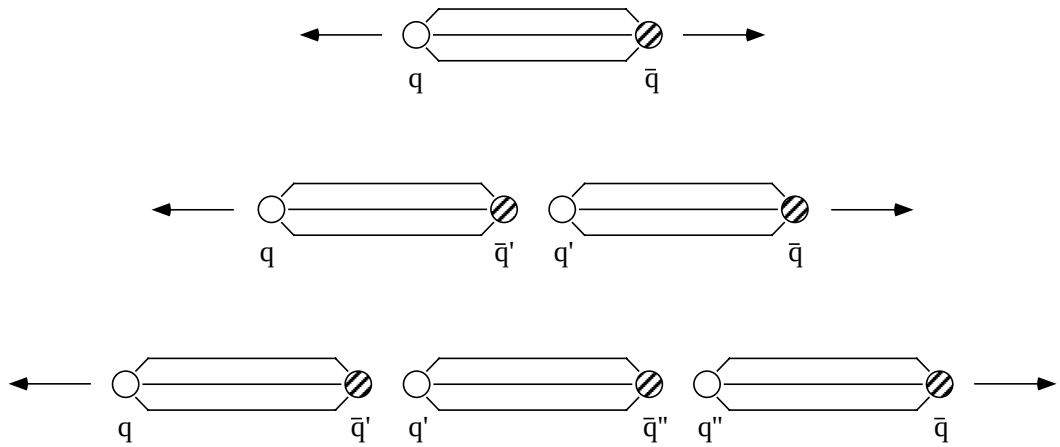

Figure 2.8: A color tube (string) stretching between a q and a $\bar{q}$. As the q and the $\bar{q}$ separate, the potential energy in the string increases. When this energy is above threshold for creating a $q'\bar{q}'$, the string may break.

special "fixup" algorithms were introduced into the Monte Carlo code. Furthermore, the early IF models were not Lorentz invariant, although this was later corrected.

The first example of a *String Fragmentation (SF)* scheme was introduced in 1974 by Artru and Mennessier [27]. With the development and incorporation of a more elaborate string model by the Lund group [28, 29] string fragmentation has become almost synonymous with the Lund model. The string model is based upon the QCD-inspired idea that the primary partons are connected by a color flux tube, or string [30]. Consider the field lines connecting two color charges (Fig. 2.8). This is analogous to the electromagnetic field lines connecting two electrically charged objects. However, due to the coupling between gluons, the field lines are pulled together to form a color "string" between the two partons. If the string has a constant energy density per unit length (estimated to be $\sim$ 1 GeV/fm) then the potential energy of the string rises linearly as the color charges are separated. Once the potential energy has grown sufficiently to produce $q - \bar{q}$ pairs, the string breaks (with probability f(z), described below) to form two separate string objects. If the invariant mass of a string object is large enough (i.e. $\geq$ hadron mass), further breaks may occur until ordinary hadrons remain.

Classically, massless quarks can be produced at a point and then be pulled apart by the color field. If they have mass or transverse momentum (with respect to the string axis), they have to be produced at some distance from each other so that the mass

and/or transverse momentum is supplied by the energy of the color field connecting them. Quantum mechanically, the $q'\bar{q}'$ pair is produced at a point and tunnels out to the "allowed" region. The tunneling probability is a function of the quark mass and transverse momentum (p_T), as is given by [30]:

$$P = \exp(-\frac{\pi m_T^2}{\kappa}), \tag{2.18}$$

where κ is the string constant (estimated to be $\sim$ 1 GeV/fm) and $m_T^2 = m^2 + p_T^2$. Because of the mass term in the exponent, strange and heavy quark (c, b) production is suppressed, yielding the relative production rates of quark flavor $u : d : s : c \sim 1 : 1 : 0.3 : 10^{-11}$. Thus, charm and heavier quarks are not expected to be produced in observable amounts in fragmentation.

In the Lund model, the probability for a second string to be formed with fraction z of the energy and longitudinal momentum $E + p_L$ of the original string is:

$$f(z) = z^{-1}(1-z)^a \exp \frac{-bm_T^2}{z}. \tag{2.19}$$

The variables a and b are parameters of the model, and must be tuned to best fit the experimental data [31]. These parameters may vary for different primary quark flavors, and for formation of mesons versus baryons.

The string fragmentation model can also be applied to multiparton systems. For the $q\bar{q}g$ process, the string is stretched from q to to the gluon g to the $\bar{q}$, as shown in Figure 2.9. Thus, the gluon is a "kink" in the color string, carrying momentum and energy.

The *Cluster Fragmentation (CF)* concept is technically simpler than the string fragmentation model, as it has fewer parameters to vary. In the Webber Model [32], implemented in the HERWIG Monte Carlo progam, a parton shower is used to form colorless clusters. These clusters do not themselves have any internal structure, and are characterized by only their total mass and flavor content. In this model, they are assumed to be the basic units from which hadrons are produced. The heavy clusters fragment into lighter ones, and these ultimately fragment into final state hadrons. Four-momentum is exchanged among neighboring clusters to achieve overall energy and momentum conservation.

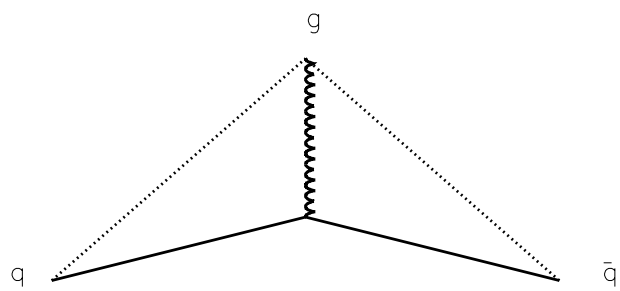

Figure 2.9: The string model for a $qg\bar{q}$ system, with the g causing a "kink" in the string. This configuration might lead to a 3-jet event similar to that shown in Figure 2.1.

In the *Decay phase*, the unstable hadrons decay into stable particles. The quantitative features of these decays are usually well known from experimentally determined branching fractions. These stable (*observable*) particles are what are measured by particle physics detectors. In this analysis, by obtaining experimental information on the final state hadrons, we shed further light on the hadronization process.

2.2.2 MLLA/LPHD and Analytic Predictions

As was noted in the previous section, the nonperturbative nature of the hadronization process makes calculations exceedingly difficult. The existence of jets in hadronic events indicated that the underlying behavior of "colored" partons can be (indirectly) studied by observation of the final state hadrons; i.e. that a "parton-hadron duality" exists. The ansatz of Local Parton Hadron Duality (LPHD) [2] asserts that a similar duality occurs locally (e.g. at any stage of a Parton Shower), and manifests itself in a close correspondence between parton and hadron distributions. If this correspondence does exist, then predictions of primary hadron distributions (without model dependencies) are possible for the cases where analytic calculations at the parton level have been performed.

Using the modified leading logarithmic approximation (MLLA) with the hypothesis

of LPHD, theoretical predictions of the distribution of hadrons in the scaled momentum variable $\xi = ln(1/x_p)$ (where $x_p = p_{hadron}/p_{beam}$) have been made [33]. The parton spectrum (and thus, using LPHD, the hadron spectrum) is expressed by:

$$x_p \bar{D}_i^f(x_p, Y, \lambda) = \tag{2.20}$$

$$\frac{4C_F(Y+\lambda)}{bB(B+1)} \int_{\epsilon - i\infty}^{\epsilon + i\infty} \frac{d\omega}{2\pi i} x_p^{-\omega} \Phi(-A+B+1, B+2, -\omega(Y+\lambda)) \cdot \mathcal{K} \tag{2.21}$$

where

$$\mathcal{K} \equiv K(\omega, \lambda) = \frac{,(A)}{,(B)} (\omega\lambda)^B \Psi(A, B+1, \omega\lambda) \cdot C_i^f \tag{2.22}$$

Here $Y = \log(E\Theta/Q_0)$, $\lambda = \log(Q_0/\Lambda)$, and Θ is the opening angle of the jet cone. For five flavors C_F =4/3, b =23/3, $A = 12/b\omega$ and $B = 307/27b$. The functions Φ and Ψ are two solutions of the confluent hyper-geometric equation. Λ is the QCD scale parameter and Q_0 is the energy cutoff of the parton evolution. Indices i and f stand for the initial parton generating the jet ($i = q, g$) and the final parton spectrum being studied ($f = q, g$). In the MLLA approximation, $C_g^g = 1$ and $C_q^g = \frac{4}{3}$. Luckily, this spectrum approximates to a gaussian for the "limiting spectrum" (i.e. where $Q_0 \sim \Lambda$, the scale at which hadronization takes place):

$$\bar{D}(\xi, Y) \approx \mathcal{N}(Y) \left(\frac{36C_F}{\pi^2 b Y^3}\right)^{1/4} \exp\left[-\sqrt{\frac{36C_F}{b}} \frac{(\xi - \xi^*)^2}{Y^{3/2}}\right] \tag{2.23}$$

where

$$\ln \mathcal{N} \approx \frac{1}{b}\sqrt{\frac{32\pi C_F}{\alpha_s(Y)}} + \left(\frac{B}{2} - \frac{1}{4}\right) \ln \alpha_s(Y) + O(1). \tag{2.24}$$

Here, $\mathcal{N}$ is the limiting parton multiplicity.

Thus, the hadron spectrum is expected to have an approximate Gaussian shape, often referred to as a "hump-backed" shape, due to the underlying parton dynamics. The development of the parton shower causes the parton (and thus the hadron) multiplicity to rise with increasing ξ (decreasing momentum). This development ceases at some cutoff scale, Q_0, at which point hadronization takes over, collecting partons into hadrons. The hadron multiplicity then decreases as ξ further increases.

As the center of mass energy increases, the maximum of this distribution, ξ^*, shifts

toward higher ξ according to the equation:

$$\xi^* = Y\left(\frac{1}{2} + a\sqrt{\frac{\alpha_s(Y)}{32C_F\pi}} - a^2\frac{\alpha_s(Y)}{32C_F\pi} + \cdots\right), \tag{2.25}$$

where the quantity a is defined as

$$a = \frac{11}{3}C_F + \frac{2n_f}{3N_c^2}, \tag{2.26}$$

and thus increases approximately linearly in Y (i.e. $\log E$). The predicted gaussian spectrum shape has been observed by many experiments for inclusive charged tracks and various identified particles; the energy dependence of the peak position has been confirmed by many different experiments at different energies [34].

It has been speculated that for a given hadron species, the peak position depends on the hadron mass; the higher the mass of the hadron species, the higher the effective cut off Q_0, and the lower the ξ^* value. This behavior has not been clearly observed for the identified hadrons, although when considering just the meson data or just the baryon data a mass dependence is observed. This may be due to the "contamination" of the measurable spectrum by particles from secondary sources. For example, the measured pion spectrum in e^+e^- events is a sum of the spectra from fragmentation, ρ decays, K^* decays, etc. Additional complications arise from the presence of heavy quarks: in addition to the hard spectra from heavy quark decays, there is the caveat that the calculations were performed in the massless parton limit. Using the flavor tagging techniques discussed in Chapter 5, we will study spectra for the light-quark samples. This will not remove the contribution due to resonances, but will remove the contributions from heavy quark decays.

Chapter 3

The SLC and the SLD Detector

The data used in this analysis was collected at the Stanford Linear Accelerator Center (SLAC) in Stanford, California. The SLAC Linear Collider (SLC) is a unique single-pass electron-positron collider that produces longitudinally-polarized Z^0's. The SLC Large Detector (SLD) is a state-of-the-art full coverage multipurpose detector placed at the interaction region. This chapter presents an overview of the main features of the SLC and the SLD.

3.1 The SLC

The SLC is the world's only linear collider (Fig. 3.1). The 2 mile long linear accelerator (linac) was constructed in the 1960's to study the interior structure of the nucleon by scattering 20 GeV electrons on fixed targets [35]. It was upgraded in the 1980's to act as a single pass electron-positron collider with sufficient energy to produce Z^0 bosons at threshold. The addition of a polarized electron source gives the SLC the unique capability to control the Z^0 polarization, which (as described in the previous chapter) is a useful tool for studying the electroweak interaction and some aspects of quantum chromodynamics.

At the start of each 120 Hz cycle, the polarized electron source (described below) produces two bunches of approximately 6×10^{10} electrons. These bunches, approximately 1 mm in length, are accelerated in the linac to 1.19 GeV and stored in the north damping ring of the SLC. Damping rings are used to compress the bunches and reduce energy fluctuations. Just before each electron bunch enters the damping ring, the polarization of the bunch is rotated from the horizontal (longitudinal) direction to the vertical direction. This is done so the electrons are not depolarized by the natural

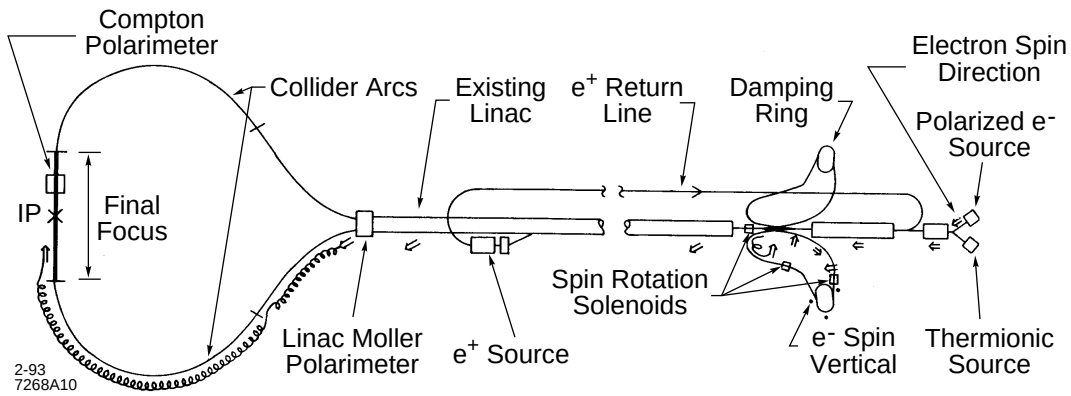

Figure 3.1: The SLC layout.

spin dynamics of the ring.

After damping, the two electron bunches and a positron bunch (discussed below) are extracted from the damping rings and further accelerated by the linac (the positron bunch leads the other two). The e^+ bunch and the first e^- bunch are both accelerated to 46.7 GeV and, at the exit of the linac, are directed by dipole magnets into a pair of 1 km long arcs, after which they then intersect at the interaction point (IP) located in the center of the SLD. During their travels through the arcs, the electrons and positrons lose energy through synchrotron radiation, and by the time the two bunches collide the mean energy per bunch is $\sim$ 45.6 GeV (half of the Z^0 rest mass).

The second e^- bunch that is extracted from the damping ring is accelerated to 30 GeV and then diverted onto a Tungsten-Rhenium alloy target. The resulting shower is filtered for positrons, which are brought back to the front-end of the linac to be used in the next cycle.

In addition to the damping rings, the arcs also have the potential for depolarizing the electron bunch. To counteract this, the electrons are *launched* into the arcs with the polarization tilted to a specific angle. After spin precession, mostly due to coupling between vertical betatron oscillations and dipole bending, the electron bunch arrives at the IP longitudinally polarized. This launch angle is optimized to produce the best longitudinal polarization at the IP.

As time progresses, the SLC continues to be more efficient in producing Z^0's (Fig. 3.2). It is projected that another 500k Z^0's will be produced in the remaining scheduled

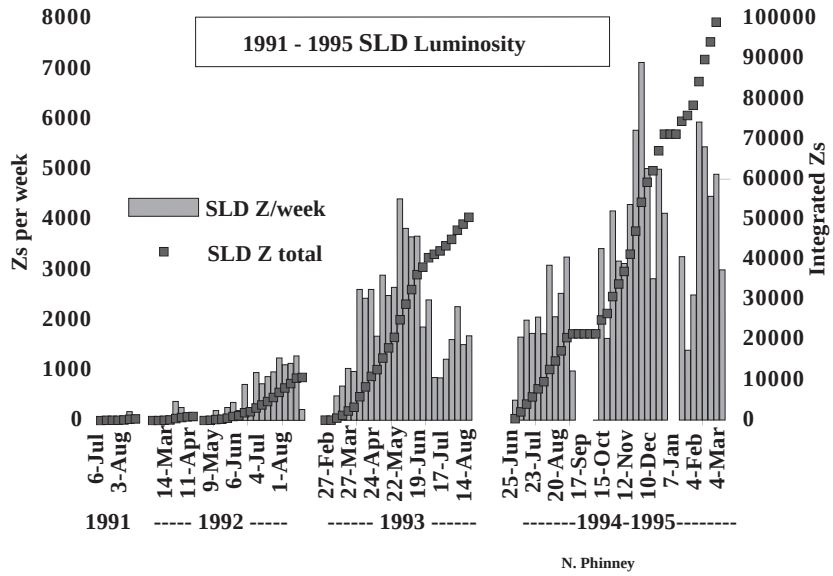

Figure 3.2: The time history for Z^0 production at SLC/SLD.

runs.

3.2 Polarization at SLC

3.2.1 The Polarized Electron Source

The SLC has the unique capability of colliding longitudinally polarized electrons with (unpolarized) positrons to produce polarized Z^0's. This is made possible by the use of Gallium-Arsenide (GaAs) photo-cathodes in the electron gun [36]. Circularly polarized laser-light (from a Nd:YAG-pumped Ti:sapphire laser) is used to selectively excite electron transitions into longitudinally-polarized states in the conduction band. An energy state diagram is shown in Figure 3.3.

For the 1992 physics run, a bulk GaAs cathode was used. This cathode had a theoretical maximum polarization of 50%; the average polarization measured [37] was 22%. For the 1993 and 1994/95 runs, a strained-lattice cathode consisting of GaAs "grown" on a GaAsP (Gallium-Arsenide-Phosphide) substrate was used. This strained lattice had a theoretical maximum polarization of 100%, and for the 1993 run produced approximately 65% polarization at the source [38]. A still-newer cathode with an extremely thin layer of GaAs was used for the 1994-95 physics run; it produced $\sim$ 80%

polarized electrons.

3.2.2 The Compton Polarimeter

The polarization of the electron bunch near the IP is measured by a Compton scattering polarimeter [8]. This polarimeter has two main components: a laser with polarizing optics, and an electron spectrometer (Fig. 3.4). A circularly polarized laser beam is focussed onto the electron bunches just after they pass through the IP (approximately 30 m downstream). Polarized photons undergo Compton scattering with some of the electrons, causing them to lose momentum. The electrons pass through a precision dipole magnet, where the scattered electrons are bent away from the main bunch. The momentum spectrum of the scattered electrons is determined by measuring their deflection angle with Cherenkov and proportional tube chambers.

The differential cross section for the Compton scattering of polarized electrons and polarized photons can be written as:

$$\frac{d\sigma}{dE} = \frac{d\sigma_u}{dE}[1 + P_\gamma P_e A_c(E)], \tag{3.1}$$

where σ_u is the unpolarized Compton scattering cross section, P_γ is the measured photon polarization, P_e is the unknown electron polarization, and A_c is the Compton asymmetry, which depends upon the energy of the scattered electron and the relative orientation of the electron spin and the photon spin (i.e. parallel or anti-parallel) [8]. Because A_c can be precisely calculated, the precision of the Compton polarimeter is limited only by detector systematics. For the 1993 physics run, the average longitudinal polarization at the IP was $(63.0 \pm 1.1)\%$; during the 1994-95 run the average was $(77.0 \pm 0.6)\%$ [9].

3.3 The SLD

The SLD, proposed in 1984 [39], is located at the e^+e^- interaction point (IP) of the SLC. It is a general purpose detector designed to have nearly complete solid angle coverage around the IP. The cut-away geometry is shown in Fig. 3.5 (the endcap portions have been removed) and a quadrant view is shown in Fig. 3.6. The *barrel* portion of

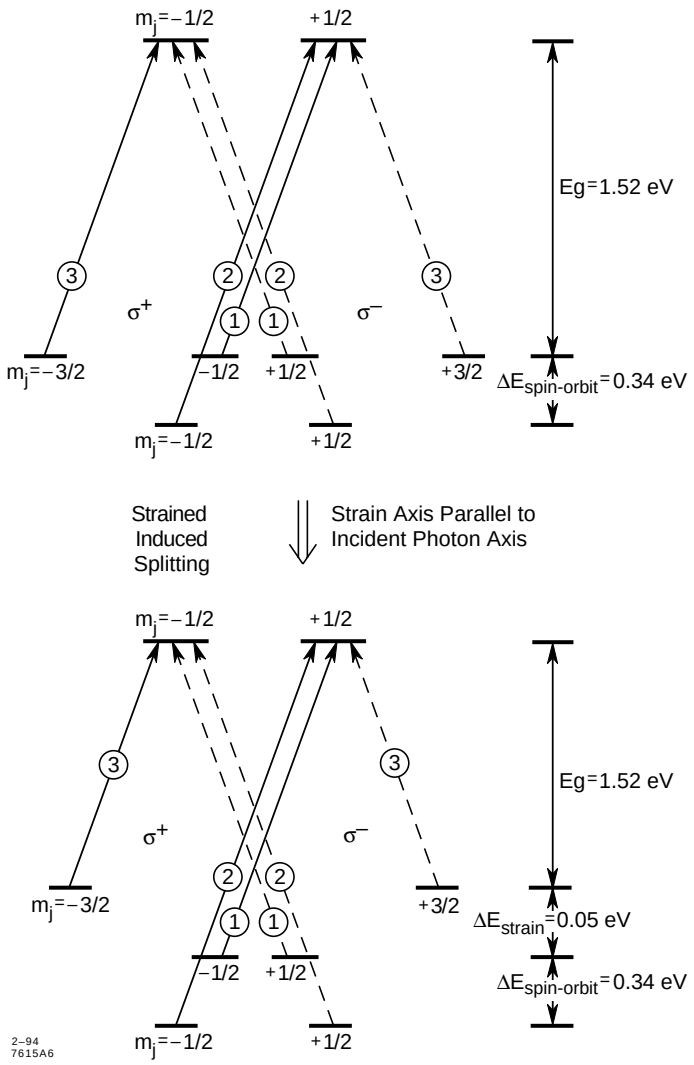

Figure 3.3: The energy state diagram for bulk GaAs (top) and the changes it undergoes when the lattice is strained (bottom). The polarization is due to the preference of certain excitation modes; the relative sizes of the matrix elements are shown in the circles. For the bulk GaAs, the maximum theoretical polarization is 50%. For the strained lattice, the maximum theoretical polarization is 100%.

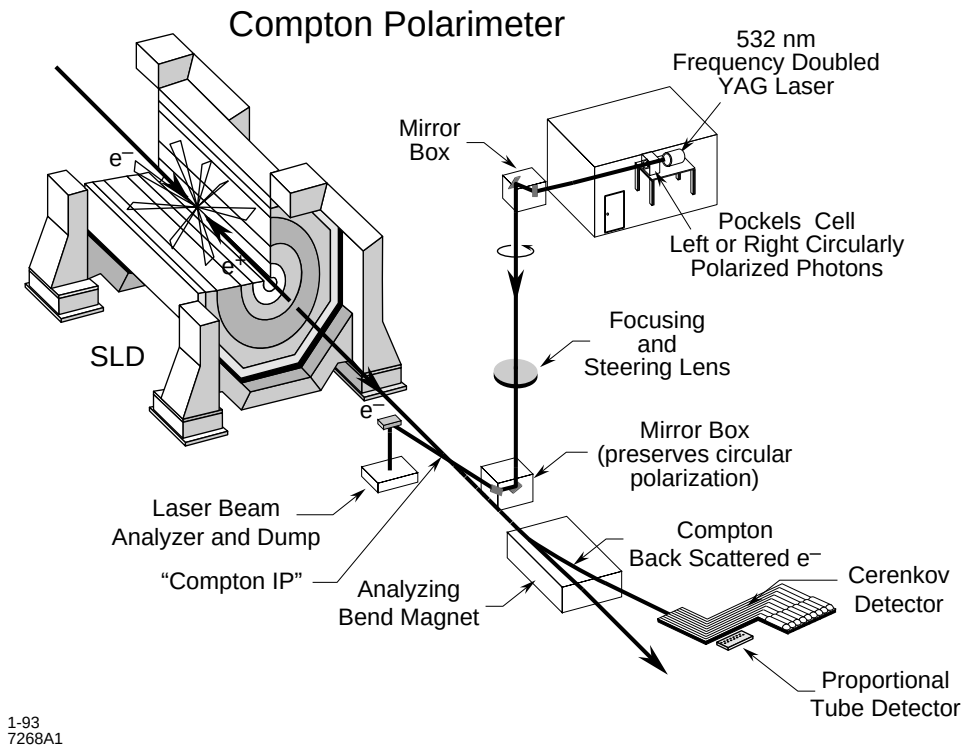

Figure 3.4: The Compton Polarimeter.

SLD is approximately a cylinder of 4.5 m radius and 10 m length. The e^+e^- beams enter along the axis of the detector, and the various detector subsystems are arranged radially within the cylinder. The *endcaps* close off the two faces of the cylinder, nearly completing the solid angle coverage. At small angles to the beam, there is no detector coverage due to the location of the beam-pipe and its support structures. Nevertheless, the detector provide coverage for 98% of the solid angle. The outer support structure of the SLD is the magnetic coil which produces a 0.6 T magnetic field. With the exception of the Warm-Iron Calorimeter (WIC), all of SLD's subsystems reside inside the coil.

3.3.1 The Luminosity Monitor (LUM)

The Luminosity Monitor was designed to provide a high-precision measurement of the absolute luminosity as well as luminosity differences between left- and right-handed polarized beams [40]. In addition, it was designed to extend the electromagnetic calorimetry coverage down to very small polar angles (the Liquid Argon Calorimeter –Section 3.3.5– provides electromagnetic shower (EM) coverage for 98% of the solid angle), and

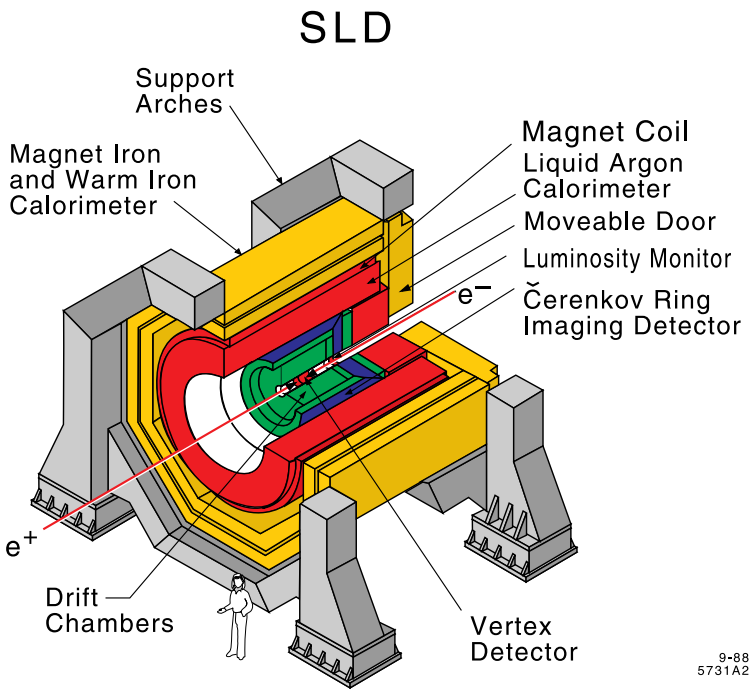

Figure 3.5: The SLD detector (isometric view). The endcaps have been removed for clarity.

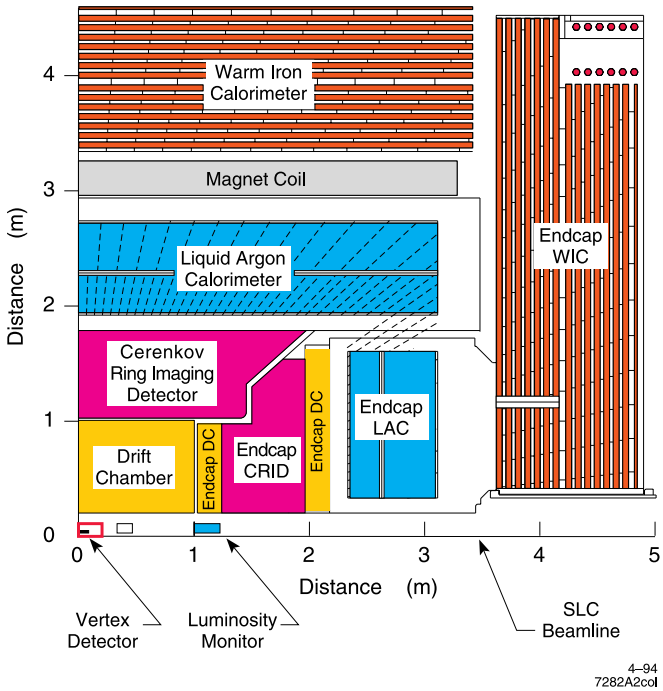

Figure 3.6: The SLD detector (quadrant view).

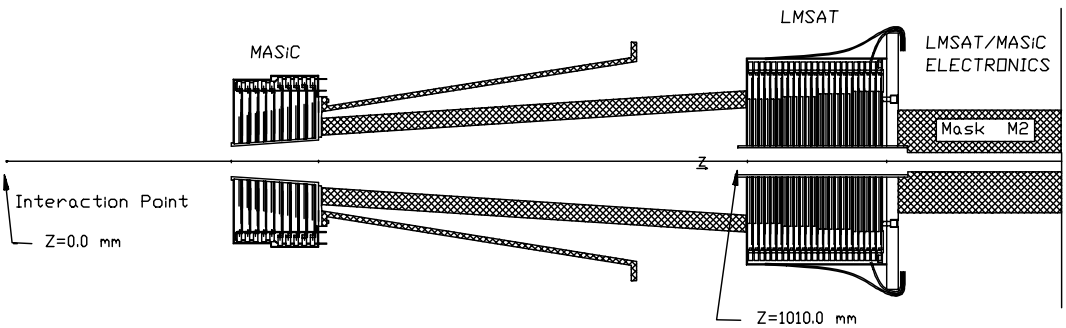

Figure 3.7: The SLD LUM, showing the LMSAT and the MASiC.

to tag electrons for two-photon physics. To do so, the small angle calorimeters employ silicon sampling detectors.

The LUM, shown in Figure 3.7, is divided into two separate modules. The LMSAT, Luminosity-Monitor/Small-Angle Trigger, mounts directly onto the Superconducting Final-Focus triplet assembly and provides polar angle coverage between 28 and 68 mrad. The MASiC, Medium Angle Silicon Calorimeter, provides coverage from 68 to 200 mrad. The EndCap LAC (discussed below), provides EM coverage for angles above 200 mrad.

3.3.2 The Vertex Detector (VXD)

The VXD uses Charge-Coupled Devices (CCDs) as the medium for detecting the ion deposition of charged particles traversing the active region. These CCDs, which contain many tiny "pixels", are ideal for measuring the space points of a charged track's trajectory.

The VXD, shown in Figure 3.8, is constructed from 60 9.2 cm long ladders arranged into four concentric cylinders, which are held in place by a beryllium shell. Eight CCDs are mounted on each ladder, with four on each side to maintain symmetric polar angle. Each CCD is $\sim$ 1 cm square, and contains $\sim 200K$ pixels, each of which is 22 μm square. On the average, 2.3 VXD (pixel) hits are obtained for each charged track passing through the detector. The inner layer of CCDs is at a radius of 29.5 mm from the IP, and the outer layer is at a radius of 41.5 mm. Each layer is 1.1% of a radiation

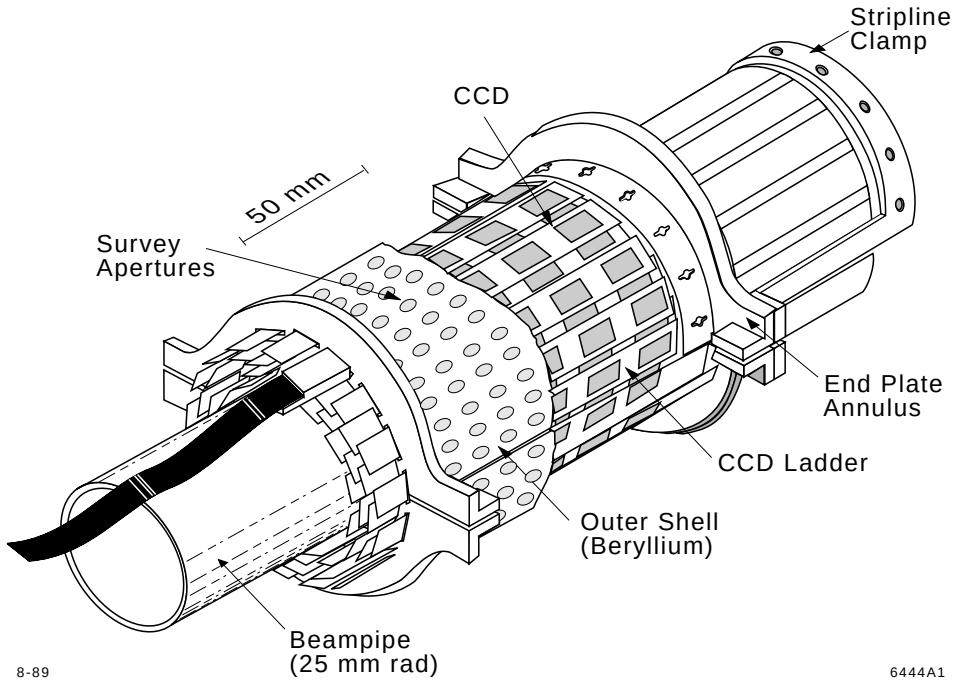

Figure 3.8: The SLD VXD vertex detector.

length (X_0) in material [1]. Inside the inner-most CCD layer is the VXD cooling jacket and the thin beryllium cylinder which serves as the beampipe. The total radiation thickness of the material between the IP and the first CCD layer is .71% X_0.

Triplets, or tracks that have three VXD hits, are used to determine the single hit resolution of the VXD. Figure 3.9 displays the residual of the middle layer VXD hit to the projected point using just the inner and outer VXD hits. After correcting for the resolution of the inner and outer hits, single hit spatial resolutions of $\sim 5\mu$m in the $r\phi$ plane (the plane perpendicular to the electron beam) and 5-9 μm in the rz plane (the plane parallel to the electron beam) have been obtained. In the rz plane,the resolution is dip-angle dependent. For high momentum tracks (muons from $Z^0 \rightarrow \mu^+\mu^-$ events), impact parameter resolutions of ~ 12 μm in the $r\phi$ view and 38 μm in the rz view have been observed [41].

An upgrade of the VXD detector is currently underway. The new detector, "VXD3",

[1] 1 radiation length (X_0) is the mean distance over which a high energy electron loses all but 1/e of its energy by bremsstrahlung [5].

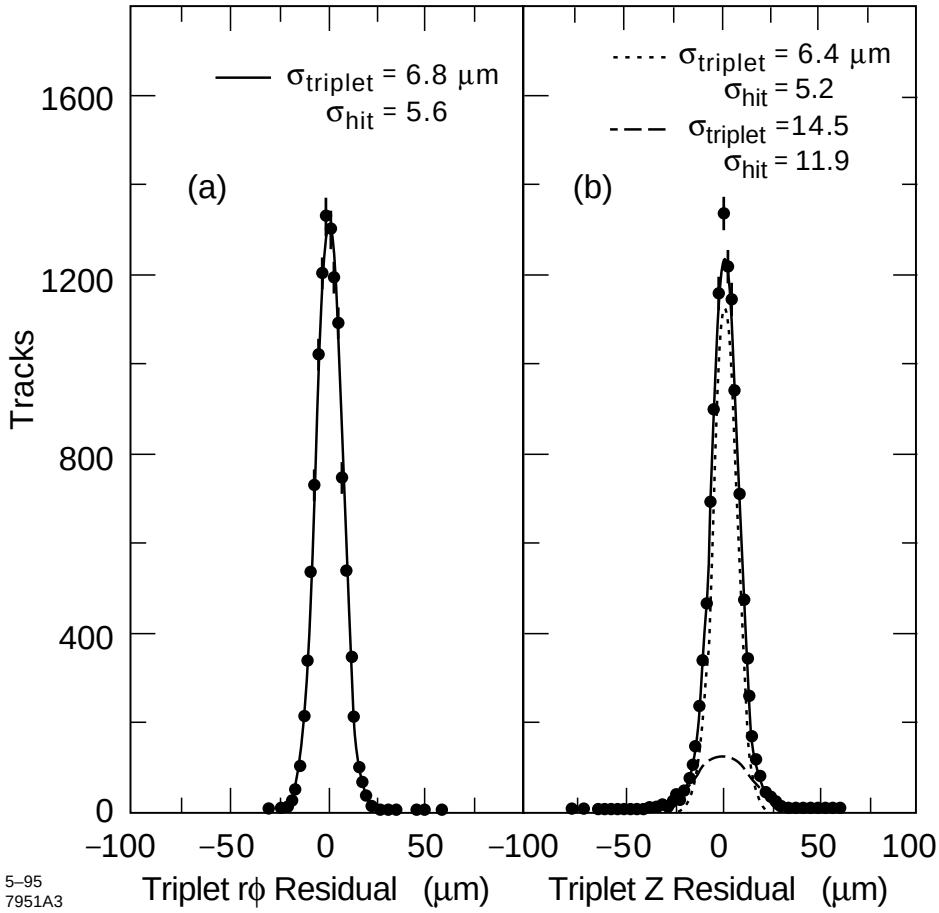

Figure 3.9: VXD single hit resolution in (a) the $r\phi$ plane and (b) the rz plane.

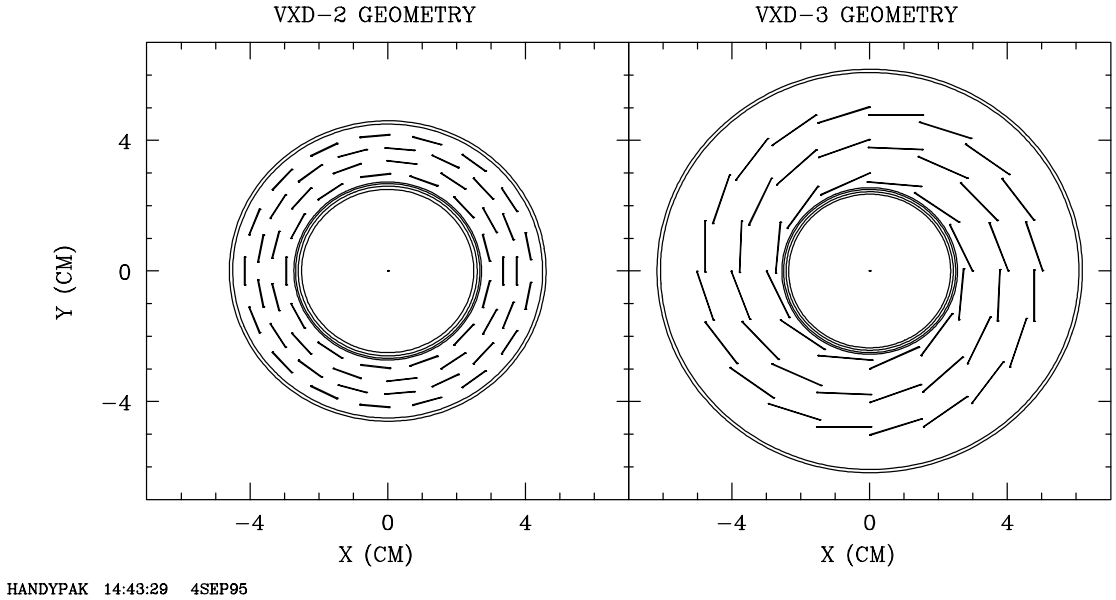

Figure 3.10: An end-view comparison of the current "VXD2" vertex detector and the new "VXD3" tracker. The overlapping CCDs insure that at least three spatial points are obtained for charged tracks that traverse all three layers.

has fully-overlapping layers of CCD ladders in order to provide at least three (well-spaced) spatial points for each charged track. The ladder length is also being increased to provide coverage at lower polar angles. Figures 3.10 and 3.11 compare the end and side views of the older "VXD2" and the new VXD3 tracker. The new tracker is expected to be fully operational for the next physics run, which starts in February, 1996.

3.3.3 The Drift Chambers

There are two separate drift chamber subsystems for the SLD - the Central Drift Chamber (CDC) and the EndCap Drift Chambers (EDCs). The CDC covers roughly 80% of the solid angle ($|cos\theta| < 0.8$), and operates in a uniform solenoidal magnetic field of 0.6 T. It is a cylindrical annulus 2 m in length, with an inner radius of 20 cm and an outer radius of 1 m. It consists of 10 "superlayers" of drift cells, each approximately 6 cm wide by 5 cm high. These superlayers are staggered in orientation (Fig. 3.12): the sense wires in the superlayers are either axial or have a 41-mrad stereo angle with respect to the beam axis.

Each cell contains a set of field shaping wires, guard wires, and sense wires (Fig.

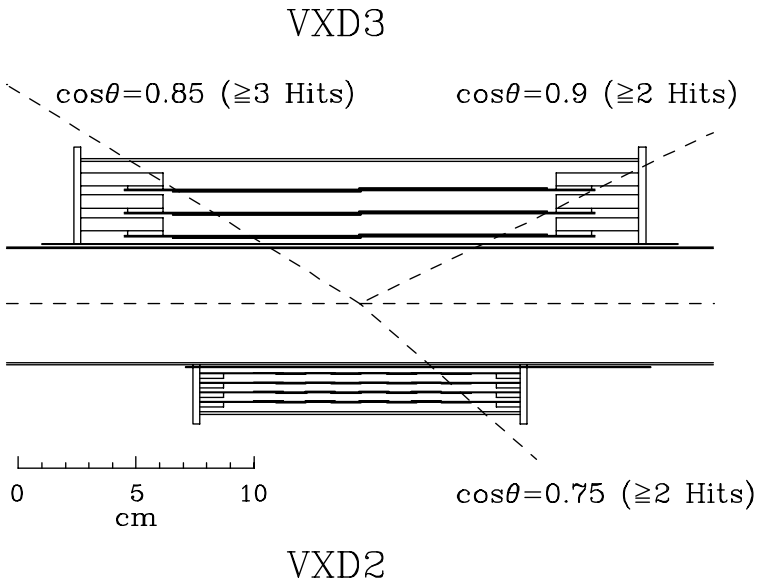

Figure 3.11: A side view comparison of VXD2 and VXD3. The new tracker will provide coverage to higher $\cos\theta$.

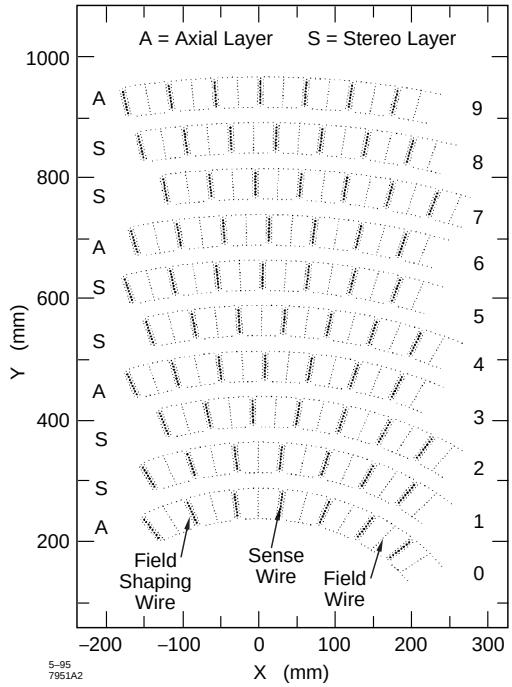

Figure 3.12: SLD's Central Drift Chamber (CDC).

3.13). As the charged track traverses the cell, a trail of ions is produced in the drift gas (a mixture of CO_2 (75%), argon (21%), Isobutane (4%), and water (0.2%)). These ions are directed by the drift field onto the 8 sense wires. The $r\phi$ position of the hit is known from the wire address. These wires are instrumented on both ends, so via charge division an approximate hit position (accurate to about 2 cm) along the sense wire can also be determined. The drift time (the time from e^+e^- collision to the time when the pulse is detected on the wire) indicates the proximity of the track to the single sense wire. Information from the other sense wires in the cell can be used to form an approximate track vector known as a vector hit. As the sense wires in the cell are not staggered, each vector hit has a mirror image on the opposite side. A pattern recognition program is used to combine vector hits from adjacent cells in order to form track candidates. A detailed fit is then performed using individual wire hit information (at this stage, the stereo layer information gives more precise z information), electric and magnetic field variations, and energy loss. The momentum resolution function for the CDC has been measured to be $(dp_t/p_t)^2 = 0.0050^2 + (0.010/p_t)^2$, where p_t is the momentum of the charged track in the plane perpendicular to the beam axis (i.e. the B-field direction) in units of GeV/c. The first term in the resolution function is the multiple scattering error, and the second term is the measurement error term [42].

3.3.4 The Cherenkov Ring-Imaging Detector (CRID)

The Cherenkov Ring-Imaging Detector (CRID) is designed to provide charged particle identification over a large momentum range. As with most components, it is actually divided into a barrel region and two endcaps. Since this author spent a great deal of time working on the hardware for the EndCap CRID (ECRID), additional details about this detector subsystem are described in the next chapter.

The principle by which the CRID(s) operate is fairly straightforward, but it is safe to say that the CRID is the most complicated portion of the detector. For a charged particle traveling with velocity $v = \beta c$ in a medium of index of refraction n, Cherenkov radiation is emitted as long as the velocity is above the threshold $\beta_{threshold} = 1/n$. Such a particle traversing the CRID emits a cone of Cherenkov

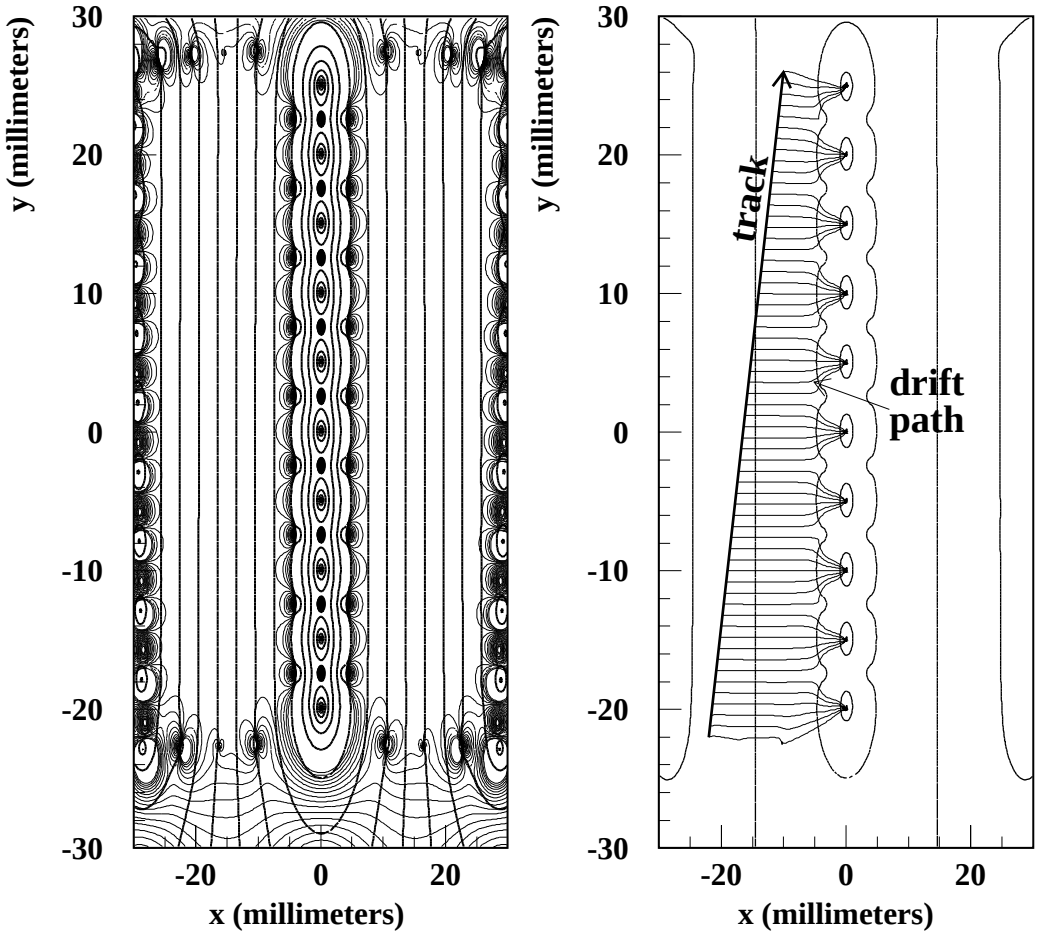

Figure 3.13: The field map for a drift cell of the CDC. The left figure shows lines of constant potential (bold) and lines of constant field strength(thin) within a CDC cell. The right figure shows a drift path of charges caused by the passing of a charged track through the cell.

radiation with polar angle $\cos\theta_c = \frac{1}{\beta n}$ with respect to the charged particle flight direction. The Cherenkov ring emitted strikes a Drift Box (or Time-Projection Chamber - TPC) which is filled with a drift gas (C_2H_6) doped with the photosensitive molecule tetrakis(dimethylamino)ethylene (TMAE). The TMAE can be ionized by photons in the UV; these photoelectrons then drift to a wire plane (MWPC) where they are detected. Through the measurement of their origin coordinates in the TPC (wire number, hit position on the wire (using charge division), and drift time), the Cherenkov angle θ_c can then be measured. Coupling this velocity information with independent momentum measurements from the drift chambers give the particle mass.

The Barrel CRID (Fig. 3.14) contains two radiator volumes: a thin (1 cm) liquid C_6F_{14} radiator (n=1.27802 at λ = 1900Å) and a large ($\sim$ 40 cm average width) gas radiator filled with a C_5F_{12}/N_2 (85%/15%) mixture (n=1.00163 at λ = 1900Å). The higher index of refraction of the liquid provides particle separation at low momenta; the gas radiator allows efficient $\pi/K/p$ separation up to 30 GeV/c (see Table 3.1) [43]. The cone of Cherenkov light emitted by the charged particles in the liquid radiator shine directly onto the drift box. Photons emitted in the gas volume are focussed by spherical mirrors into rings on the drift box (Fig. 3.15).

Radiators	$e^{\pm}$	$\mu^{\pm}$	$\pi^{\pm}$	$K^{\pm}$	$p/\bar{p}$
C_6F_{14}	0.001	0.133	0.176	0.621	1.179(GeV/c)
C_5F_{12}	0.009	1.856	2.451	8.649	16.422(GeV/c)
C_4F_{10}	0.009	1.915	2.530	8.927	16.950(GeV/c)

Table 3.1: Momentum thresholds for producing Cherenkov rings in the CRIDs.

The EndCap CRID (ECRID)

The design of the EndCap CRID (Fig. 3.16) is similar to that of the Barrel CRID except in a few respects. First, the focussing structure for the MWPC had to be modified because, unlike the Barrel, the electrons do not drift parallel to the magnetic field lines. This causes the electrons to impact the detector wires at a large Lorentz angle ($\theta_L \sim 15°$). Second, the decision was made to not build a liquid radiator system.

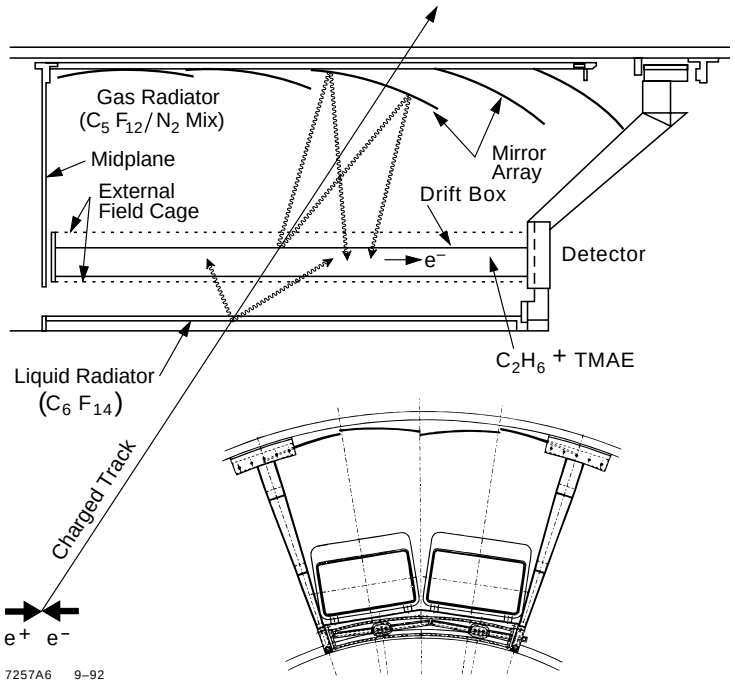

Figure 3.14: The Barrel CRID.

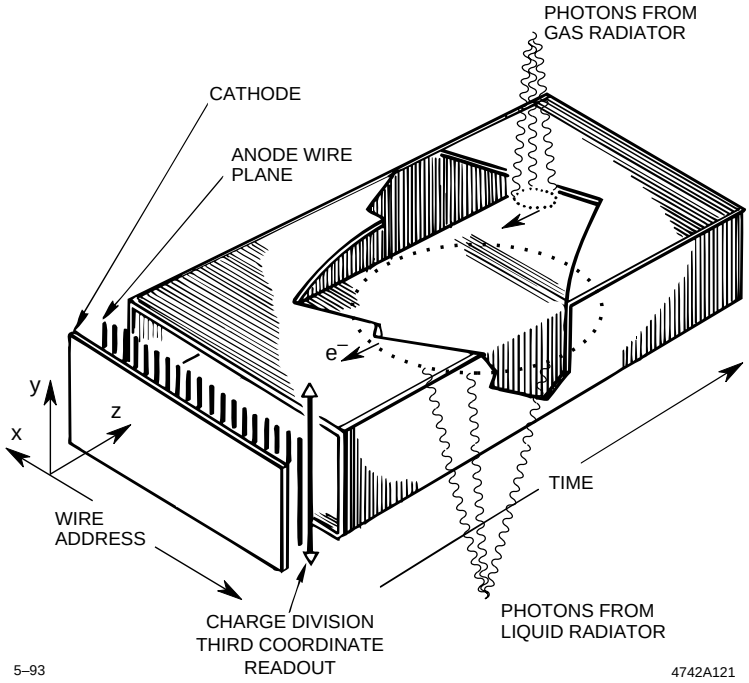

Figure 3.15: A CRID Drift Box, or TPC.

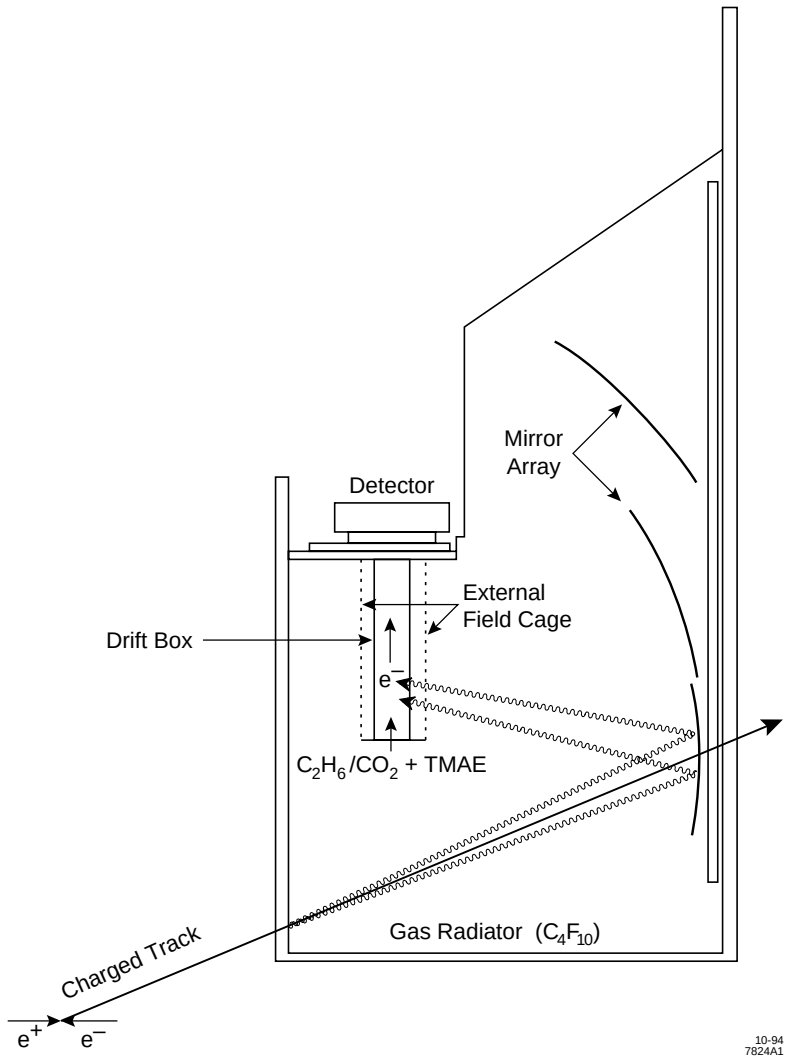

Figure 3.16: The side view of the EndCap CRID (ECRID). Note the lack of a liquid radiator. This greatly simplified the design of the Drift Boxes.

This simplified the TPC design by allowing the use of rectangular drift boxes spaced in azimuth and equipped with quartz windows on only one side (see Figure 3.17). Lastly, the radiator gas used in the Endcap vessels is C_4F_{10}, a material which has the nice operational feature of being gaseous at room temperature. This allowed for a great simplification in the recirculation design. The only drawback is that the index of refraction (n=1.00153 at $\lambda = 1770$Å) is slightly lower than C_5F_{12}, which results in $\sim$ 6% higher momentum thresholds [44].

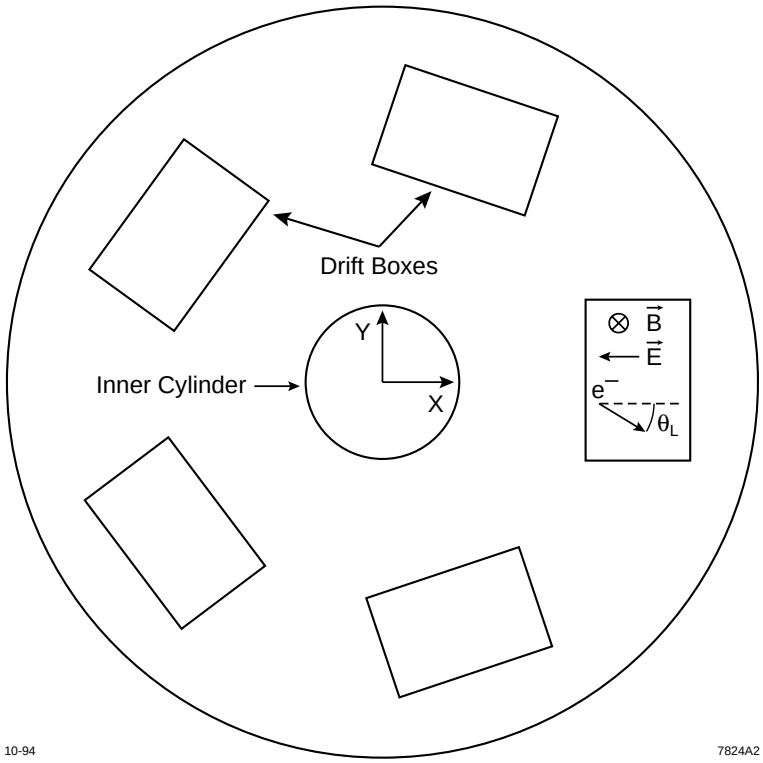

Figure 3.17: The ECRID, viewed perpendicular to the beamline. Unlike the Barrel CRID, the electrons are drifting perpendicular to the magnetic field. This causes the electrons to drift at an angle with respect to the $\vec{E}$ field.

3.3.5 The Liquid Argon Calorimeter (LAC)

The Liquid Argon Calorimeter (LAC) is a lead-argon sampling calorimeter designed to measure the energy of both charged and neutral particles [39]. As with most subsystems, the LAC can be broken into three sections: a barrel and two endcaps. The barrel, which has an inner radius of 1.8 m and an outer radius of 2.9 m, provides continuous coverage between $\theta = 35°$ and $\theta = 145°$ (here, θ is the measured angle with respect to the electron beam direction). The two endcap sections butt against the barrel, and provide coverage between 8° and 35° with respect to the beampipe. Overall, the LAC provides coverage for 98% of the solid angle around the IP.

The LAC has an "onion skin" structure. The two innermost layers are fairly thin, and are designed primarily to measure the energy from electromagnetic showers due to the interaction of electrons or photons. The two outer layers are denser in composition, and are designed to measure the energy in hadronic showers due to the interaction of neutral or charged hadrons. Overall, there are 21 radiation lengths of material in the electromagnetic (EM) sections of the LAC, and 2 absorbtion lengths[2] in the hadronic (HAD) sections. In total, there are $2.8\lambda_0$ of material in the LAC.

The LAC is divided into modules, an illustration of which is shown in Figure 3.18. Each module consists of radial layers of lead and argon. These layers are built out of parallel plates of lead separated from each other by non-conducting spacers and immersed is a liquid argon bath. Particles which interact with the lead produce a secondary shower of low energy particles which then ionize the argon. High voltage is applied to every other layer of lead, producing a field which sweeps the liberated charges out of the argon and onto the opposite layer of lead, which is segmented into square tiles. Several tiles from adjacent layers are electrically connected to form projective towers (units of constant cross-section when viewed from the IP). Each tower is connected to an amplifier to measure the charge deposited. As the argon supplies no charge amplification, the charge observed is proportional to the energy deposited.

[2] 1 absorbtion length (λ_0) is the mean distance over which a high energy hadron loses all but 1/e of its energy due to nuclear interactions [5].

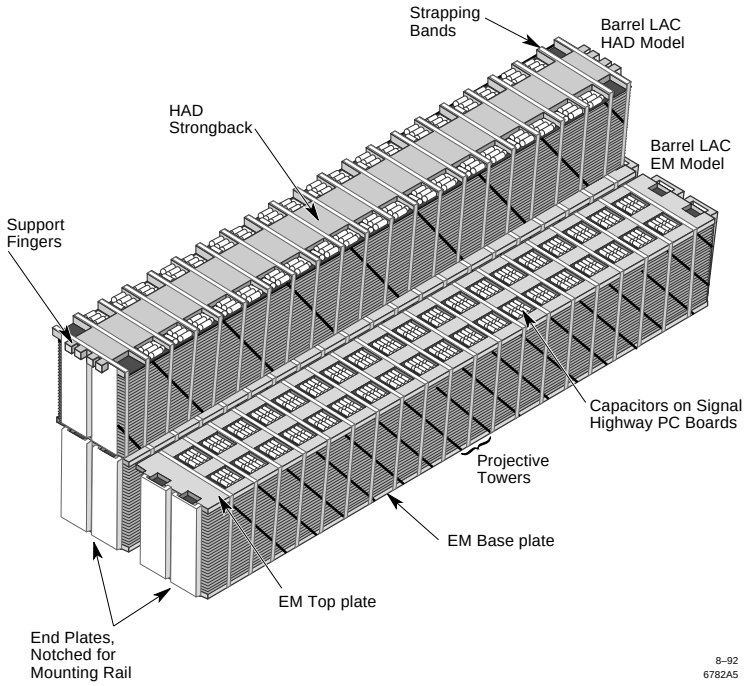

Figure 3.18: View of a LAC module, showing the inner EM and outer HAD sections.

The barrel and endcap portions of the LAC are segmented in polar angle and azimuthal angle, thus allowing for spatial determination of the energy shower. The segmentation and module thicknesses were chosen to maximize the amount of particle energy sampled, and to be able to differentiate between electromagnetic and hadronic particles. The energy resolution of the LAC has been shown to be $\sim 15\%/\sqrt{E}$ GeV for EM showers and $\sim 60\%/\sqrt{E}$ GeV for hadronic showers [45].

3.3.6 The Warm Iron Calorimeter (WIC)

The WIC (Fig. 3.19) serves four functions on the SLD: the flux return for the solenoid; a backing-calorimeter to measure residual hadronic energy that has "leaked" through the LAC; a muon-identification system; and the structural support for the rest of the detector components. The WIC consists of 18 layers of Iarroci streamer tubes sandwiched between 5 cm thick steel plates [12]. These tubes are instrumented with square readout pads for calorimetric purposes, and with long conducting strips in order to perform muon tracking. These strips are laid in two separate arrays at 90° with respect to each other in order to measure the trajectory of the muon in 2D.

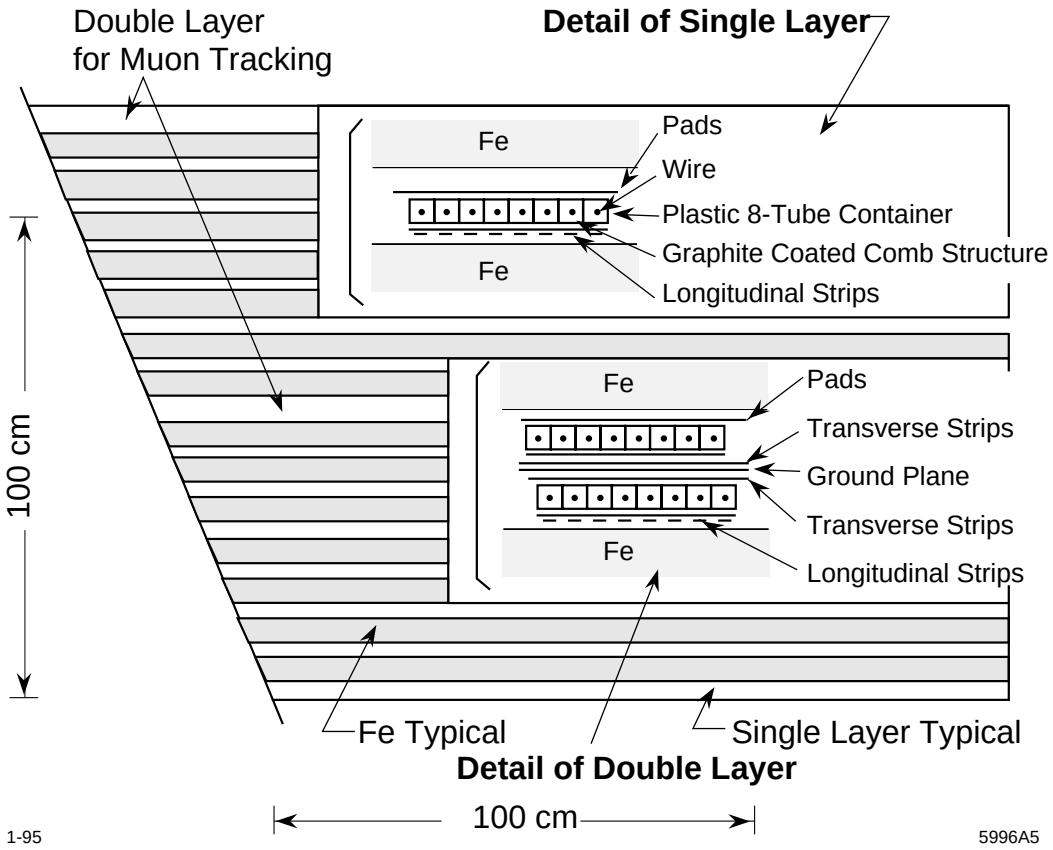

Figure 3.19: Cutaway view of the WIC.

Chapter 4

The EndCap CRID

While the ECRID was not used for the analysis described in this thesis, it was the main project during my first three years of research activity. I had major responsibility for testing of the mirrors, including the design and construction of a semi-automatic vacuum ultraviolet (VUV) reflectometer. During the later stages of the assembly and commissioning of the ECRID, I was given the responsibility of being the EndCap CRID Commissioner. This involved overseeing all work being done on the ECRID. At that time I also completed the radiator gas purification and control system.

The EndCap CRID was designed to extend the particle identification capabilities of the Barrel CRID into the low polar angle regions. The Barrel CRID covers $|\cos\theta| < 0.7$ and the ECRID adds the region $0.82 < |\cos\theta| < 0.98$. The ECRID was made as similar to the Barrel CRID as possible. In particular, the mirror manufacturing and testing procedures were quite similar to those developed for the Barrel CRID. The most significant differences are:

- Liquid radiators were not included in the ECRID. This permitted much simpler (rectangular rather than trapezoidal) and smaller drift chambers, but restricted particle identification to higher momenta ($p > 2.5 GeV/c$ for $\pi^{\pm}$).
- The drift chambers must drift the electrons perpendicular to the magnetic field leading to a different design for the detectors.
- A different gas (C_4F_{10} instead of C_5F_{12}) was used for the radiator.

4.1 The EndCap CRID Mirrors

In this section the fabrication, testing, and installation of the mirrors used to image the Cherenkov radiation into circles in the drift chambers are discussed.

The Rutgers hardware commitment to the ECRID included all aspects of the selection, fabrication, testing and installation of these mirrors into the ECRID vessels (see Figure 3.16); 132 spherical mirrors were produced including 60 per EndCap and 12 spares. In the ECRID mirror geometry, the mirrors are arranged on pie-shaped support frames, with 10 frames per endcap. As there are five drift boxes per endcap (Fig. 3.17) half of the mirror frames are "centered" (i.e. they reflect onto a drift box directly in front of them) and half are "offset" (i.e. they reflect onto drift boxes on either side). Twelve different mirror shapes with three different mirror radii were used.

4.1.1 Glass Manufacturing Techniques and Quality Control Tests

The specifications for the mirror blanks (uncoated glass) indicated that the physical dimensions had to pass fairly tight tolerances to obtain maximum coverage without interference between the mirrors. Also, the polished surface was required to have a very smooth finish so that scattering of light would be limited to a few percent. Having maximal reflectivity while minimizing the scattered fraction was important due to the small number of reconstructed Cherenkov photons from a charged track (typically 9-10 γ's for $\beta \sim 1$ particles). The selected vendor, Lancaster Glass Company[1], was the same manufacturer that furnished the glass for the 400 barrel CRID mirrors.

The mirrors were formed using 6 mm-thick soda-lime glass that was heated until soft and *slumped* - pulled under vacuum into spherical molds of approximately the correct radius. For the ECRID, three different mirror radii were used: 88.8 cm, 120.2 cm, and 130.0 cm. These mirror blanks were then cut into trapezoidal shapes of varying dimensions (see Figures 4.1 and 4.2 for two examples of the twelve mirror shapes required), and the edges were beveled slightly. The mirrors were then placed on polishing spheres of the correct radius, and the concave surfaces were polished until they were

[1] Lancaster Glass Company, Lancaster, Pa. 43130

judged to be smooth by visual inspection. The mirrors were then sent to Rutgers for more rigorous quality control checks (below).

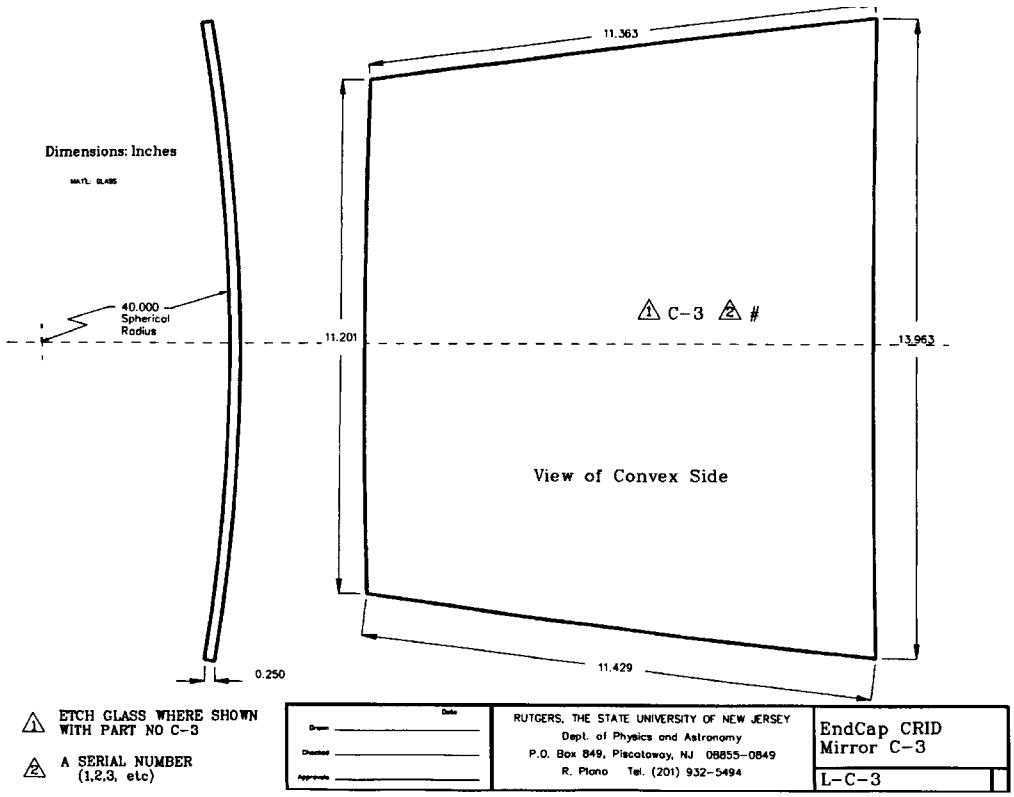

Figure 4.1: An example of a trapezoidal mirror used in the ECRID. This shows the dimensions for one of the large Centered-Frame mirrors.

During testing of the first shipment of mirror blanks to arrive at Rutgers, it became evident that significant rounding of the edges was taking place, thus losing a large fraction (up to 10%) of the mirror surface for useful reflections. This rounding problem was eventually traced to the polishing procedure described above: as the polishing surface would rotate on the concave side of the mirrors, polishing rouge would collect along the edges of the glass and grind them away. Once the problem was understood, it was remedied by mounting discardable "outriggers" of glass next to the edges of the mirror, and then simultaneously polishing the entire arrangement. Thus, the edge grinding would primarily affect the discardable pieces. This procedure was shown to be acceptable, and the faulty mirrors were repolished until the edge rounding was negligible.

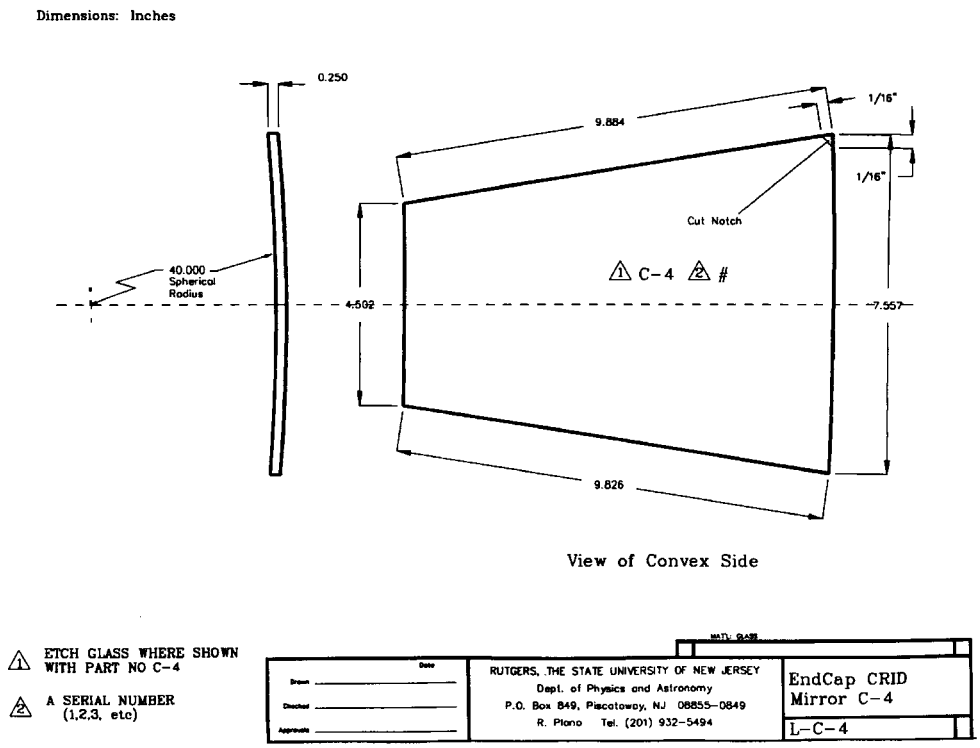

Figure 4.2: An example of a trapezoidal mirror used in the ECRID. This shows the dimensions for one of the small Offset-Frame mirrors.

Glass Roughness Checks

It was desired that the mirror surfaces be polished to a smoothness of a few nanometers (rms) to minimize light loss due to scattering. The surface profiles of 90% of the uncoated mirror blanks were measured using a WYCO surface profilometer. This device measured the relative height of the glass surface using optical interferometry. Thus, no physical contact with the mirror surface was necessary. At each of three (or more) locations on the mirror surface, profile measurements were made at 1024 points equally spaced along a straight line approximately 5 mm long.

The raw profilometer output showed the overall spherical curvature of the glass surface, as shown in Figure 4.3. A second order polynomial fit was used to remove the overall curvature, revealing the residual roughness of the surface, as shown in Figure 4.4, in this instance with an rms of 55.8 Å(5.58 nm). In adopting a selection criterion on maximum acceptable roughness we noted that there was an ambiguity in a specification on rms alone, unless the length of the surface over which the measurement was made

was also taken into account. We investigated this dependence using a Fourier transform of the residual roughness data to extract the contribution to the overall roughness as a function of the distance scale over which the roughness was viewed. The results corresponding to the data in Figure 4.4 are shown in Figures 4.5 and 4.6. Figure 4.5 shows the incremental contribution to the overall roughness as a function of distance on the glass surface. This is integrated in Figure 4.6 to show the dependence of the rms roughness on the distance over which the roughness is measured.

We elected to specify the acceptable roughness as being that measured over distances less than 160 μm on the mirror blanks' surface. This was motivated by our specifications on the angular dispersion (from all sources) to be less than 1 mrad; when treating the surface as a diffraction grating, a pitch of greater than 160 μm would produce a diffraction peak within 1 mrad of the (specular) reflected image. The maximum allowed rms over a distance of 160μm was set at 30 Å. Initially, a large fraction (26/97) of the uncoated mirrors were rejected due to surface roughness; eventually the manufacturer's polishing and handling procedures were modified to ensure 100% acceptance.

Optical Distortion Checks of Glass Blanks

Prior to coating, the radius of curvature of the mirror blanks was measured and the amount of optical distortion arising from deviations of the surface from a perfect sphere was determined. This was done with the apparatus shown schematically in Figure 4.7. The mirror was placed concave surface up in a shallow container of water with the back surface of the mirror blank submerged (but not the front surface); the index of refraction of water is close enough to that of glass so that reflections from the back surface of the blank were negligible. A mask consisting of a square grid of accurately positioned holes was placed on top of the mirror blank and illuminated with a point source of light; the reflected image of the mask was viewed on a frosted glass screen held the same distance from the mirror blank as the point light source. To determine the radius of curvature, the position of the point source/viewing screen assembly was adjusted until the reflected image was as small as possible, and the distance from the assembly to the mirror then measured. It was possible in this way to measure the radius

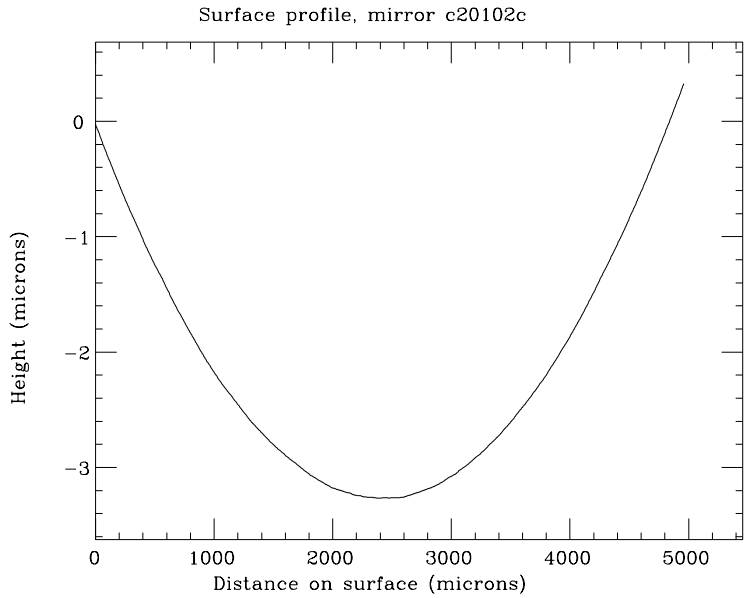

Figure 4.3: The raw surface profile for a typical ECRID mirror blank, before removing the overall curvature.

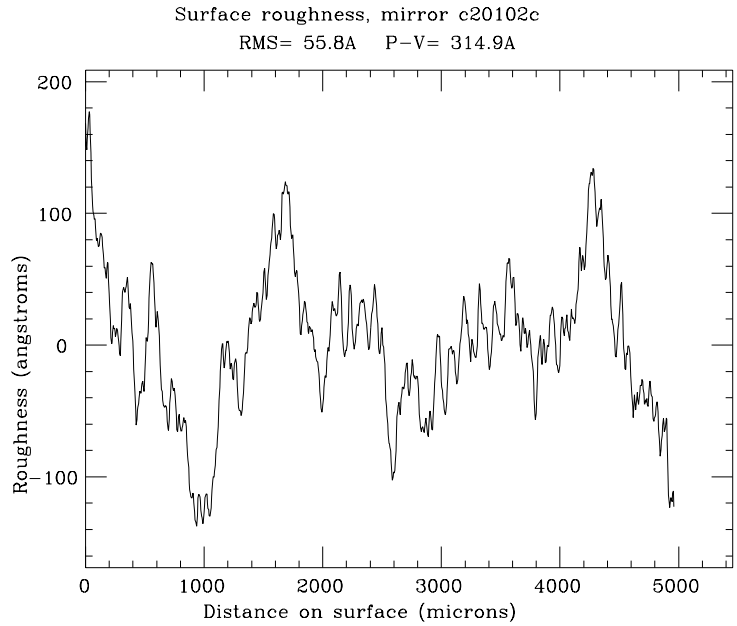

Figure 4.4: The surface profile for a 5 mm strip, after removing the overall curvature.

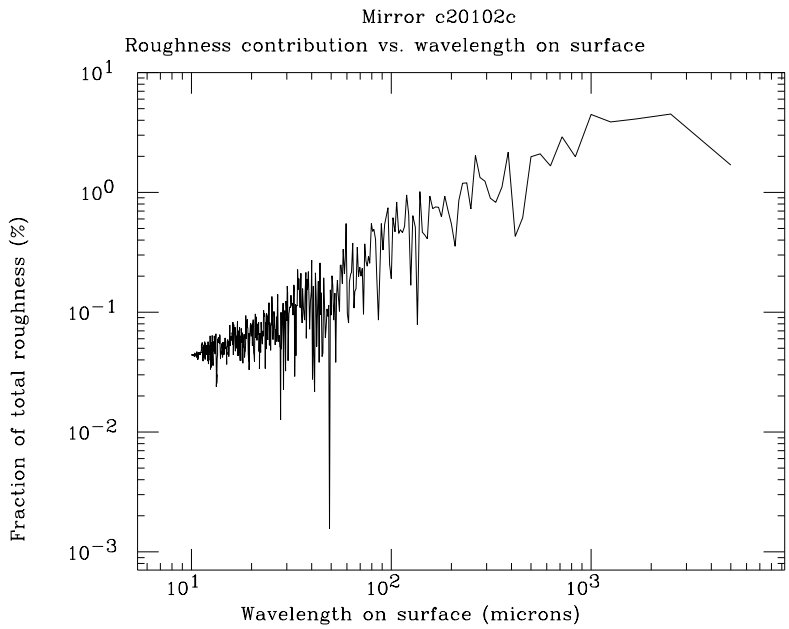

Figure 4.5: This shows the wavelength components over the 5mm length of the surveyed strip. Note that the largest contributions to the roughness are due to long wavelength components ($\lambda \sim 1mm$).

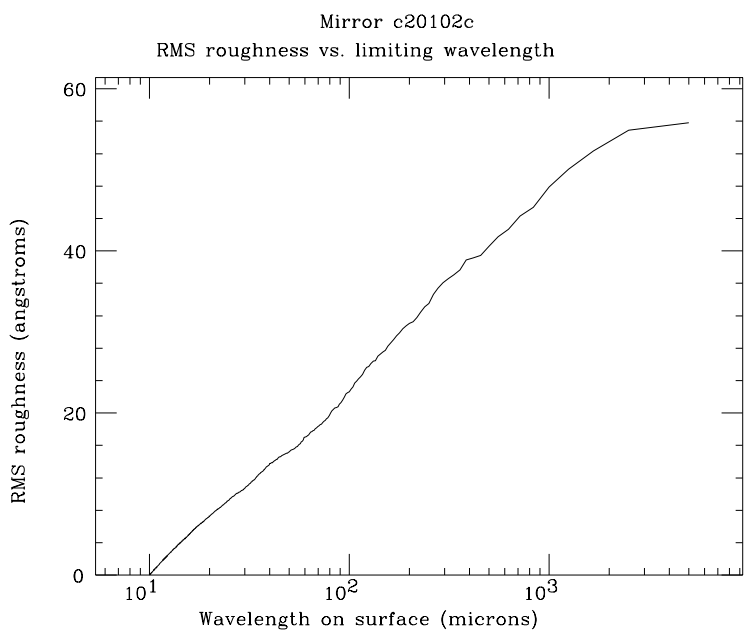

Figure 4.6: This shows the change in the integrated roughness for the 5mm surveyed strip as the the maximum allowable wavelength component increase. For this mirror blank, the total integrated roughness for the strip when considering all components up to 160 μm is 28 Å. The design criterion was 30 Å.

of curvature to within a few millimeters; the specified tolerances on the mirror radii were ± 15 mm.

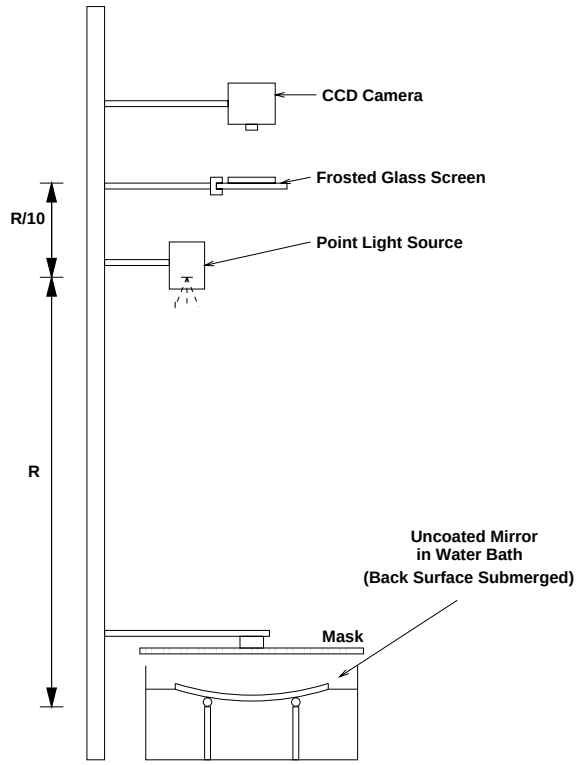

Figure 4.7: Apparatus used to determine the optical distortion from each mirror blank. Note that the uncoated mirror rests with its back surface immersed in water. The apparatus was used in this configuration to measure the optical distortion of the mirrors. To measure the radius of curvature of the mirror, the point source and a glass screen mounted alongside were moved downward until the reflected image was as small as possible. This gave the focal length of the mirror, and thus the radius.

After determining the radius of curvature, the frosted glass viewing screen was moved out of the way and the reflected image viewed on a second frosted glass screen placed above the point light source and approximately 1/10th as far from the point source as the mirror blank. The image of the mask formed on this frosted screen was observed with a video camera which was connected to a "frame grabber" system which digitized the image. This digitized image was used as input to image processing software which determined the locations of the images of the mask holes. A least-square minimization procedure was then used to determine the best fit of the images to a square grid, and an average and maximum residual deviation in milliradians from the image that would have been produced by a perfect sphere were calculated. (Since the

point source and viewing screen were not exactly collinear the expected image deviates from an exactly square array. The extent of that deviation was investigated using ray-tracing, and was determined to be negligible in comparison to the deviations produced by distortions of the mirror blank.). The linearity of the video system was checked periodically by replacing the frosted glass screen with a rendering of an accurately spaced array of dots. Deviations from linearity were also negligible in comparison to the distortions being measured. This also served to calibrate the system.

The distortion measurements thus made were accurate to ~ 0.1 milliradians. Mirror blanks were required to have an average residual deviation of no more than .5 mrad, and a maximum residual deviation of no more than 1.0 mrad. A large fraction ($\geq 90\%$) of the mirror blanks passed these criteria, and the remaining were returned to the manufacturer for repolishing.

After certifying the optical quality of the glass blanks, small ($\sim$ 5mm $\times$ 5mm) indium pads were ultrasonically soldered onto the front surface of the mirror and grounding wires attached. Typically, these pads were placed near a corner of the mirror, at a location that would later be covered by the mounting clips (described below). This was done to minimize the amount of "wasted" surface area and maximize the number of reflected photons. After coating, these wires would be used to electrically ground the metallic mirror coating to the support frame.

4.1.2 Coating and Reflectivity Tests

The aluminum coating was applied by Acton Research Corporation (ARC)[2], the same vendor who coated the barrel CRID mirrors. This coating was chosen by the barrel CRID group after extensive testing of various manufacturers' coatings [46].

Coating Process

Before coating, the mirror blanks were cleaned by conventional chemical methods. The concave surfaces of the mirror substrates were coated by evaporating approximately 80

[2] Acton Research Corporation, Acton, Ma. 01720.

nm of ultra-high purity aluminum, followed by 40 nm of magnesium fluoride overcoat (MgF_2), in a high-vacuum environment (approximately 10^{-7} Torr). The mirrors were held by their edges with friction clamps so that no shaded areas were left on the mirrors. The aluminum was deposited in a few seconds and followed immediately by the MgF_2 to minimize the oxidation of the reflective coating. After coating, the mirrors were shipped to Rutgers and stored in a dry-air clean room[3] until testing.

Reflectivity Testing of Coatings

One spherical mirror and one planar "witness coupon" ($5.1 \times 5.1\ cm^2$) were coated in each batch by Acton (except when two small mirrors were coated together). The reflectivity of the witness coupon was measured by the vendor using the Acton Model VRTMS-502 Vacuum Measurement System at 10 wavelengths ranging between 160 and 230 nm. The coating specifications were stated to be a minimum reflectivity of 80% at 160 nm, increasing linearly to 85% reflectivity at 180 nm, and remaining constant at 85% reflectivity to 230 nm. If the reflectivity of the witness coupon was above the minimum specifications, the mirrors were assumed to be acceptable and the mirrors and coupons were shipped (the Acton VUV reflectometer was not large enough to test the full-sized spherical mirrors). When received at Rutgers, the mirrors were inspected for visible surface flaws and, if found acceptable, then stored in a dry-air clean room with less than 30% relative humidity at 23° C until reflectivity tests could be performed. Approximately five mirrors were rejected due to coating blemishes and returned to Acton. Acton's procedure was to make a precise mapping of the surface flaws, strip the coating and apply a new coating. A reappearance of the blemish on two of the mirrors indicated a substrate flaw, while the lack of blemishes on the rest indicated cleaning errors by Acton. The mirrors that had substrate flaws (e.g. small "pin-prick" dimples on the front surface) were set aside for spares.

The reflectivity of each full sized spherical mirror was measured at Rutgers over 10

[3] MgF_2 is hygroscopic, so water molecules are easily absorbed by the coating. As water strongly absorbs VUV light, it was crucial to keep the mirrors as dry as possible.

different wavelengths ranging from 160 to 230 nm. A semi-automated custom instrument (Fig. 4.8) was designed and constructed to measure the (absolute) reflectivity of each full sized mirror in a vacuum environment. A McPhearson 218 vacuum UV monochromator with a deuterium lamp directed a narrow beam of light onto a rotatable mirror which would first reflect the light directly onto a p-terphynl plexiglass window coupled directly to a photomultiplier tube. After measuring the incident intensity of the VUV light, the mirror would then rotate to reflect the light onto the spherical test mirror which would then focus the light onto the plexiglass window. By taking the ratio between the incident (I_i) and the reflected (I_r) light intensities, an uncorrected mirror reflectivity could be calculated:

$$R(\lambda) = \frac{I_r(\lambda)}{I_i(\lambda)}. \tag{4.1}$$

The full-sized mirror could be pivoted about its center of curvature and rotated about its center point, allowing any point on the mirror surface to be tested. At each wavelength, at least seven positions on the full sized mirror were tested: the center point and two concentric circles(Δr = 2.5 to 4.0 cm) of three points each. A third ring of three points was also tested on the larger mirrors. The positioning of the test mirror and light intensity measurements were computer-controlled via CAMAC (as was the data-acquisition), while the changing of the wavelength and the positioning of the rotating mirror was controlled manually. The incident light intensity was measured at the beginning and ending of each wavelength test sequence to monitor drift in the deuterium lamp output. The spherical mirror was tested first at 160 nm, then at 230 nm, and then in decreasing wavelength increments with a final test at 160 nm to monitor any change in the test environment.

During early tests it became apparent that a design flaw in the reflectometer was lowering the reflected light intensity over all wavelengths and most noticeably in the 160-180 nm region (Fig. 4.9). In Figure 4.8 it is apparent that there is a difference in path length ($\Delta l \sim 25$ cm) for the reflected light with respect to the incident light. This introduced an additional attenuation of the reflected light which manifested itself as a

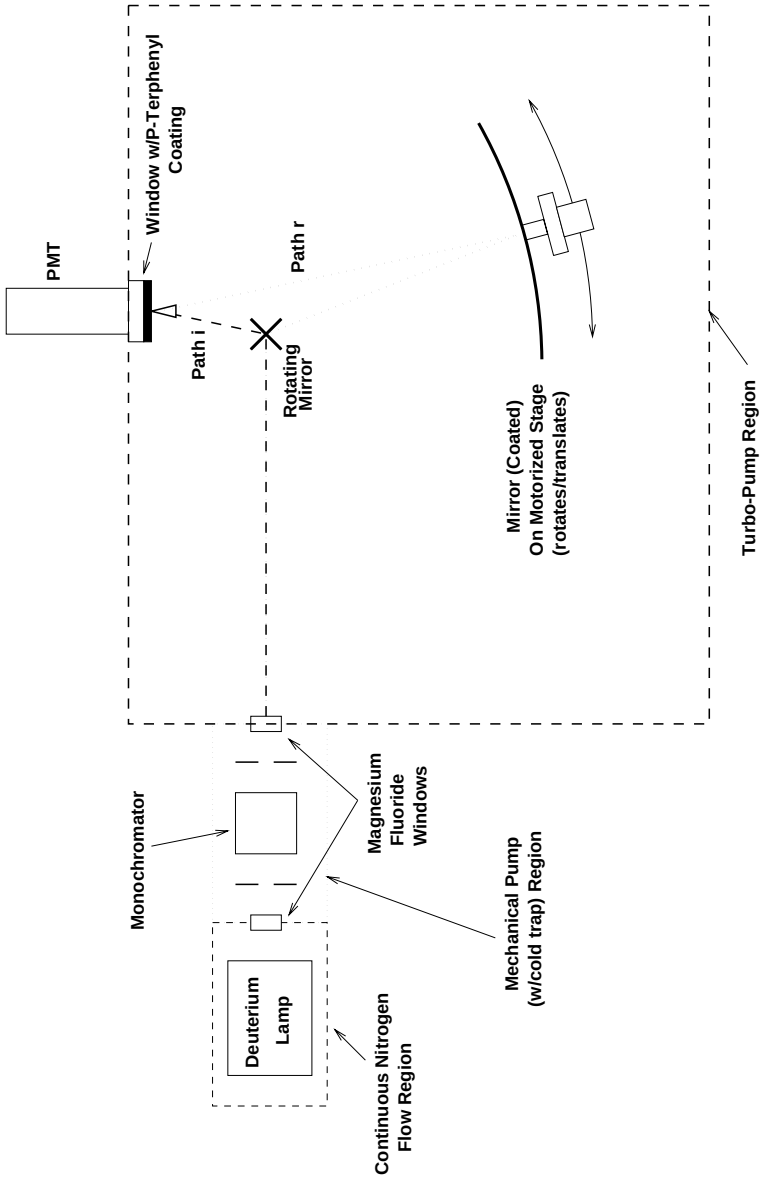

Figure 4.8: The VUV reflectometer used to test the reflectivities of the full-sized mirrors. Note the difference in optical path length for the incident (i) light and the reflected (r) light, $\sim$ 25 cm. The typical operating pressure for the main test vessel was 0.1 Torr.

lowered mirror reflectivity:

$$R(\lambda) = \frac{I_r(\lambda)}{I_i(\lambda)} e^{-\frac{\Delta l}{l_0(P,\lambda)}}; \tag{4.2}$$

where $l_0(P, \lambda)$ is the pressure and wavelength dependent absorption length for the remaining gas in the reflectometer.

As it was impossible in the time available to modify the apparatus to correct this problem, it was decided to calibrate the instrument by interspersing 20 witness coupon tests (tested by manufacturer) with full sized mirror tests. Various witness coupons were measured by separate instruments at Acton Research and by University of California - Santa Barbara (UCSB) to verify the quoted reflectivity [46]. Figure 4.11 shows the amount of reflectometer error as a function of wavelength. The fully corrected reflectivities for 129 of the 132 full sized mirrors is shown in Figure 4.12 (3 mirrors were untested due to time constraints and held for spares).

4.1.3 Design and Assembly of the Mirror Frames

As part of the overall design of the EndCap CRID mirror system, the desired location of each mirror was precisely calculated. To simplify the design and make it more rugged (and foolproof), it was decided to not allow small adjustments to the mirror positions. While in a dry room at Rutgers, the mirrors were mounted in groups of 6 on V–shaped frames constructed from aluminum box girders (Figures 4.13 and 4.14). The mirrors are held pointed in the desired directions atop aluminum posts which are capped with plugs machined so that their surfaces are tangent to the underside surface of the mirrors at the point of contact. The mirrors were glued against the plugs, and also pulled against them using small stainless steel clips which extend slightly over the edge of the mirror and are clamped to the aluminum post. A supplemental restraint system was also attached. This was composed of small clips attached at two points on each mirror's perimeter; these clips were held in tension with spring loaded constraining wires. Soldered wires grounded the mirror's coating to the mirror frames.

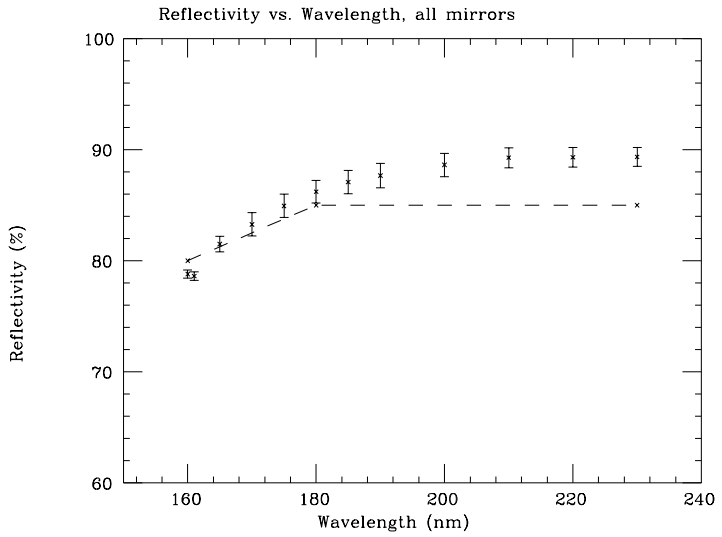

Figure 4.9: The average reflectivity of the mirrors used in the ECRID, including spares. The two points at 160 nm indicate a small change in the testing conditions over the course of the reflectivity survey. The dashed line indicates the minimum acceptable reflectivity.

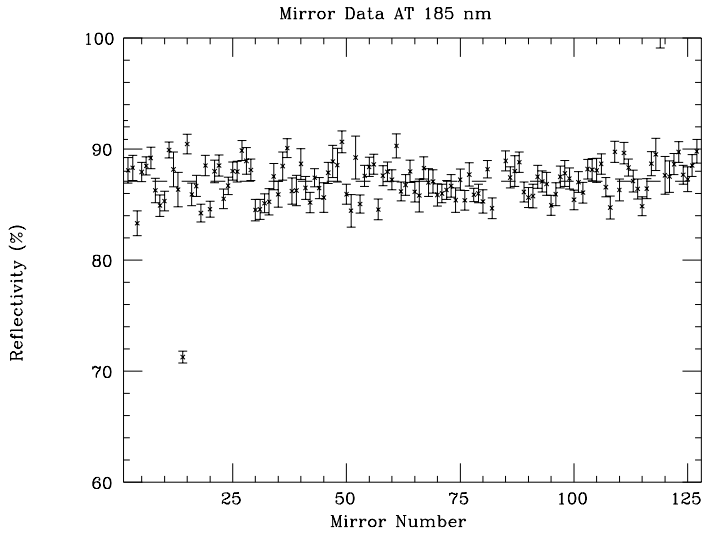

Figure 4.10: An example of the mirror-to-mirror variation in reflectivity. In this case, the measurements are for 185 nm. The mirror whose reflectivity at this point was $\sim 70\%$ was damaged by oil-vapor contamination. It was not installed in the ECRID.

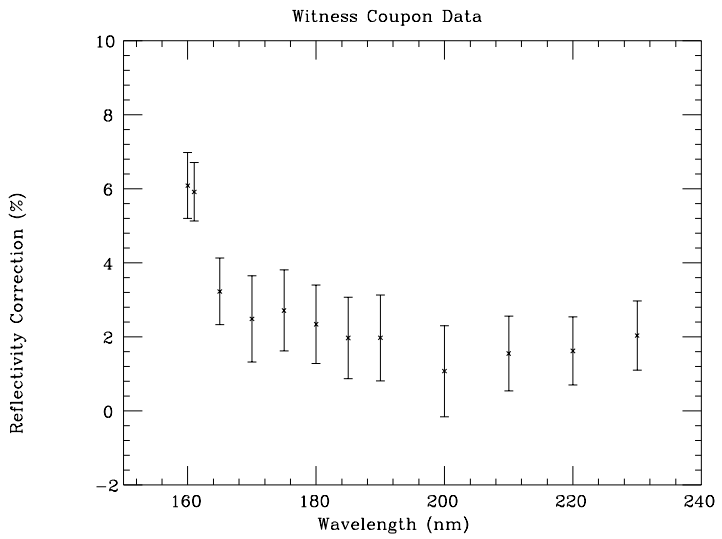

Figure 4.11: The calibration corrections applied to the reflectivities displayed in Figure 4.9. An overall normalization uncertainty of 2% is not shown.

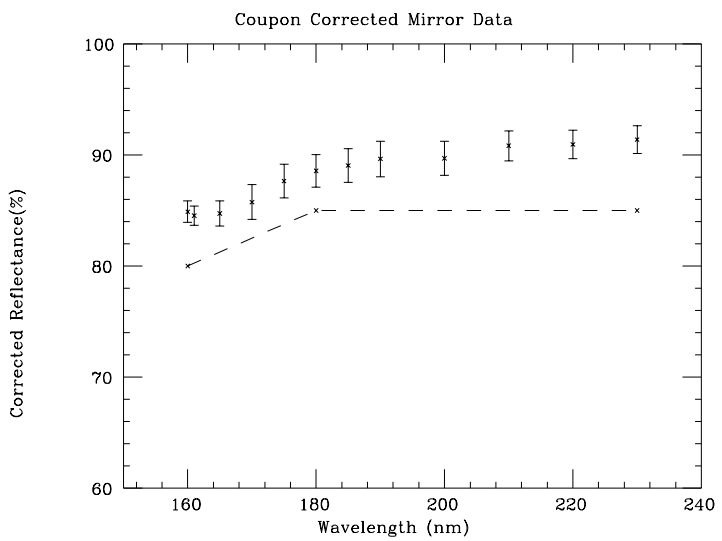

Figure 4.12: The average reflectivity of the mirrors used in the ECRID, after correcting for reflectivity bias. The dashed line indicates the minimum acceptable reflectivity. An overall normalization uncertainty of 2% is not shown.

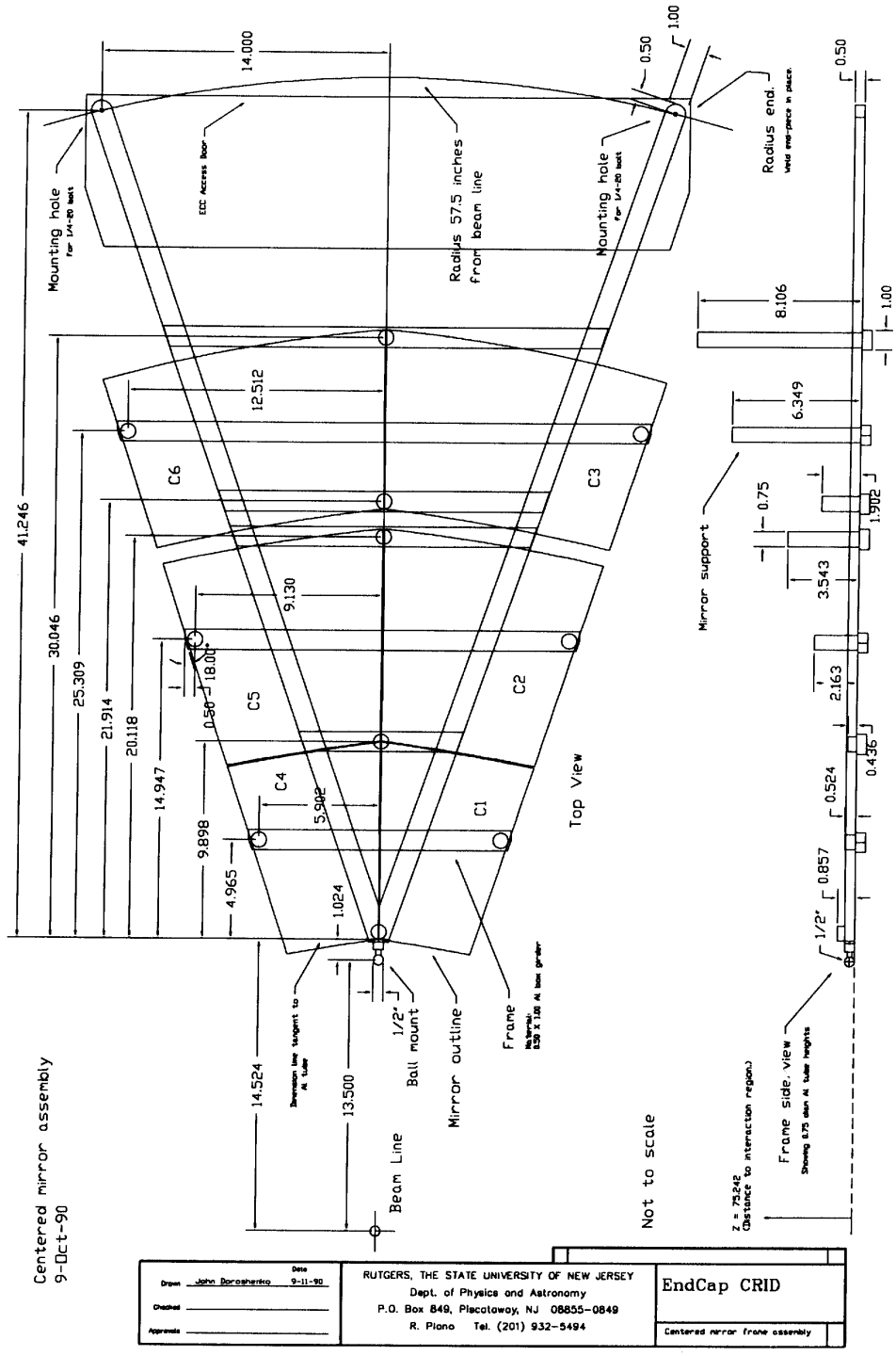

Figure 4.13: A drawing of the frames used to support the Centered Mirrors - the mirrors that focussed the Cherenkov rings onto drift boxes mounted directly in front of the mirror frame.

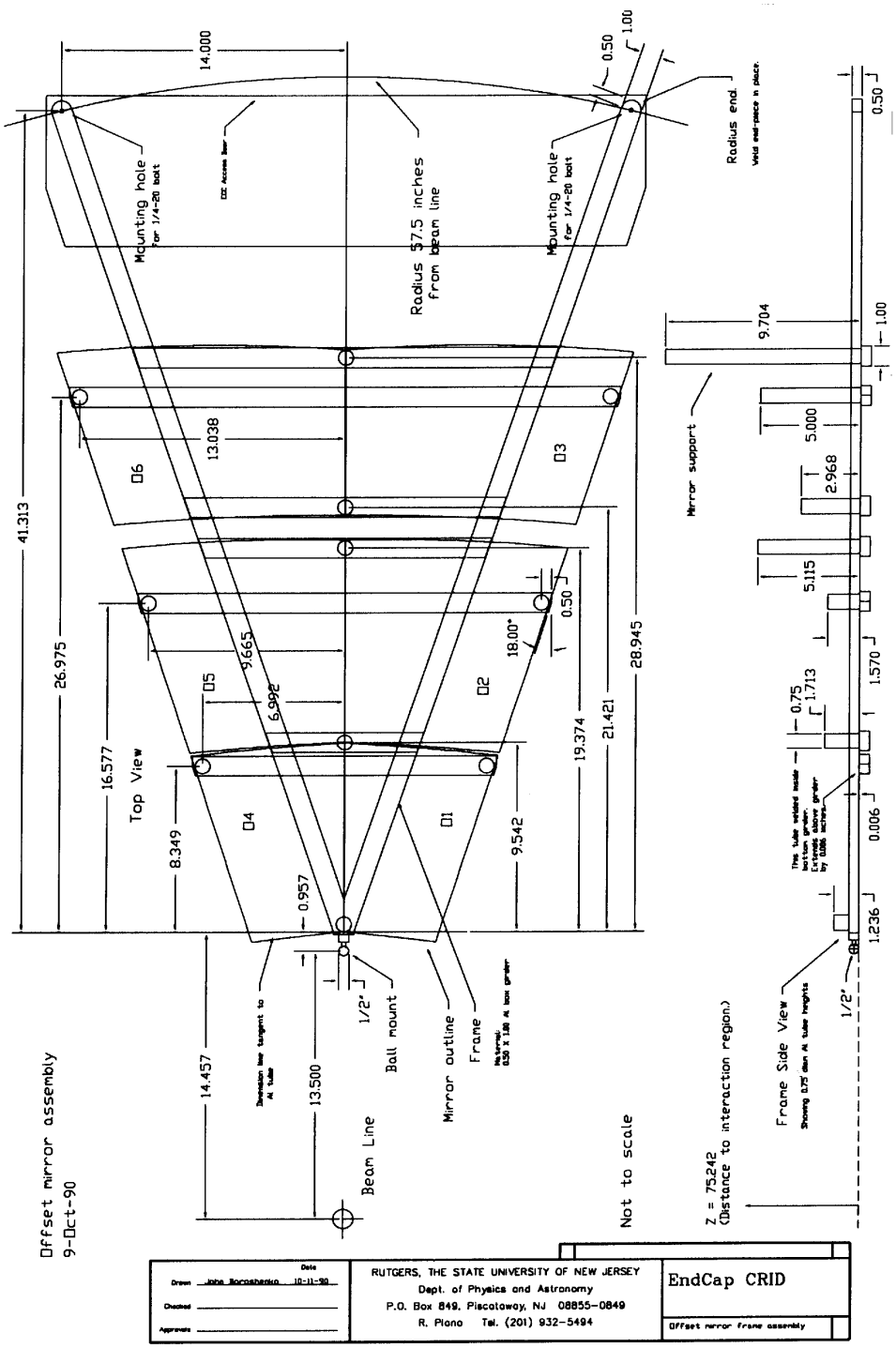

Figure 4.14: A drawing of the frames used to support the Offset Mirrors - the mirrors that focussed the Cherenkov rings onto drift boxes mounted on either side of the mirror frame.

4.1.4 Frame Installation and Survey

The assembled frames were packed in nitrogen-filled bags and protected by custom–made shipping containers designed to absorb vibrations. They were shipped to SLAC via air-freight, and stored in the SLD Collider Hall until installation. Except during the shipping itself, the mirror shipping containers were attached to a dry nitrogen source to keep the mirrors in a dry environment.

The mirrors were installed inside the ECRID vessels using a semi-flexible insertion tool designed to support the mirror frames while protecting the mirror surfaces. During the installation procedure, the EndCap vessels were surrounded by dry/clean-room assemblies. Ten frames were installed per EndCap, alternating Centered and Offset frames.

After the installation, the mirrors were surveyed *in situ* using a survey device modified from the UCSB apparatus used for the BCRID survey. This survey tool was mounted in the positions which the drift boxes would later occupy. The tool consisted of a laser on a movable motorized platform whose location in x and y was digitized via linear encoders. The laser was attached to a two axis rotating platform with encoders which digitized the pointing direction in θ and ϕ. The laser had an array of photosensitive diodes attached to its front end. In the surveying process, the laser was positioned at an $x - y$ position selected from a previously computed chart, and the pointing direction of the laser was adjusted until the reflection of the laser light from the mirror surface produced a signal minimum in the photodiode array.

The resulting x, y, θ, and ϕ values defined a ray in space which passed through the center of a sphere, of which the mirror surface was a segment. On average, 6 such measurements were made for each mirror, and a least squares fit was done to determine the best estimate for the center of the sphere. The typical rms error on the sphere center was 2 mm [47].

4.2 The End Cap CRID C_4F_{10} Gas System

The initial design for the CRIDs called for the Barrel and the EndCaps to all be connected to the same radiator gas recirculation system, which would recirculate and filter the fluorocarbon compound C_5F_{12}. However, due to operational complications with the Barrel CRID gas system, it was later decided to build a separate radiator gas system for the EndCaps.

For the EndCap gas radiator system, we opted for C_4F_{10}[4], a material that had previously been considered too expensive for use in the CRIDs[5]. Some advantages of C_4F_{10} over C_5F_{12} are its lower condensation point ($-2°$C vs $30°$C)[6] and its higher transparency in the range $\lambda \simeq 160 - 180$nm, where the quantum efficiency of photosensitive TMAE is the highest. However, the index of refraction for C_4F_{10} ($n = 1.00153$ at $\lambda = 1770$ Å) is slightly lower than for C_5F_{12}, resulting in momentum thresholds $\sim$ 6% higher (see Table 3.1).

There were two requirements that had to be met for a successful radiator gas system: (i) the pressure must be held very steady ($\pm$ 0.2 torr) in order to keep from damaging the quartz-windowed drift boxes (Fig. 3.15); (ii) the gas must be very clean in order to keep UV absorption to a minimum. As even small quantities (few ppm) of O_2 can be detrimental to the UV transmission, it is necessary to recirculate the C_4F_{10} through the EndCap gas volumes (2650 liters/EndCap) fairly often to "sweep" out the contaminants.

After building two small bench models to test various aspects of the design, the full scale gas system, shown schematically in Fig. 4.15, was erected. The ECRID radiator gas system is a closed loop recirculation system which maintains the vessel pressure by controlling the C_4F_{10} vapor pressure inside a condensing tank[7] which contains $\sim$ 25

---

[4]Perfluorobutane, Developmental Product L-11667,3M Co., St. Paul, MN 55144, USA.

[5]Due to increase industrial production of this material as a "ozone-friendly" replacement for Halon, the price dropped $\sim$ 50%.

[6]The barrel CRID currently uses a C_5F_{12}/N_2 mixture as radiator gas to avoid the risk of condensation.

[7]Where possible, standard commercial items were used in order to keep costs down. In this instance, the condensing tank is a stainless-steel 40 gallon beer keg.

liters of liquid C_4F_{10}. This condensing tank, which is held inside a commercial freezer, has several low-mass kapton/foil heaters (300W capacity) placed inside it. Electronic signals from pressure transducers[8] mounted on the ECRID vessels are fed into a microprocessor control unit, which controls the amount of heat delivered to the condensing tank. When the vessel pressure is below the nominal set value (1.9 torr above atmospheric), additional heat is delivered to the liquid which then vaporizes some of the fluorocarbon and raises the vessel pressure. To lower the pressure, the amount of power to the heaters is lowered (typically, $\sim$ 100 watts of heating power is continuously being applied). The condensing tank effective temperature must be maintained constant to about 0.01° C to keep the C_4F_{10} pressure constant to 0.2 Torr.

The above design is further complicated by the second design requirement discussed above: the radiator gas must be recirculated and purified in order to keep the amount of UV-absorbing contaminants to a minimum. C_4F_{10} gas is injected into the vessel at the rate of $\sim$ 5 liters per minute. Simultaneously, this amount of gas is condensing into the above-mentioned tank. Periodically, the excess liquid from this tank is pumped out and introduced into a liquid filtration system. After multiple passes through the Silica Gel[9] and Ridox[10] filters (to remove H_2O and O_2 contaminants), the liquid is vaporized, filtered for a final time and then reintroduced into the vessel. Figure 4.16 shows the improvement in the C_4F_{10} transparency after this filtering process is completed.

Stable operation of the radiator gas system has been achieved for flows up to 2.5 l/min in each endcap while maintaining the system pressure to ± 0.02 Torr[11]. This corresponds to a complete volume change every 18 hours. In addition to controlling the duty cycle of the heaters and the freezer's compressor, the microprocessor is used to control an auxiliary bubbler connected to the condensing tank. This addition was found to be necessary to achieve long term stability for flows greater than 1 l/min in each endcap. It is postulated that the collection of nitrogen and other gases that slowly

---

[8] Model 221A: MKS Instruments Inc., Andover, MA 01810, USA.

[9] Silica Gel Sorbead WS: Costal Chemical, Pasadena, TX 77503, USA.

[10] Q5 Reactant: Engelhard Co., Elyria, OH 44035, USA.

[11] As C_4F_{10} is fairly dense ($\sim 1.59 g/cm^3$), there is a 2 torr pressure difference between the top and the bottom portion of the ECRID vessel.

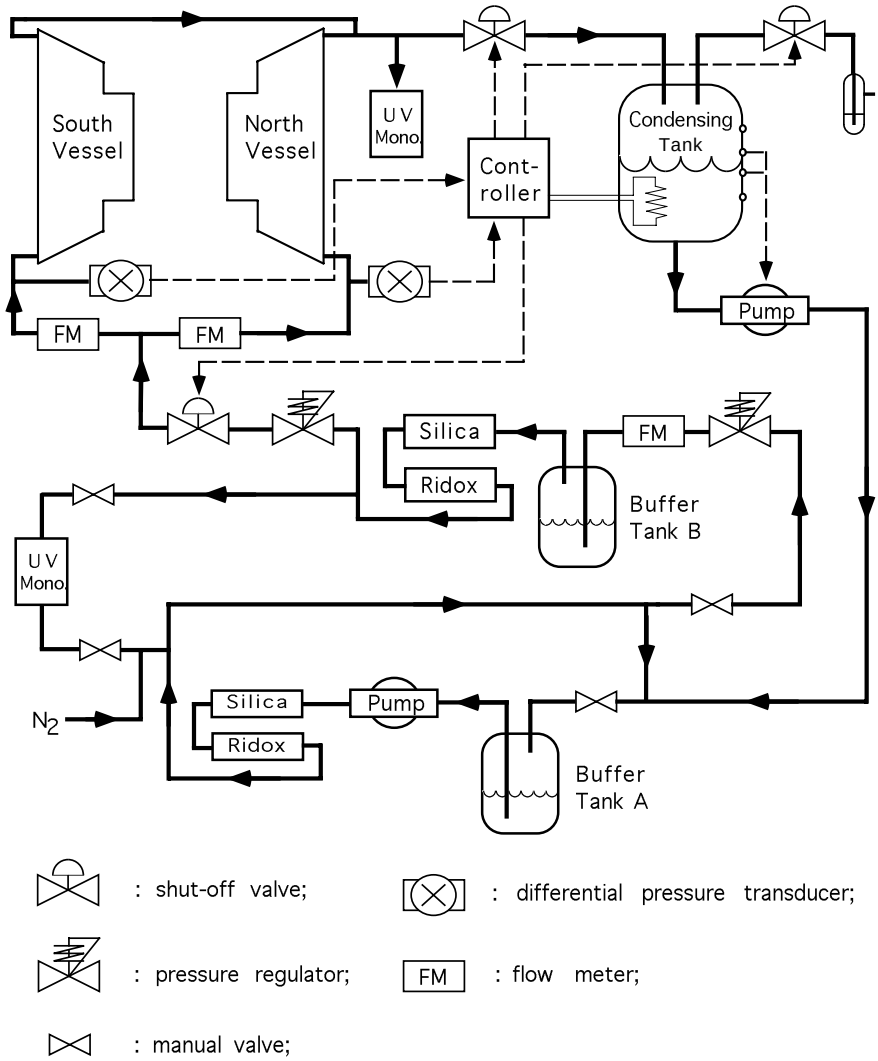

Figure 4.15: A schematic of the ECRID C_4F_{10} Recirculation and Pressure Control System.

leak into the system causes system instabilities. With the use of the bubbler, which is opened when the fraction of time that the heater is on falls below a setpoint, those gases which do not condense in the tank are purged before they accumulate to the point of causing serious system disruption.

All aspects of the CRID's hardware status, including the ECRIDs' vessel pressure, are continually monitored by a dedicated μVAX (Fig. 4.17). In addition, there are several layers of alarms to ensure that the hardware is performing within well-defined parameters. The C_4F_{10} transparency is measured using a UV-transmission apparatus similar in nature to the reflectometer used to test the mirrors. The system design allows

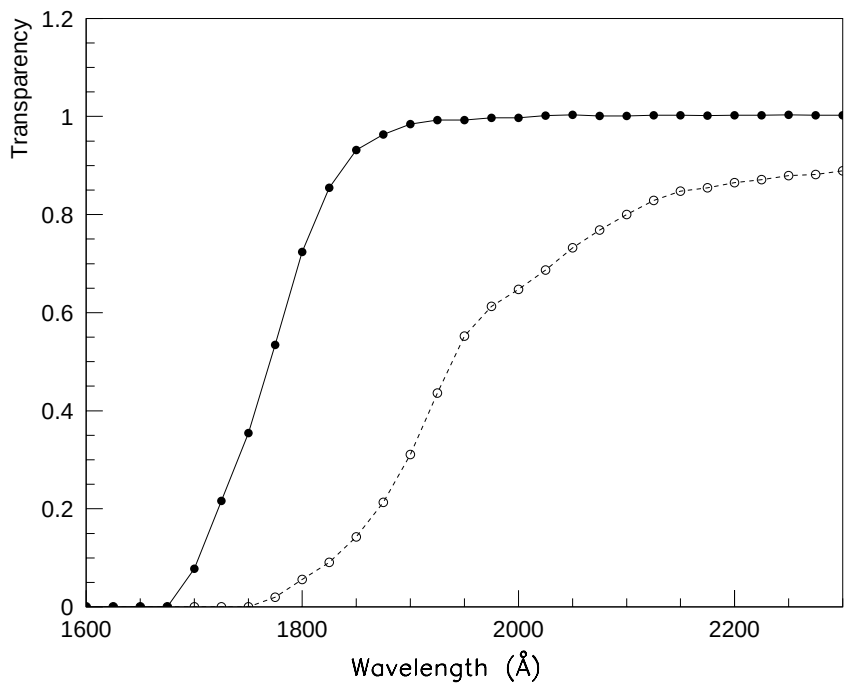

Figure 4.16: Transparency measurements in 1 cm of liquid C_4F_{10} held inside a cell equipped with quartz windows. The dashed lines show the unfiltered transparency, the solid lines show the improvement due to filtration. Note that the transparency of the quartz essentially "cuts off" at 1650Å.

for sampling at different stages of the recovery and filtering process. A sonar system inside the vessels monitors the gas composition at three different heights.

4.3 The ECRID in Operation

At this time, the ECRID has not been used in physics analysis, due to the fact that the offline software for the ECRID and the EndCap Drift Chambers (EDC) is still being developed. Nevertheless, we have several indications that the ECRID hardware and online software is fully functional.

All CRID Drift Boxes (Barrel and EndCap) are equipped with UV fiber optic flashers that are strategically placed just outside the quartz windows. These fibers, which are oriented toward the interior of the box, are designed to produce "survey points" that allow the drift fields, electron lifetime, etc. to be monitored during normal operation.

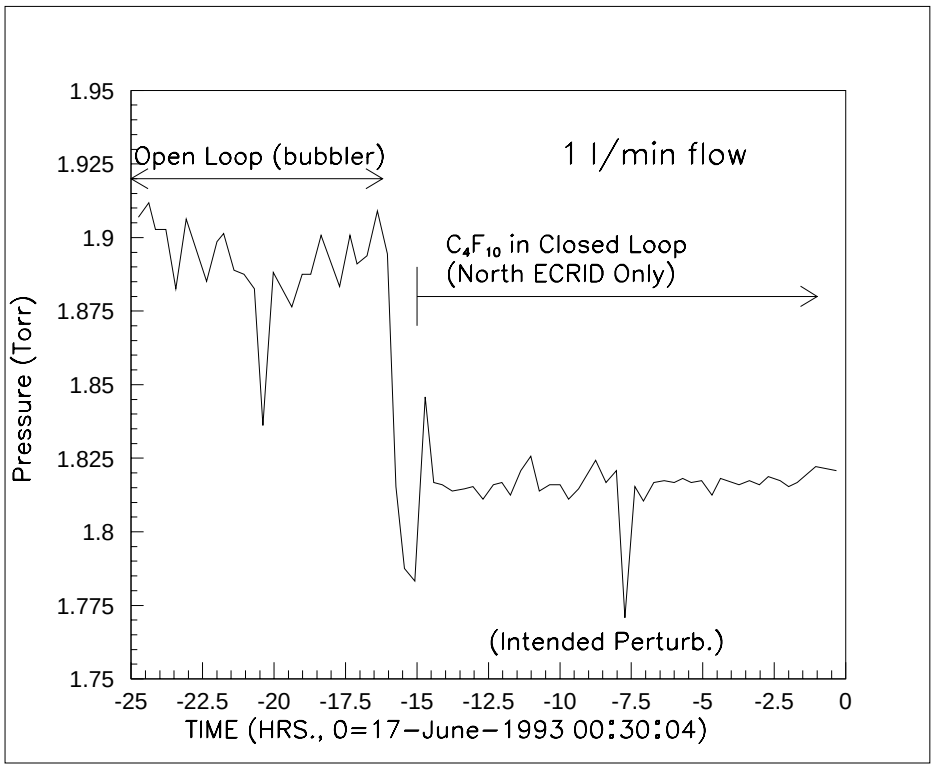

Figure 4.17: C_4F_{10} pressure control time history for the first vessel test. Note the reduction in the magnitude of the pressure oscillations once the system was run in closed-loop mode.

Figure 4.18 shows the orientation of the fibers on the quartz surface of the ECRID drift boxes.

The first data to be acquired from the ECRID drift boxes were of the reconstructed electrons produced by these UV flashers. Figures 4.19 and 4.20 show two views of the reconstructed electron patterns. Comparing these figures to the schematic, it is apparent that the drift boxes and detectors are performing as designed.

Due to the software problems discussed above, it is impossible at this time to perform particle identification. By looking at very high momentum tracks that are well separated from other tracks in the event, we see ring candidates of the appropriate (limiting) radius. Figure 4.21 is an overlay of many such ring candidates.

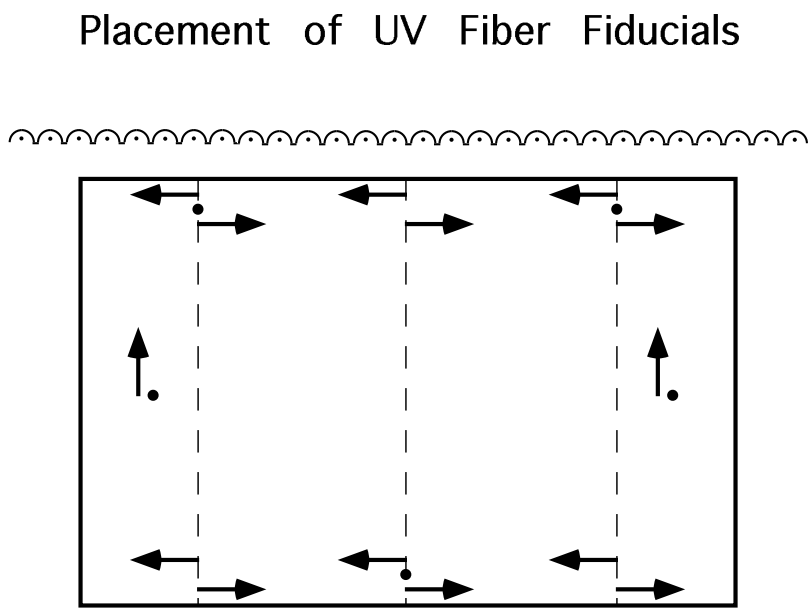

Figure 4.18: A schematic of the UV-fiber layout on the quartz window of an ECRID drift box. The scalloped-structure at the top of the drawing indicates the wire-detector plane; the wire number hit gives the "TPC X" coordinate. The $\vec{E}$ field points from top to bottom; the electrons drift along this axis. The amount of time between the beam crossing and the detection of the electron gives the drift distance - the "TPC z" coordinate. The third dimension, given by charge division, points into the page. The arrows indicate an angled orientation of the fibers with respect to the quartz face; the black circles indicate fibers that point directly into the drift box.

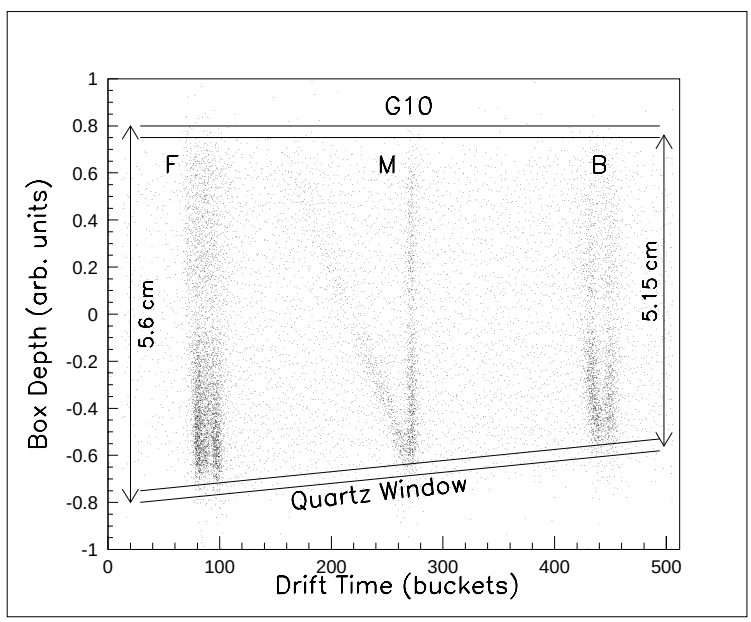

Figure 4.19: A "side-view" of the reconstructed hits produced by the UV fiber flashers. The horizontal axis is the drift time (z) coordinate, and the vertical axis is the charge division (y) coordinate.

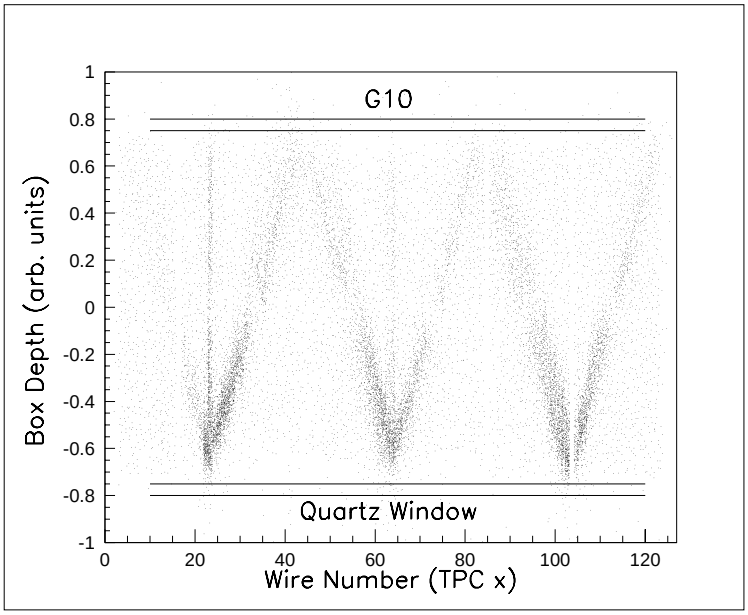

Figure 4.20: A "front-view" of the reconstructed hits produced by the UV fiber flashers. The horizontal axis is the wire address (x) coordinate, and the vertical direction is the charge division (y) coordinate.

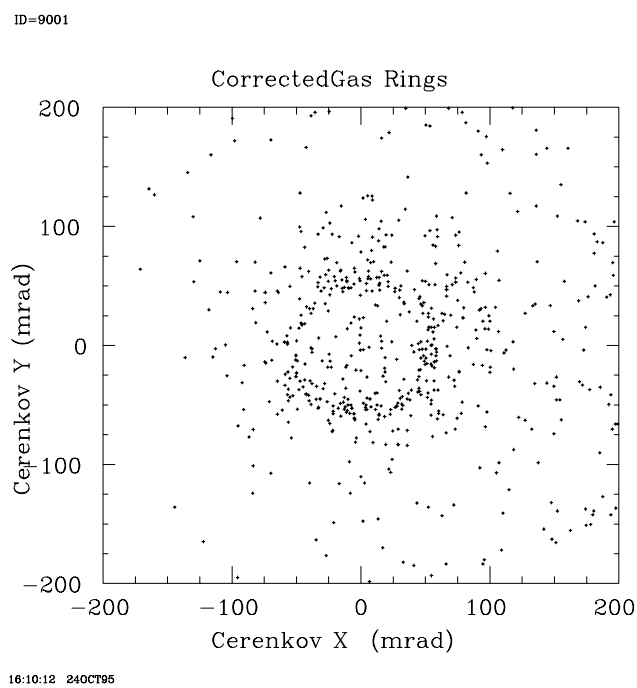

Figure 4.21: Overlay of reconstructed rings in the SLD EndCap CRID.

Chapter 5

Hadronic Event Selection

For this analysis, the strengths of SLC/SLD were used to separate the Z^0 decays into high purity light- and heavy-quark hadronic samples, and to separate the light quark jets into enriched quark and antiquark jet samples. In this chapter, the conditions necessary to record data are discussed. The criteria for selecting hadronic events are then described, including the important feature of determining the position of the interaction point. Next, the flavor-tagging technique using signed impact parameters is explained. Lastly, the procedure used to select enriched quark jets based upon the sign of the electron beam polarization is described.

5.1 The SLD Readout Triggers

One of the many advantageous features of working in an e^+e^- environment is the simplicity of the trigger system. Since the background does not often mimic the interesting physics (hadron production, τ pairs, μ pairs, or bhabhas–e^+e^- pairs), straight-forward "intuitive" triggering techniques are used to decide when to record the data to tape. Below are the seven triggers used in the 1993-95 running periods. With the exception of the Bhabha triggers, all components of the detector are read out on every trigger.

1. The Energy Trigger: This trigger is designed to "fire" on events with a large amount of energy in the LAC, and requires that at least 8 GeV total deposited energy (min-I scale)[1] be recorded for the EM and/or HAD calorimeter towers in the LAC. Only the energy in towers that are above a certain (noise) threshold are

[1] The standard LAC energy scale used is the *min-I* scale, referring to minimum ionizing particles such as muons. In this scale, ADC counts are converted to energy as follows: For the EM towers, 1 ADC count = 2.04 MeV; For the HAD towers, 1 ADC count = 5.41 MeV.

recorded; the thresholds are defined to be 60 ADC counts for the EM towers (corresponding to 246 MeV) and 120 ADC counts for the HAD towers (corresponding to 1.296 GeV). Prior to October 1994, when this trigger was fired the calorimeter systems (LAC,WIC,LUM) were the only detector elements read out. Since then, the entire detector is read out for each Energy trigger.

2. The Tracking Trigger: This requires that at least two charged tracks pass through 9 of the 10 CDC layers and be separated from each other by at least 120°. The cells are marked as "hit" if 6 of the 8 sense wires have pulses above threshold. The pattern of the hit cells is required to match an entry in a pattern map for the CDC. Entries in this map correspond to all possible trajectories for $p_T > 250\ MeV/c$ charged tracks originating from the Interaction Point (IP). This trigger is very efficient for hadrons and τ decays in the barrel region.

3. The HAD Trigger: This is a combination of the first two triggers, requiring both one charged track passing through 9 of the 10 CDC layers and a smaller deposition of energy in the LAC than the Energy Trigger.

4. The WAB Trigger: This trigger is designed to be fired by two back-to-back charged tracks in the CDC. Unlike the above tracking trigger, this trigger allows short track stubs to satisfy the criterion. It is designed to catch all wide angle Bhabha ($e^+e^- \rightarrow e^+e^-$) "WAB" events, even when the CDC detector acceptance limits the length of the track being measured.

5. The Muon-pair Trigger: This requires one charged track in the event to satisfy the 9 layer CDC requirement. Calorimetric hits must be present in the opposite WIC octant.

6. The Bhabha Trigger: This trigger requires a total energy (EM scale) of at least 12.5 GeV in both the North and South EM2 (the outer of the two EM layers) sections of the LUM. This threshold ensures that the trigger is not fired due to background splashes on the luminosity monitor. For this trigger, only the LUM/MASiC is read out.

7. The Random Trigger: This trigger recorded data every 20 seconds, regardless of the detector status, to provide information for background studies.

At SLD, the efficiency for triggering on hadronic Z^0 decays approaches 100% [48]. During good running conditions the typical trigger rate is $\sim 0.1Hz$, while during "noisy" running it can easily reach above $2Hz$.

5.1.1 The Tracking Trigger Veto

Several vetos have been built in to the triggering system in order to prevent excessive detector dead-time due to the processing of "noisy" events. These events are most often caused by the detector being sprayed by the accelerator during moments of non-optimum running. One of these vetos, the Tracking Trigger veto, prevents the tracking information from being read out if more than 275 of the 640 CDC cells are marked as "hit"; where a "hit" means that 6 of the 8 sense wires have a signal pulse. During nominal running, this has a relatively small effect on the number of Z^0's that are recorded without tracking information. However, for a substantial portion of the 1993 physics run ($\sim$ 40%), the Tracking Trigger Veto was set incorrectly, causing a bias against high multiplicity events ($\sim$ 5% of the 1993 hadronic events). This effect has been modelled in the Monte Carlo simulation (discussed below).

5.2 The Hadronic Event Filter

After the data has been written to tape, several filtering routine are used to select potential Z^0 candidates and reject a large fraction of the background. This filtering is performed using information form the LAC, WIC, and CDC (at the track pattern level). For selection of hadronic events, a logical OR of two filters is taken. The first filter, the "EIT filter", uses the LAC information to select events that have energy above a certain threshold and good forward-backward energy balance. The second "Track" filter requires at least one track (at pattern recognition level) to be above 1 GeV/c in momentum.

For this analysis, we use the EIT (Pass 1) filter. The LAC quantities used for EIT-Pass 1 are:

- NEMHI : The number of LAC EM towers with a signal above the "Hi" Threshold of 60 ADC counts.
- EHI : The sum of the energy deposited in all of the LAC EM(HAD) towers with a signal greater than the "Hi" threshold: 60(120) ADC counts.
- ELO : The sum of the energy deposited in all of the LAC EM(HAD) towers with a signal greater than the "Low" threshold: 8(12) ADC counts (equivalent to 33 MeV (130 GeV) on the min-I scale).

The EIT Pass-1 filter requires that each event satisfies:

1. $NEMHI \geq 10$
2. $EHI > 15$ GeV (min-I scale)
3. $ELO < 140$ GeV (min-I scale)
4. $2 * EHI > 3 * (ELO - 70GeV)$
5. The N and S hemispheres must each have $NEMHI > 0$

Requirements 3 and 5 remove beam-wall and other accelerator-based background events. Item 4 removes events with large numbers of SLC muons passing through the LAC. It is estimated that $\sim$ 97% of the background events that pass one or more of the triggers are rejected by the Pass 1 filter. The combined efficiency for a hadronic Z^0 decay to pass both the triggering algorithm and the EIT Pass-1 filter is approximately 92% [48]. Events that survive the Pass-1 filter then are run through a Pass-2 filter that classifies an event as a potential WAB, μ-pair, or hadron event. Figure 5.1 shows several event-variable comparisons between the data and the Hadronic MC with detector simulation.

After events are filtered, a full detector reconstruction procedure is performed to make a "physics-ready" data summary tape (DST). Analysis is then performed using either the full DST or compressed versions of it (miniDSTs, micro-,nano-,etc.).

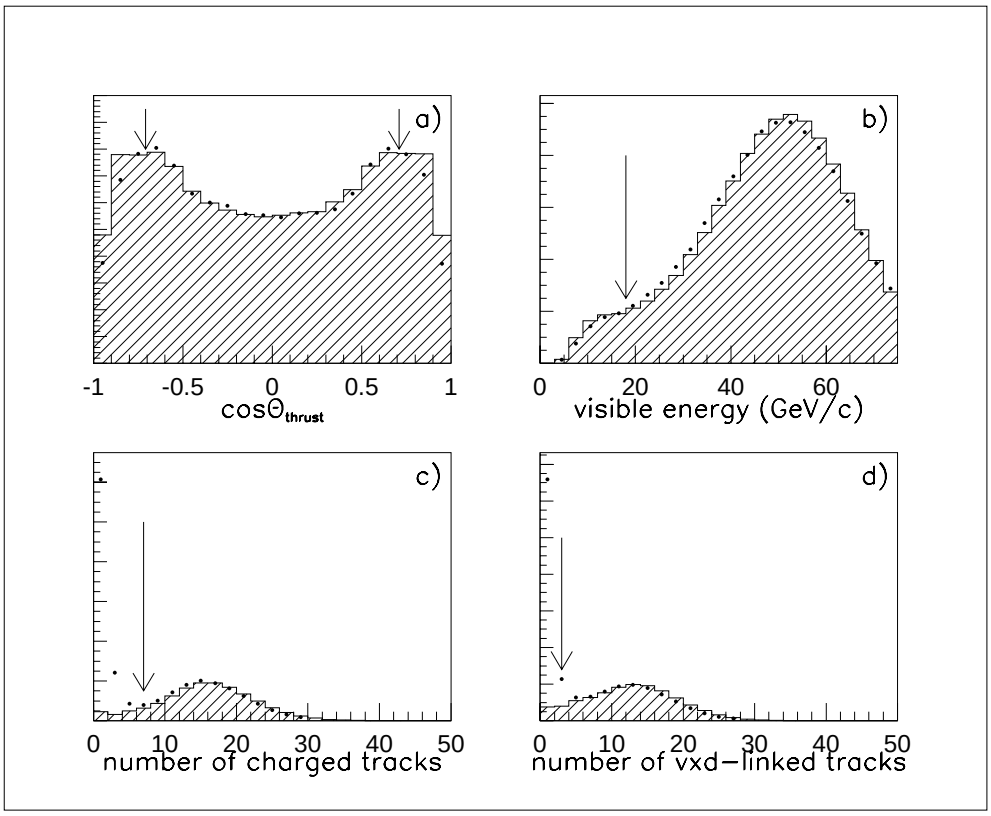

Figure 5.1: Data (points) and MC (hatched) comparisons for events that pass the EIT hadronic filter. The arrows indicate the cut values used in the final event selection. The excess of events with low charged track multiplicities is due to the $Z^0 \rightarrow \tau^+\tau^-$ contamination in the EIT-filtered event sample.

5.3 Hadronic Event Selection

For this analysis, a hadronic event is defined as an event which satisfies the following criteria:

1. The event passes the EIT filter described above.
2. The *Thrust* axis of the event (defined below) must satisfy $|\cos\theta_{thrust}| \leq 0.71$, where θ_{thrust} is the angle of the thrust axis with respect to positron-beam direction. The thrust axis is calculated using the LAC energy clusters.
3. The event contains at least 7 charged tracks in the event, each with $p_T \geq 200\ MeV/c$.
4. At least 3 of the charged tracks must have 2 or more VXD hits.
5. The visible energy of the charged tracks must be at least 18 GeV.
6. The Interaction Point (IP) of the event must be well measured.

The Thrust axis of the event is defined as the axis $\hat{t}$ which maximizes the quantity

$$T = \frac{\sum_{clusters} |\vec{p} \cdot \hat{t}|}{\sum_{clusters} |\vec{p}|}, \tag{5.1}$$

where $\vec{p}$ is the 3-momentum of the energy cluster, assuming the IP as the origin of the vector and the pion mass for the particle that generated the energy splash. The requirement that the thrust axis satisfy $|\cos\theta_{thrust}| \leq 0.71$ guarantees that the event is contained in the barrel portion of the detector.

The IP position is required to be well measured so that the techniques described below may be used to "tag" the event as a probable light-flavor event ($Z^0 \rightarrow q\bar{q}$, where q=u, d, or s) or a probable heavy-flavor event ($Z^0 \rightarrow Q\bar{Q}$, where Q=c or b).

Figure 5.2 shows a comparison between the data and the MC simulation (discussed below) for several event variables; they are in good agreement with one another. Agreement between the data and the MC is important in order to have confidence in the simulation values for reconstruction efficiency, etc. The number of selected hadronic events for the various data-collecting periods in the 1993 and 1994-95 physics runs are shown in Table 5.1.

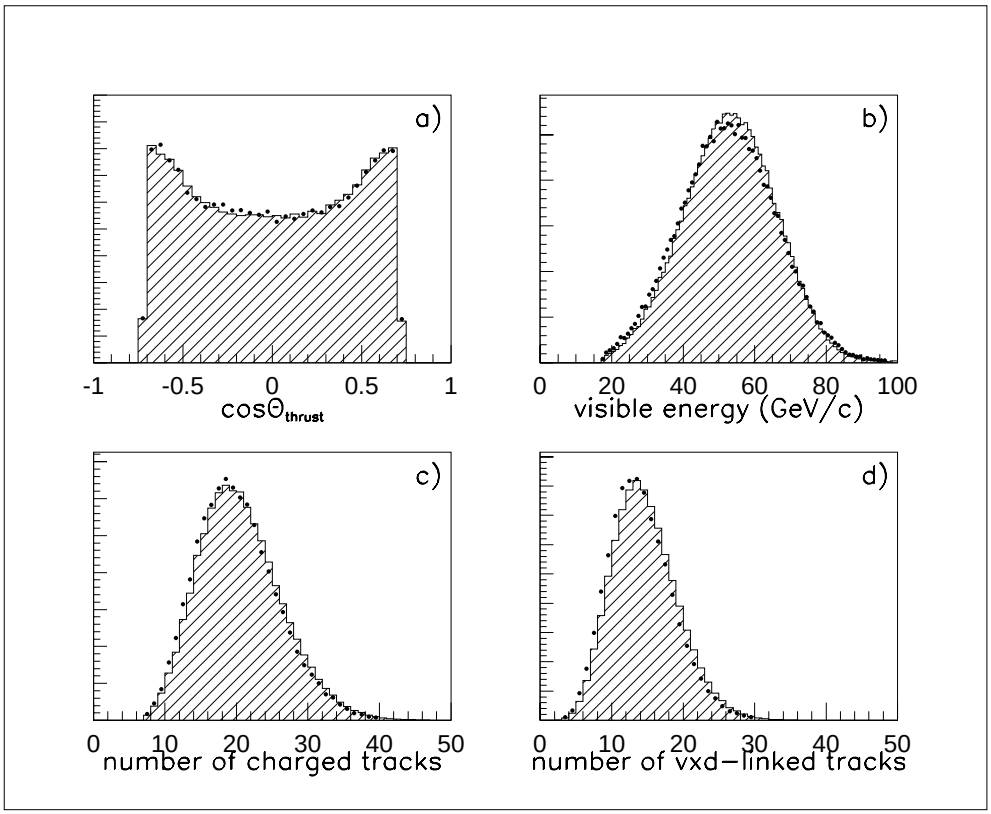

Figure 5.2: Data (points) and MC (hatched) comparisons for selected events. It is estimated that there is less than 0.2% τ contamination in the final hadronic event sample.

Run Period	# of Selected Hadronic Events
1993 Pre-Veto	8552
1993 Veto	11702
1993 Post-Veto	8035
1994 Summer	12133
1994 Fall	29702
1995	20125
total:	90249

Table 5.1: Selected Hadronic Z^0 statistics for the 1993-1995 data run.

5.3.1 Precision IP Position Determination

For each hadronic interaction, an average primary vertex position in the transverse plane (the plane perpendicular to the beam) can be determined by extrapolating all charged tracks back toward the center of the SLD beam pipe, and fitting for a common vertex. This gives a transverse error ellipse of typically 100 μm along the major axis and $\sim$ 15 μm along the minor axis (see Figure 5.3). As the SLC interaction region is very small ($\sim$ 1-3 μm in the transverse plane, and $\sim$ 0.7 mm in length) and fairly steady, a much better determination of the transverse IP position can be obtained by averaging over a block of sequential events. By performing this averaging, the error ellipse becomes essentially circular by removing the jet-axis bias. Also, averaging removes the biases due to isolated tracks and displaced secondary vertices.

The SLD hadronic data set is broken into blocks of 30 sequential Z^0 decays (an exception is made when at least 20 events are acquired and an interruption in SLC collisions occurs). The average primary vertex for each event is obtained, and an average IP position for the block is calculated. An iterative chi-squared fit is then performed to obtain the best IP position for the block of events; typically the procedure converges after 5 iterations, at which point the overall fit has a $\chi^2/dof < 1.3$. This produces an average IP position with a transverse resolution of $\sim$ 7 μm.

This technique has been cross-checked using a data sample independent of the hadronic data set: the $Z^0 \rightarrow \mu^+\mu^-$ events (Fig. 5.4). By extrapolating both of the muon tracks back to the IP and then subtracting out the extrapolation errors,

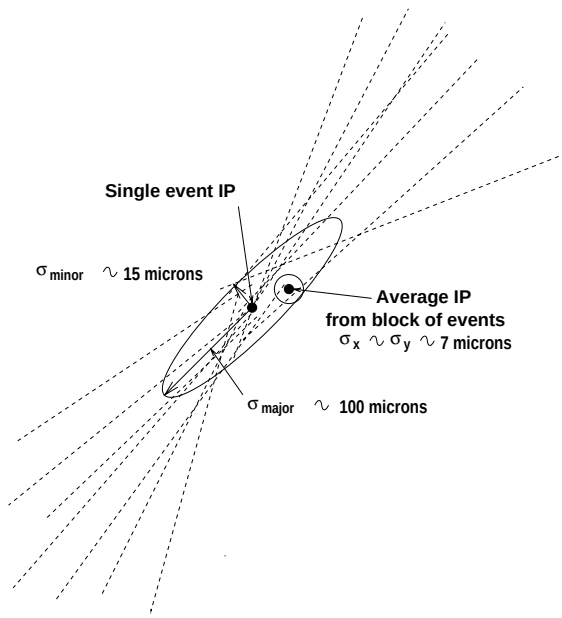

Figure 5.3: The differences in the transverse IP position and errors determined from a single event and the average over a block of events. Note that the jet bias in the error ellipse is essentially removed by averaging over many events.

the resulting width of the distribution is $7 \pm 2\mu$m, which is consistent with the above resolution.

The longitudinal position of the IP is determined on an event-by-event basis, as the tracking resolution is much finer than the possible distribution of the interactions along the z axis (i.e. the bunch length, which is ~ 1 mm). After the average transverse position of the the IP for a given data block is determined by the above technique, tracks with associated VXD hits in a given event are extrapolated to their point of closest approach in the x-y plane to the average IP position. The z position of this point is computed and, if the x-y impact parameter is less than 3σ and 500 μm from the average (transverse) IP position, it is used to compute the median z position of the event. The resolution of the median z position has been found to be flavor dependent [11]; the typical resolution for locating the IP z position has been determined (via Monte Carlo + detector simulation) to be (32,36,52) μm for (uds,c,b) events.

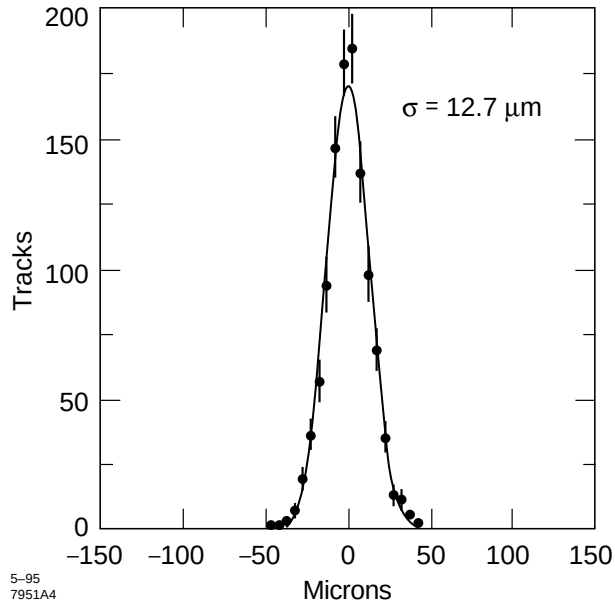

Figure 5.4: The xy impact parameters of tracks in $\mu^+\mu^-$ events. After correcting for extrapolation errors, a resolution of $\sim$ 7 μm on the transverse position of the IP is obtained.

5.4 Hadronic Event and Detector Simulation

The development of selection cuts used in this analysis and the estimation of selection efficiencies and sample purities required a detailed simulation of the detector and physics processes. A Monte Carlo (MC) "generator" was used to generate hadronic events. The output of the generator was then passed through a simulation package (GEANT 3.21 [49]) designed to simulate the detector response. The data obtained from the random triggers were "overlaid" to simulate the presence of backgrounds. The simulated event was then reconstructed in the same manner as the data.

For the 1994-95 MC, the JETSET 7.4 [31] generator was used with LUND fragmentation parameters determined using TASSO [50] and OPAL data [51], and particle production parameters tuned to reproduce data from other experiments at Z^0 energies [52] (for the 1993 MC the JETSET 6.3 generator was used with similar tuning). The fragmentation function for the b- and c- quarks followed the Peterson representation [53]. A B-hadron decay model was developed at SLD and tuned to CLEO and ARGUS data; a detailed description of this model is found in [54]. The combination of this output with the detector simulation is referred to herein simply as "the MC".

We also use the generator level output (without detector simulation) for comparisons with our experimental results. In addition to the above generator, which we refer to as "SLD-Tuned JETSET", we also make comparisons with "Default JETSET" – JETSET 7.4 without special parameter tuning or special b-decay model.

5.5 Flavor Tagging, and Quark-Jet Tagging

For the first portion of this analysis, the determination of production rates and spectra of K_s^0 and $\Lambda^0/\bar{\Lambda}^0$ in hadronic decays, it is sufficient to select a hadronic event sample. We are able to capitalize on the operating conditions at SLD in order to study more deeply the hadronization phenomenon. Below we discuss two "tagging techniques" used to produce high-purity subsets of the data.

5.5.1 The Normalized Impact Parameter and Flavor Tagging

Once the hadronic event has been selected, the impact parameters of charged tracks are used to tag the flavor of the event. This tag technique, originally proposed by Hayes [55], exploits the facts that heavy quarks from Z^0 decays hadronize into fast heavy hadrons, which then travel a measurable distance (typically 3 mm for B hadrons and 1.5 mm for charmed hadrons) before decaying into a large number of charged tracks. As these heavy hadrons have a high mass, the impact parameters of the decay particles with respect to the IP are large in comparison to the detector resolution. In contrast, light quarks (u,d,and s) typically produce very few tracks with significant impact parameters. A schematic of a B meson decay is shown in Figure 5.5.

An improvement of this technique was suggested [56, 57] to sign the impact parameter of the track based upon where the charged track crosses the jet axis. As shown in Figure 5.6, tracks crossing the jet axis in front of the IP get a positive sign, while those crossing behind get a negative sign. This creates an asymmetric distribution as the tracks from heavy meson decays tend to populate the positive region (Fig. 5.7).

For this analysis, we use a 2-D signed impact parameter technique to select flavor-tagged events. In order to be less sensitive to track reconstruction errors, material

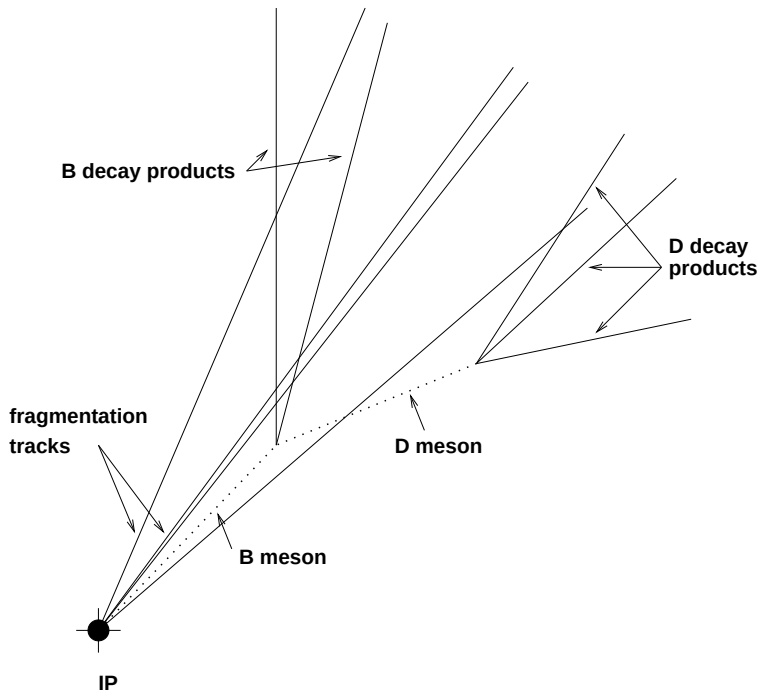

Figure 5.5: An example of a B meson decay. The fragmentation tracks tend to point back toward the IP, while the tracks from the neutral heavy meson decays may or may not.

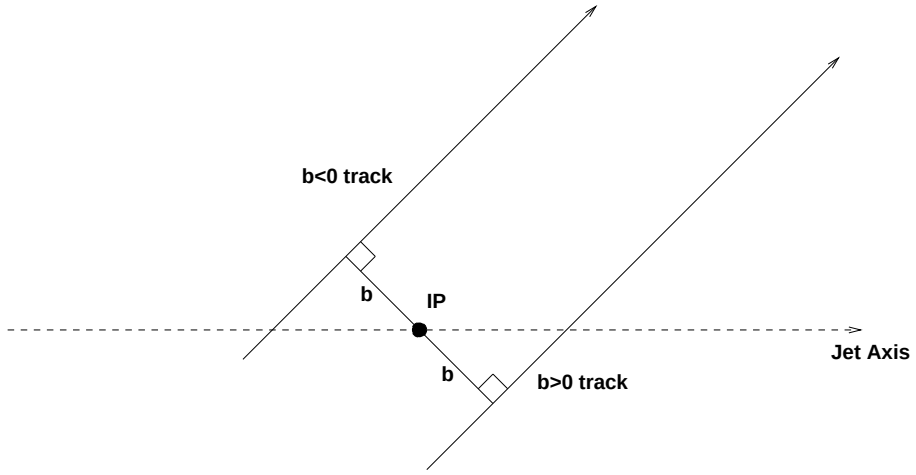

Figure 5.6: The sign convention for the signed impact parameter technique. The jet axis is used as an approximation of the heavy-quark hadron flight direction.

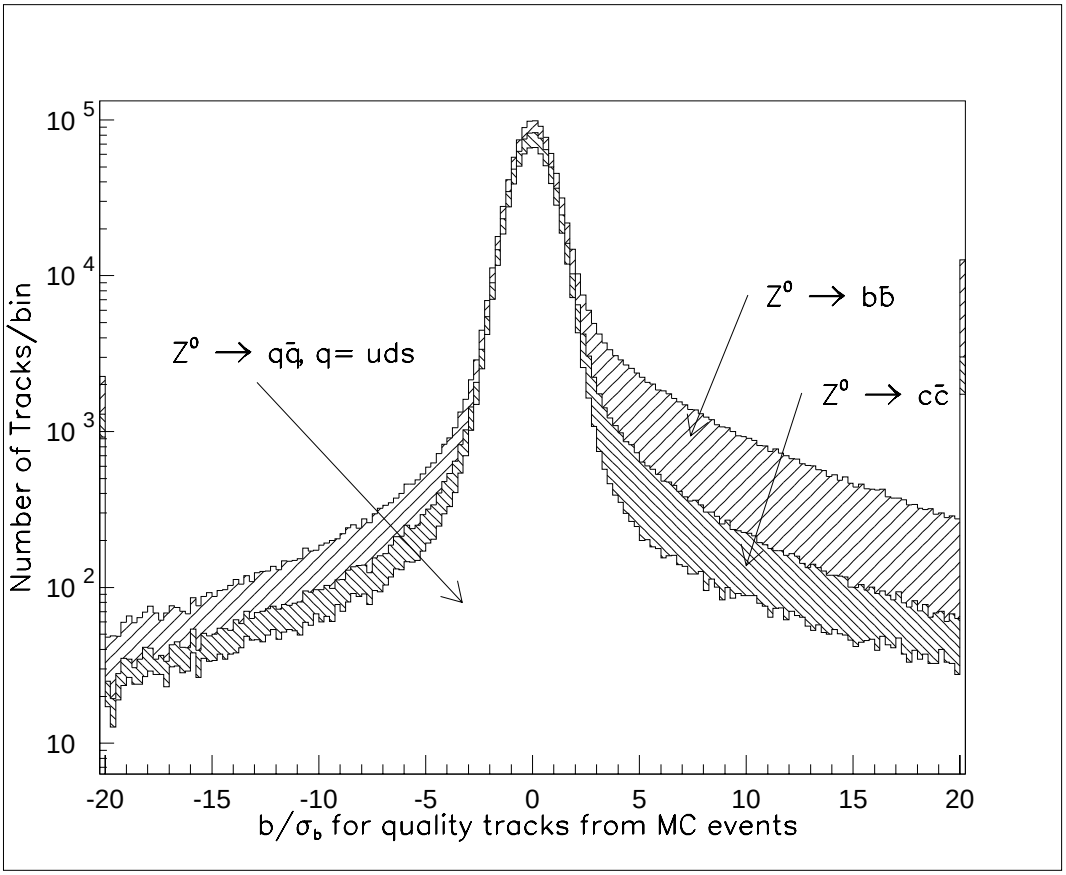

Figure 5.7: The normalized impact parameter (b/σ_b) distribution for light and heavy quark decay modes. The first and last bins show the amount of under- and over-flows.

interactions, neutral particle decays, and uncertainty of heavy-hadron lifetimes, the selection cuts are applied to a well-measured (and well-simulated) subset of the charged tracks. These tracks, herein referred to as *quality* tracks, have met the following requirements:

- The first hit for the CDC-portion of the track must occur no further than 39 cm (radially) from the origin. This requirement limits the extrapolation distance back to the VXD.
- There must be at least 40 CDC hits associated with the charged track.
- The track must extrapolate back to within 1 cm radially of the IP, and within 1.5 cm in the z direction. This is required in order to reject most tracks that potentially are due to nuclear interactions with the detector or beam pipe material.
- The quality of the CDC track fit must satisfy $\chi^2/dof < 5$.
- Pairs of oppositely-charged tracks were combined through a V^0 finding algorithm (which served as the basis for the analysis discussed in the next chapter). Tracks which formed a V^0 that was consistent in mass with either a K_s^0 , a Λ^0, or a γ-conversion were rejected.
- Tracks must have at least one associated VXD hit.

After combining the required VXD information with the CDC track that passes the above requirements, additional constraints were applied:

- The 2-D (xy) impact parameter, b, of the track to the IP must be less than 3 mm.
- The uncertainty on the impact parameter, σ_b, must be less than 250 μm. Effectively, this sets a minimum track momentum of $\sim$ 300 MeV/c.
- The quality of the CDC+VXD track fit must satisfy $\chi^2/dof < 5$.

After applying these selection criteria, a difference in the average number of quality tracks for the MC and the data was observed: 12.81 quality tracks/event for the MC

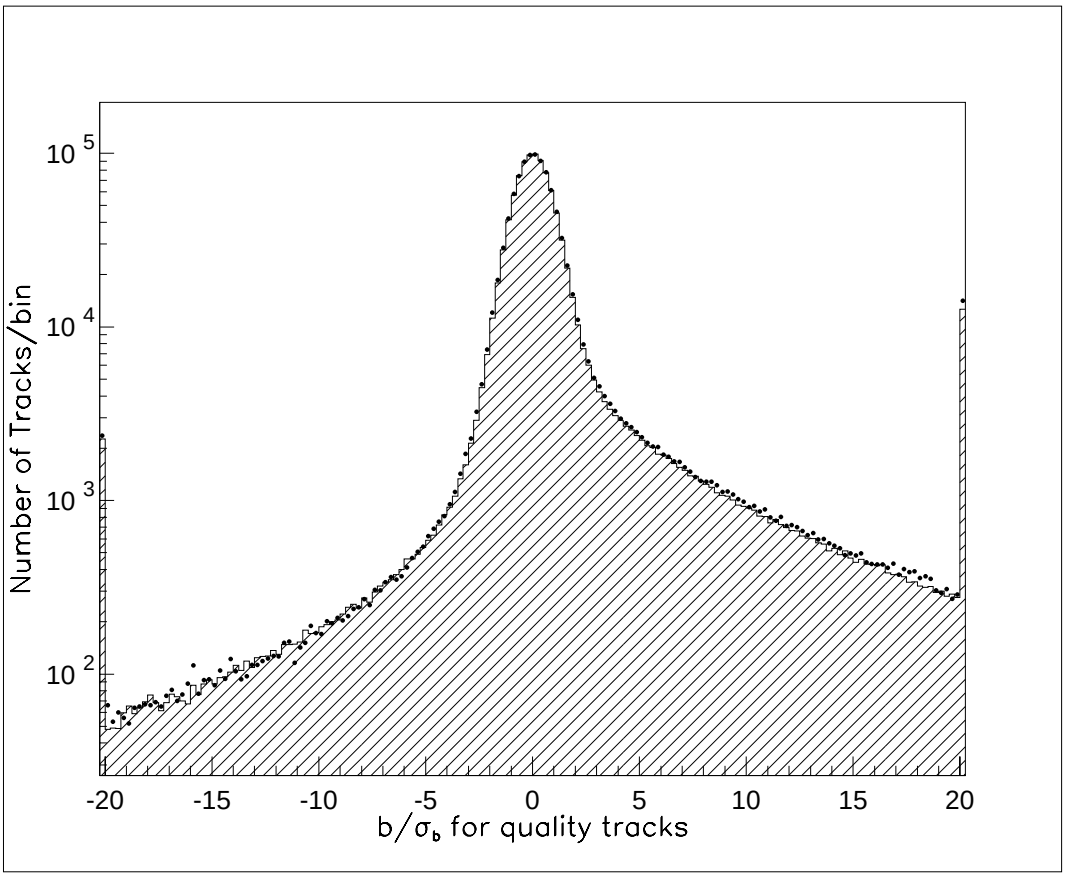

Figure 5.8: A comparison of the normalized impact parameter distributions for data (points) and MC (hatched). The first and last bins show the under- and over-flow number of tracks. A *significant* track is defined as a track whose $b/\sigma_b > 3.0$.

simulation; 12.24/event for the data. Angular-dependent and momentum-dependent efficiency corrections were applied to the MC in order to provide good agreement between the data and the MC [58]. A comparison of the normalized impact-parameter distributions for the data and the MC (after corrections) are shown in Figure 5.8.

For this analysis, we define a *significant* quality track as one whose normalized impact parameter is greater than 3.0. Figure 5.9 shows the comparison between the MC and the data for the number of significant tracks per event, n_{sig}; very good agreement is observed. The events with large numbers of significant tracks are predominantly b-quark events, while those with few significant tracks are predominantly *uds* events. Therefore, the hadronic event sample is broken into three subsamples as follows:

- a "*uds*-enriched" sample of events with no significant quality tracks , i.e. events

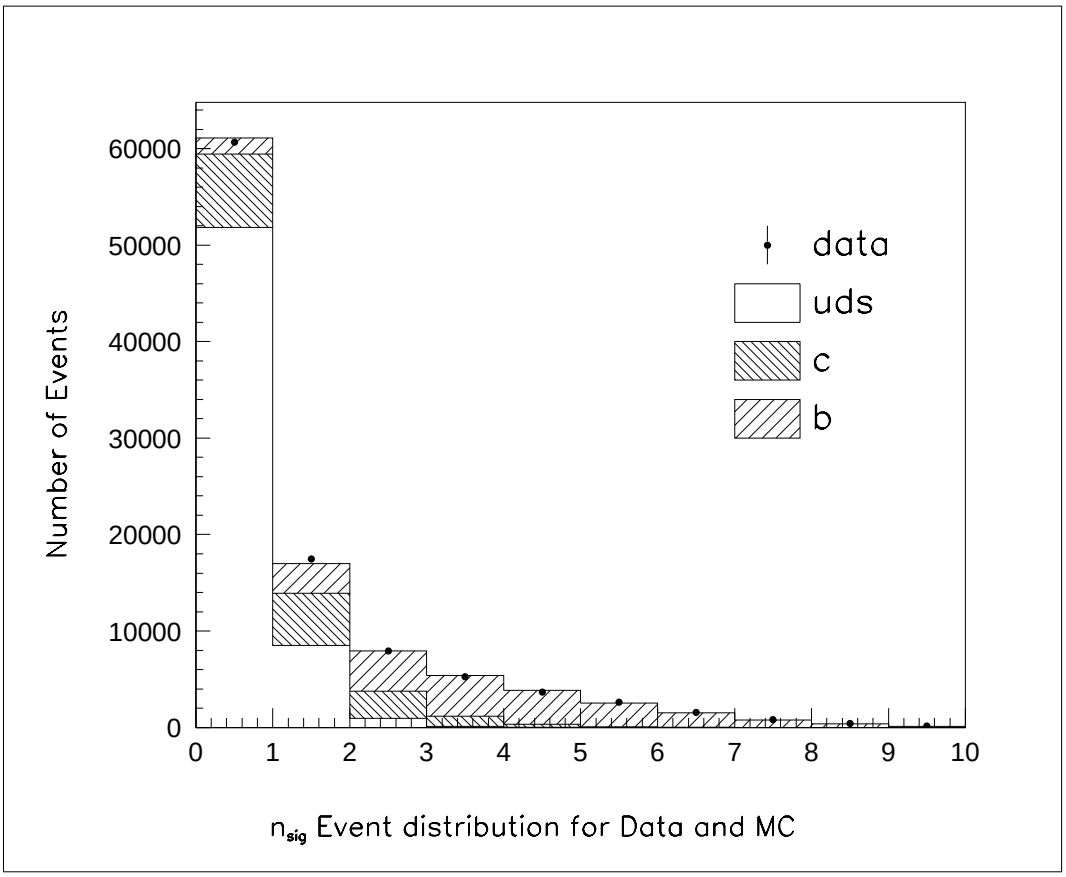

Figure 5.9: A comparison of the n_{sig} distributions for the data (points) and the MC (histogram). Events with 3 or more significant tracks are tagged as b-quark events; events with 0 significant tracks are tagged as *uds* quark events, and the remaining events are tagged as c-quark events.

with $n_{sig} = 0$,

- a "c-enriched" sample of events with n_{sig} =1 or 2,
- a "b-enriched" sample of events with $n_{sig} \geq 3$.

The nominal efficiency and purities for the event tags are shown in Tables 5.2 and 5.3. For the 1993-1995 data sets, there were 53526 $n_{sig} = 0$ events, 22648 n_{sig} =1 or 2 events, and 14039 $n_{sig} = \geq 3$ events.

5.5.2 Quark Jet Tagging

As was discussed in Chapter 2, the electron beam polarization at SLC induces a large asymmetry in the polar angle distributions of the quarks from Z^0 decays, which prefer to

n_{sig} tag	*uds* frac.	*c* frac.	*b* frac.
0	0.848	0.125	0.027
1 or 2	0.379	0.330	0.292
≥ 3	0.009	0.101	0.890

Table 5.2: Estimated event purities for the event flavor tags. The sum of each row equals 1.

n_{sig} tag	uds tag eff.	c tag eff.	b tag eff.
0	0.844	0.440	0.076
1 or 2	0.154	0.475	0.332
≥ 3	0.002	0.085	0.592

Table 5.3: Estimated tagging efficiencies for selecting $uds-$,$c-$, and $b-$quark events using the n_{sig} tag. The sum of each column equals 1.

follow the electron (positron) direction for left(right)-handed electron beams. Figure 2.3 shows the calculated quark production asymmetry for the average polarization obtained during the 1993 and 1994-95 physics run, $72.3 \pm 0.4\%$[2]. This unique feature of SLD was used to study particle production differences in (light) quark and antiquark jets.

In order to tag a hemisphere as a "quark-jet" hemisphere, the following procedure was used. For each *uds*-tagged event, the thrust axis was calculated as described above, and then signed so that the z-component pointed in the electron(positron) beam direction if the electron beam polarization was left(right)-handed. A plane perpendicular to the thrust axis was used to divide the event into two hemispheres, and the hemisphere whose tracks satisfied $\vec{p} \cdot \vec{t} > 0$ was tagged as the "quark-jet" hemisphere. The opposite hemisphere was tagged as the "antiquark-jet" hemisphere.

In order to improve the "signal-to-noise" ratio, events with $|\cos\theta_{thrust}| < 0.2$ were rejected. The purities for this tag as a function of the $|\cos\theta_{thrust}|$ cut are shown in Figure 5.10; the degradation in the purity of the tag at detector level is due to the acceptance cuts and the approximation of the thrust axis for the final state quark direction. To determine the best $\cos\theta_{thrust}$ value to cut at, the "quality" of the tag

[2]For this analysis, unlike that in reference [9], the average electron-beam polarization was $61.8 \pm .40\%$ for the 1993 physics run, and $77.2 \pm .24\%$ for the 1994-95 physics run

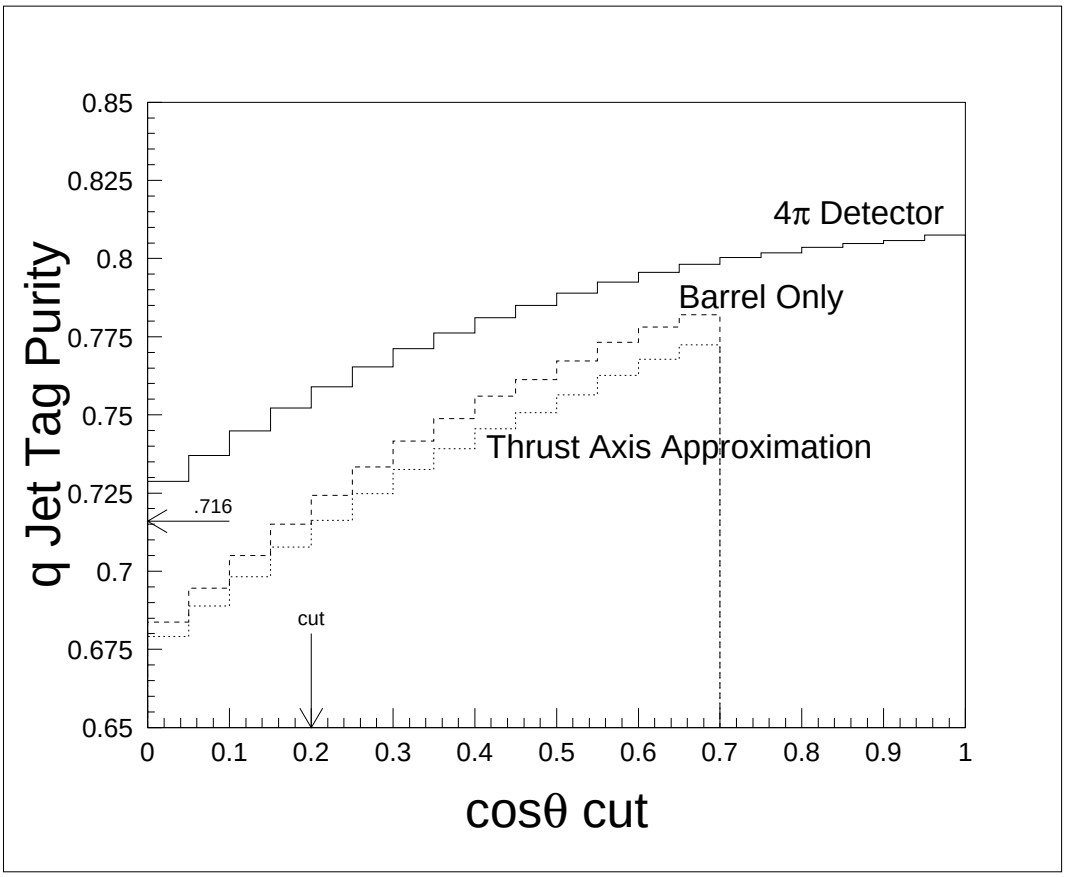

Figure 5.10: The calculated quark-jet tag purities as a function of the polar angle cut, assuming an average electron beam polarization of 72.3%. Shown are the tag purities for a perfect 4π detector, after acceptance cuts, and after using the thrust axis for the tag. For the $|cos\theta_{thrust}|$ chosen, an estimated quark jet purity of 71.6% is obtained.

was considered. This figure of merit, equal to $(N_{correct\,tag} - N_{incorrect\,tag})/\sqrt{(total)}$, was used to maximize the purity while minimizing the statistical error. The tag quality as a function of the polar angle cut is shown in Figure 5.11.

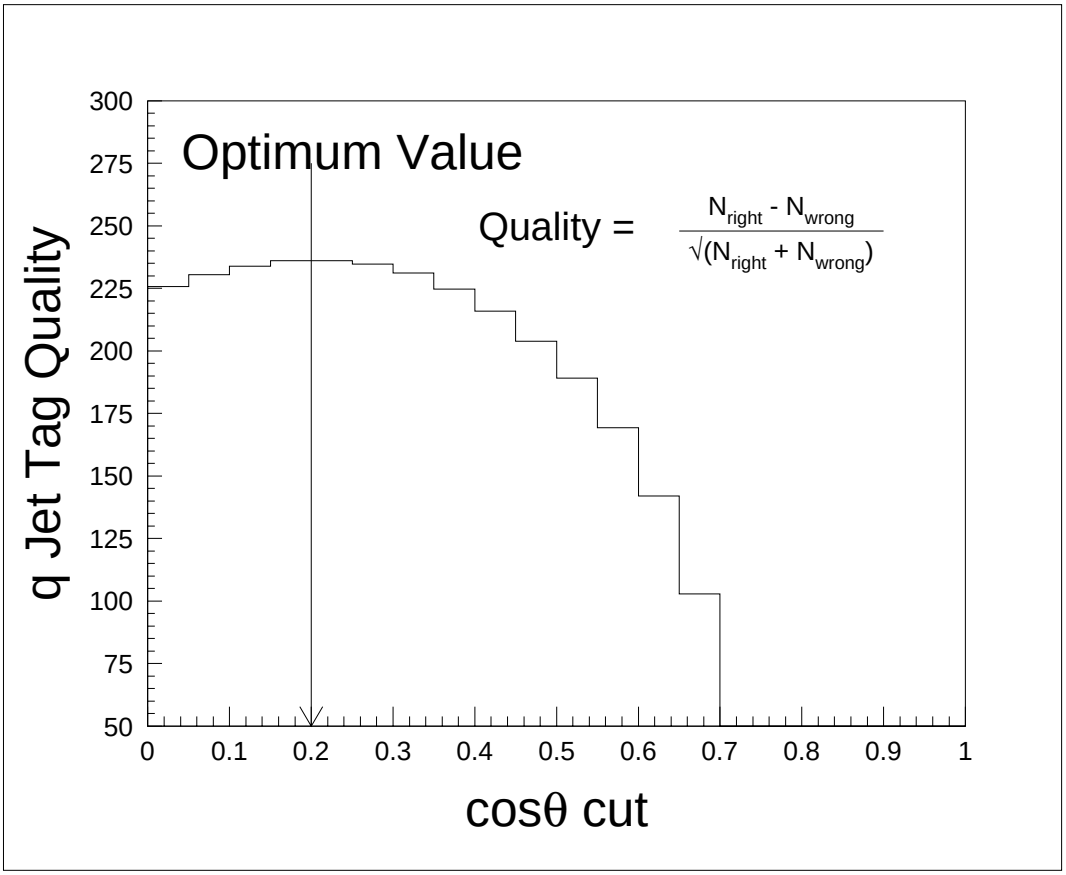

Figure 5.11: The "quality" of the quark-jet tag as a function of the Thrust Axis polar angle cut.

Chapter 6

The V^0 Reconstruction and the Global Analysis

6.1 Introduction

For this analysis we reconstruct the charged decay modes $K_s^0 \to \pi^+\pi^-$ and $\Lambda^0(\bar{\Lambda^0}) \to p(\bar{p})\pi^\mp$ (collectively referred to as V^0 decays). As the average charged particle multiplicity in Z^0 decays is approximately 20 tracks, a large combinatoric background exists. Selection cuts are used to improve the signal-to-noise ratio and to remove signal-distorting backgrounds. The data are binned in momentum and the V^0 invariant mass peaks are fitted. The resulting spectra are corrected for reconstruction and selection efficiency and integrated to obtain the total production rates. The spectra are compared to existing measurements and to QCD (MLLA+LPHD) predictions. Systematic errors and checks are discussed, including a cross-check against the well-measured K_s^0 and $\Lambda^0/\bar{\Lambda}^0$ lifetimes.

6.2 The Selection of the V^0 candidates

The tracks used to form the K_s^0 and $\Lambda^0/\bar{\Lambda}^0$ candidates were required to pass the following track quality cuts in order to improve the invariant mass resolution:

- a minimum transverse momentum of 150 MeV/c with respect to the beam direction.
- at least 40 hits measured by the Central Drift Chamber.
- a polar angle satisfying $|cos\theta| < 0.8$.

Pairs of oppositely charged tracks satisfying these requirements were then combined to form V^0 candidates if their separation was less than 15 mm at their point of closest

approach. A χ^2 fit of the two tracks to a common vertex was performed. To reject combinatoric background, the following selection cuts were applied:

1. The fit probability of the two tracks to a common vertex had to be greater than 2%.

2. This secondary vertex had to be separated from the IP by at least 1 mm, and by at least $5\sigma_l$. Here, σ_l is the error in the separation length of the V^0, using the assumed flight direction, the reconstruction errors for the secondary vertex, and the uncertainty in the IP position. The nominal errors used for the IP position were 7 μm in the plane perpendicular to the beam, and 35 μm in the electron-beam direction.

3. For secondary vertices reconstructed outside the Vertex Detector, candidates were rejected if there were two or more VXD hits consistent with either of the two charged tracks.

4. In the plane perpendicular to the beam, the angle between the vector sum of the momenta of the two charged tracks and the line joining the IP to the secondary vertex was required to be less than $k \cdot (2 + 20/p_t + 5/p_t^2)$ mrad (up to a maximum deviation of 60 mrad). Here, p_t is in units of GeV/c and k=1.75 for $\Lambda^0/\bar{\Lambda}^0$ candidates and 2.5 for K_s^0 candidates (see below).

5. For $\Lambda^0/\bar{\Lambda}^0$ candidates, a minimum vector-sum momentum of 500 MeV/c was required.

For the V^0 candidates, two invariant mass calculations were performed. The pion masses were assigned to both tracks and the invariant mass of the pair $m_{\pi\pi}$ was calculated, using the charged tracks' momenta at the fitted vertex position. The 42460 V^0 candidates whose $m_{\pi\pi}$ were in the mass window between 400 and 600 MeV/c^2 were regarded as K_s^0 candidates. The invariant mass of the charged track pair was also calculated assuming the higher momentum charged track to have the proton mass ($m_{p\pi}$). The 39804 V^0 candidates whose $m_{p\pi}$ were in the mass window between 1.075 and 1.215

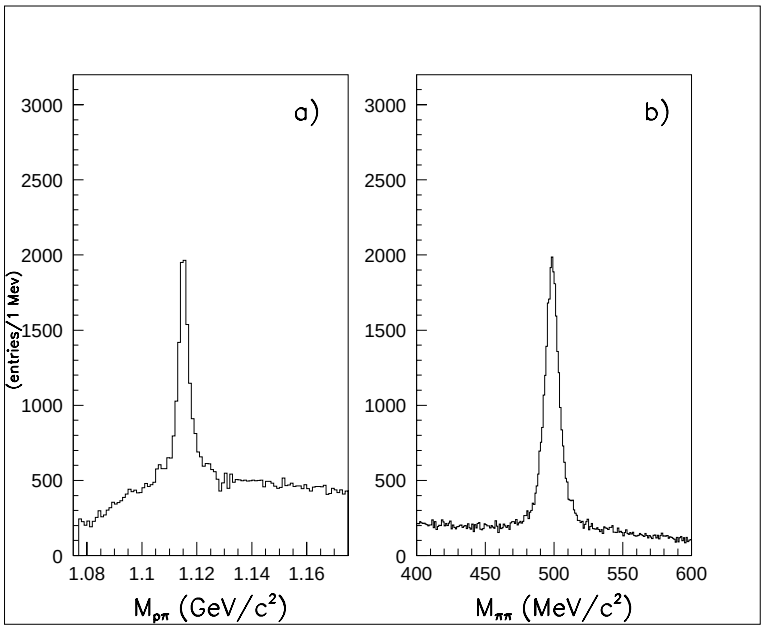

Figure 6.1: Invariant mass plots for (a) the $p\pi$ hypothesis, and (b) the $\pi\pi$ hypothesis, after cuts 1-5 were applied to select V^0 candidates.

MeV/c^2 were regarded as $\Lambda^0/\bar{\Lambda}^0$ candidates. When plotting the $\pi\pi$ and $p\pi$ invariant masses, clear peaks are visible in the distributions (Fig. 6.1).

Without the aid of particle identification, there are kinematic regions populated by both $\Lambda^0/\bar{\Lambda}^0$'s and K_s^0 decays. Depending upon the type of analysis, the kinematic-overlap region may introduce important biases. In this analysis, the kinematic-overlap region was removed where it distorts the invariant mass distributions.

For the K_s^0 analysis, the $\Lambda^0/\bar{\Lambda}^0$ background causes an asymmetric "bump" in the $\pi\pi$-invariant mass distribution, as seen in Figure 6.2, which complicated the fitting procedure. A cut on the "helicity angle" θ^*, defined as the angle between the π^+ momentum vector in the K_s^0 rest frame and the K_s^0 flight direction, was used to remove the Λ^0 and $\bar{\Lambda}^0$ contamination (Fig. 6.3). K_s^0 candidates were required to have $|cos\theta^*| \leq 0.8$, which removed 20% of the K_s^0 signal. This cut also removes the γ-conversion background.

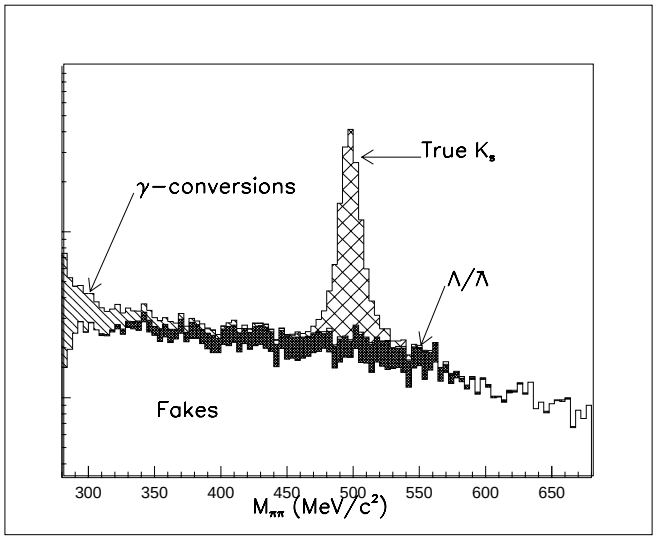

Figure 6.2: The simulated $K_s^0 \rightarrow \pi^+\pi^-$ signal along with the various background distributions. The cuts on the K_s^0 helicity angle remove the $\Lambda^0/\bar{\Lambda}^0$ and γ-conversion backgrounds. (Note: the vertical scale is logarithmic)

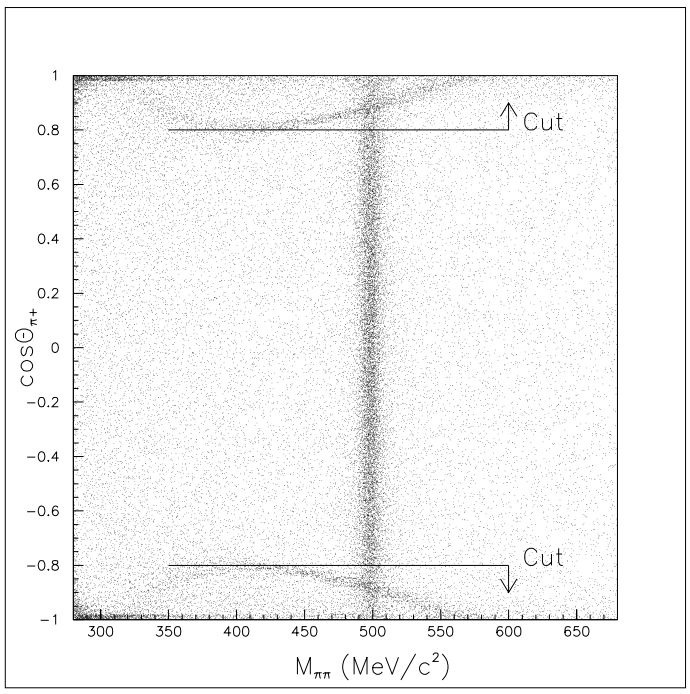

Figure 6.3: A scatter plot of the helicity angle of the π^+ (see text) versus the $\pi\pi$ invariant mass for the K_s^0 candidates in the data. The vertical K_s^0 band is clearly visible. The lower and upper curved bands are due to the Λ^0 and the $\bar{\Lambda}^0$ (respectively) in the sample. The darkened regions at the upper- and lower-left corners are due to γ-conversions.

For the $\Lambda^0/\bar{\Lambda}^0$ analysis, the shape of the K_s^0 background depends on momentum. Above a V^0 momentum of a few GeV/c, the $K_s^0 \rightarrow \pi\pi$ background is essentially uniform in the peak region of the $p\pi$ invariant-mass distribution (see Figure 6.4), and no cuts were made to remove the K_s^0 overlap. At sufficiently low momentum, the K_s^0 background becomes asymmetric under the $\Lambda^0/\bar{\Lambda}^0$ peak due to detector acceptance; the "soft" π fails to be reconstructed and thus the K_s^0 is not found. Therefore, below 1.8 GeV/c a mass cut was applied to remove the K_s^0 contamination. This cut (see Fig. 6.5) removed all $\Lambda^0/\bar{\Lambda}^0$ candidates whose $\pi\pi$ invariant mass was within 3σ of the K_s^0 mass (up to a maximum deviation of 30 MeV/c^2). It does not significantly affect the combinatoric background. Figure 6.6 demonstrates the momentum-dependence of the K_s^0 mass resolution in the MC simulation.

Another source of physics background for both K_s^0's and $\Lambda^0/\bar{\Lambda}^0$'s is the gamma conversion process $\gamma \rightarrow e^+e^-$ in the presence of an atomic nucleus. These gamma conversions also provide a kinematic-overlap region with either the K_s^0 or the $\Lambda^0/\bar{\Lambda}^0$ decays. These may be removed from the V^0 sample by several methods: particle identification for either of the charged tracks (discussed below), invariant mass cuts for the e^+e^- hypothesis, or by cuts on the helicity angle distribution (see Figures 6.3 and 6.7). For the K_s^0 analysis, no explicit cut was needed due to the helicity angle cuts used to reject $\Lambda^0/\bar{\Lambda}^0$'s. For the $\Lambda^0/\bar{\Lambda}^0$ analysis, the proton helicity angle was required to satisfy $\cos\theta^* \geq -0.95$. This removed approximately 2.5% of the $\Lambda^0/\bar{\Lambda}^0$ signal[1].

6.2.1 Using the CRID to obtain a High Purity $\Lambda^0/\bar{\Lambda}^0$ Sample

While not used in this analysis, it is interesting to demonstrate the uses of the SLD CRID for obtaining high-purity $\Lambda^0/\bar{\Lambda}^0$ samples. To do so, we will remove the $m_{\pi\pi}$ cut and examine the particle type of the high-momentum track of the $\Lambda^0/\bar{\Lambda}^0$ candidate. From kinematics, if a $\Lambda^0/\bar{\Lambda}^0$ of momentum above $\sim 301 MeV/c$ decays into the $p\pi$ mode, the proton has a higher momentum track in the lab frame than the pion. Due to the nature of the background ($\sim$ 90% pions) under the mass peak, it is sufficient to

[1] As the $\Lambda^0/\bar{\Lambda}^0$ may be polarized, the cut does not necessarily remove *exactly* 2.5% of the signal.

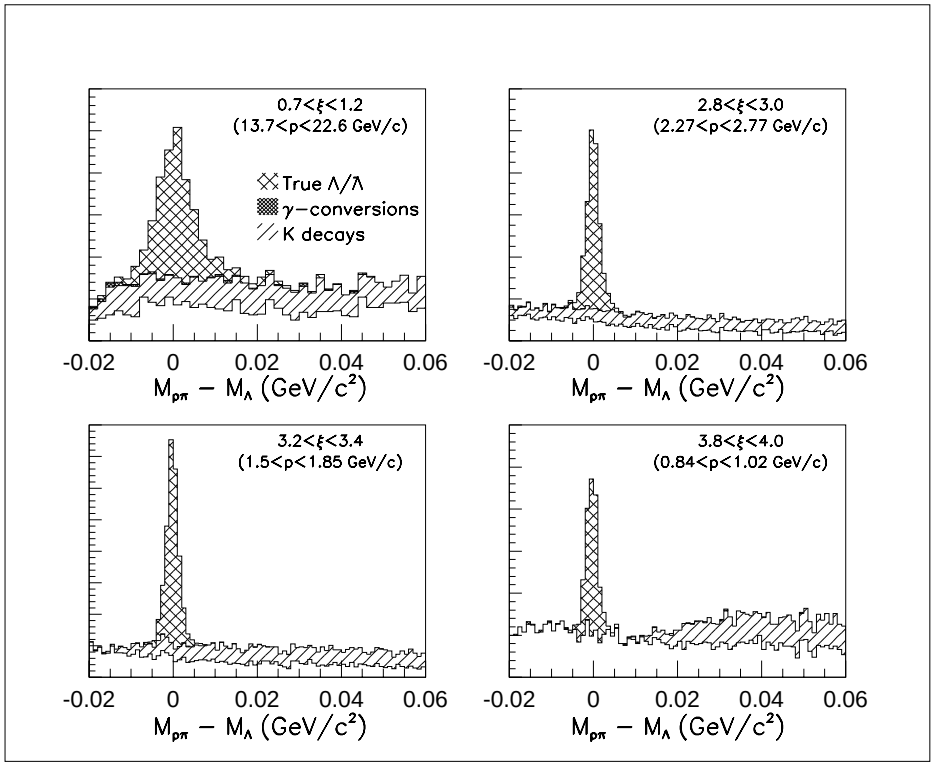

Figure 6.4: The distribution of $M_{p\pi} - M_{\Lambda^0}$ for MC $\Lambda^0/\bar{\Lambda}^0$candidates. The contributions of γ-conversions and K_s^0 decays to the background are indicated. The γ-conversions are removed by a helicity cut (text). At sufficiently low momentum, a mass cut is required to remove the K_s^0 contribution.

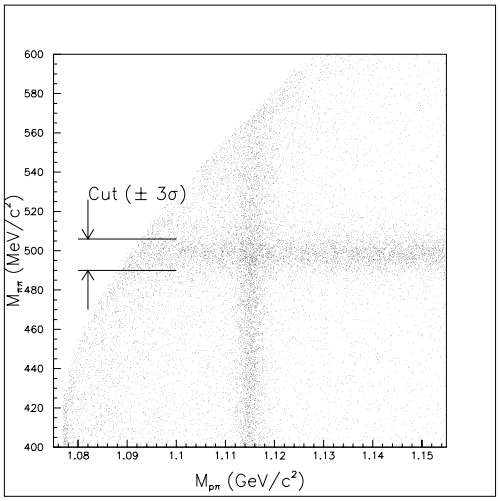

Figure 6.5: A scatter plot of the $\pi\pi$ invariant mass vs. the $p(\bar{p})\pi$ invariant mass for the $\Lambda^0/\bar{\Lambda}^0$ candidates in the data sample that pass the selection cuts. The K_s^0 contamination is removed from the $\Lambda^0/\bar{\Lambda}^0$ sample by cutting out the candidates whose invariant mass is within 3σ of the K_s^0 mass, up to a maximum deviation of 30 MeV/c^2. The kinematic edge is clearly visible.

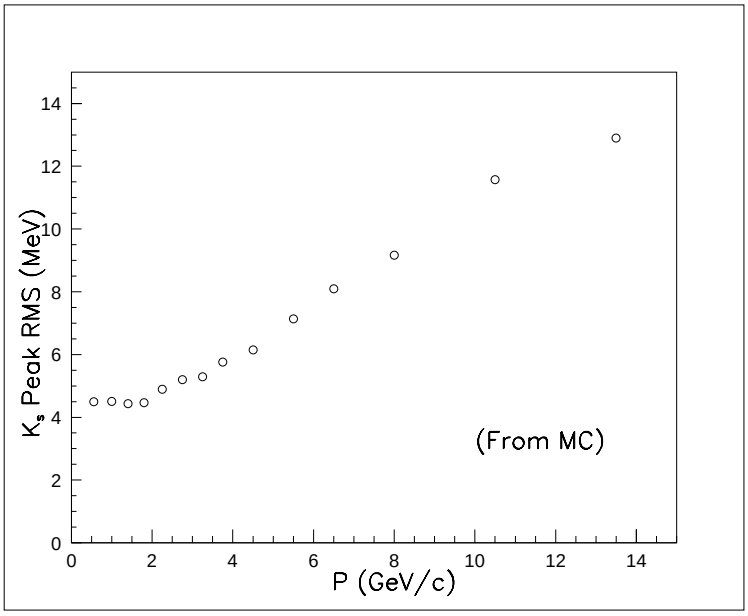

Figure 6.6: The RMS width of the MC $\pi\pi$ invariant mass distribution due to K_s^0 decays.

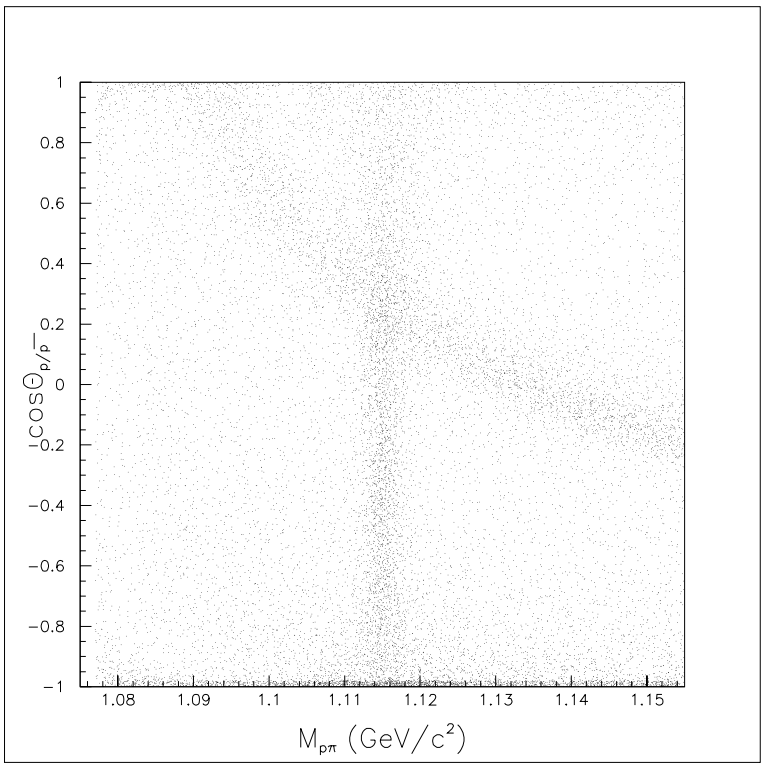

Figure 6.7: A scatter plot of the of the helicity angle of the $p(\bar{p})$ in the rest frame of the $p(\bar{p})\pi$ combination versus the $p(\bar{p})\pi$ invariant mass. The vertical $\Lambda^0/\bar{\Lambda}^0$ band is clearly visible. The curved band is due to the $K_s^0 \rightarrow \pi\pi$ contamination in the sample. The horizontal band near $cos\theta = -1$ is due to γ-conversion contamination.

consider only the p and π hypotheses.

A 3×3 efficiency matrix for the identification of π's, K's and $p(\bar{p})$ is shown in Figure 6.8. This matrix, which was computed using detailed detector simulation, has been calibrated with data. The outstanding feature of the CRID is its ability to perform particle identification over a wide momentum range.

For this demonstration, the Barrel CRID information is used in two different operating modes to clean up the $\Lambda^0/\bar{\Lambda}^0$ signal. In the high-efficiency mode, the $\Lambda^0/\bar{\Lambda}^0$ candidate is rejected only if the CRID data indicates that the high momentum track is definitely a pion. In the event that the identification is ambiguous or the CRID subsystem was not operational during the time the data was recorded (eg., during periods of high background in the detector), the $\Lambda^0/\bar{\Lambda}^0$ candidate is not rejected. This removes a significant portion of the background with only a few percent loss of signal. In the high-purity mode, which may be required for analyses such as studying Λ^0 polarization, the $\Lambda^0/\bar{\Lambda}^0$ candidate is retained only if the high-momentum track is positively identified as a $p/\bar{p}$. This mode produces a very pure sample, but at much lower efficiencies (Fig. 6.9).

6.3 Production Rates, Spectra and Lifetimes in Hadronic Z^0 Decays

The V^0 candidates were binned in terms of $\xi = -\ln(x_p)$, where $x_p = p_{V^0}/p_{beam}$ is the V^0 momentum scaled by the beam momentum. The kinematic cuts described in the last section were applied. The resulting invariant mass distributions were then fitted with various peak and background shapes using the program MINUIT [59]. The nominal shape used to fit the signal (mass peak) was a sum of two gaussians of common center:

$$P_{signal}(m) = \frac{1}{\sqrt{2\pi}}(Area) \times (\frac{f_1}{s_f\sigma_1}e^{\frac{-(m-m_0)^2}{2(s_f\sigma_1)^2}} + \frac{1-f_1}{s_f\sigma_2}e^{\frac{-(m-m_0)^2}{2(s_f\sigma_2)^2}}). \tag{6.1}$$

The relative fractions of the two gaussians f_1 and $f_2 = 1 - f_1$ and the nominal widths σ_1 and σ_2 were fixed from MC simulation. The area, common center m_0, and the resolution scale-factor s_f were free parameters of the fit. In most cases, a single gaussian did not give an adequate fit. This is to be expected as the mass-resolution is momentum-dependent and fairly large momentum bins were used. In some cases, three gaussians

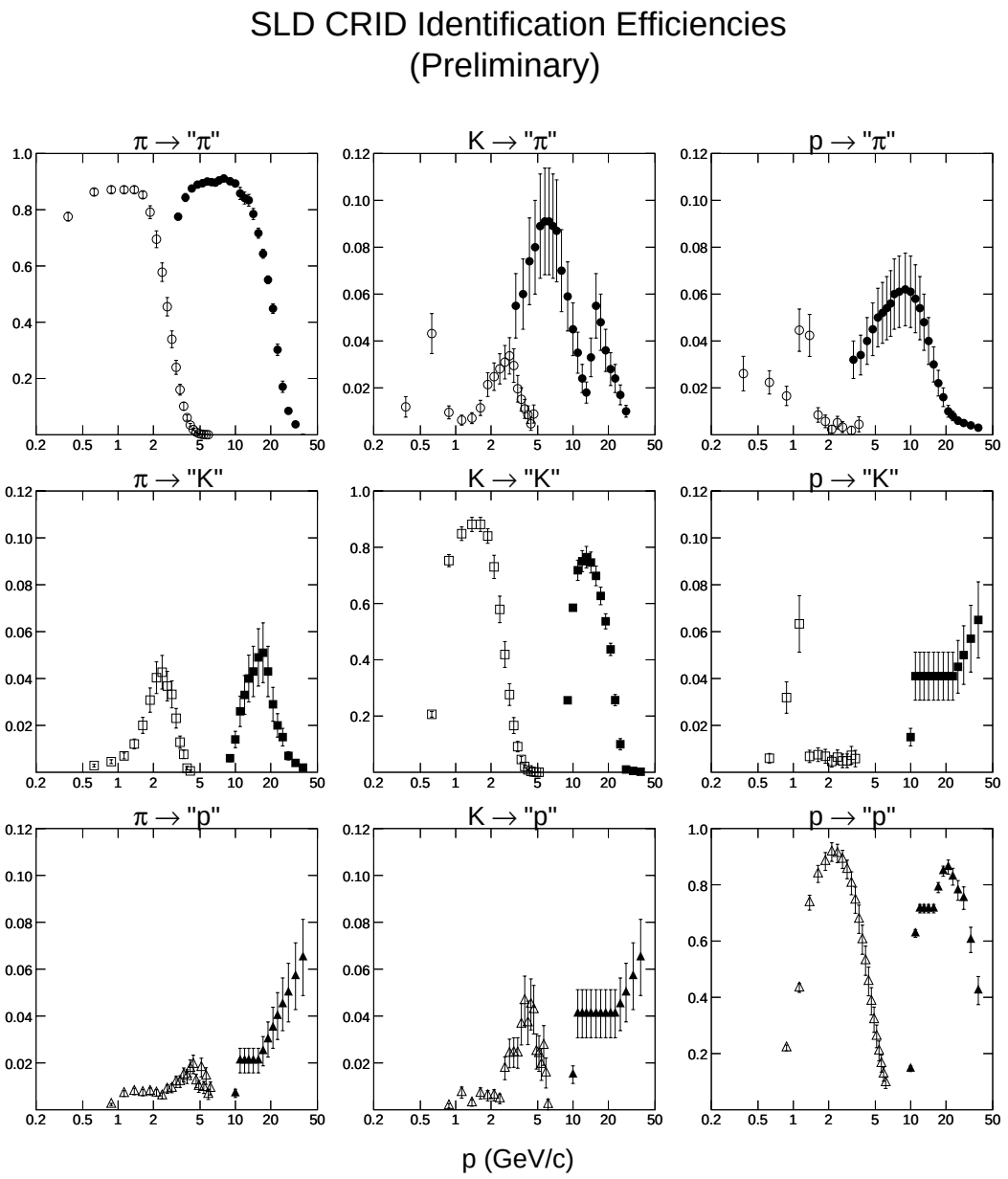

Figure 6.8: The particle identification efficiencies and mis-identification rates for the SLD Barrel CRID.

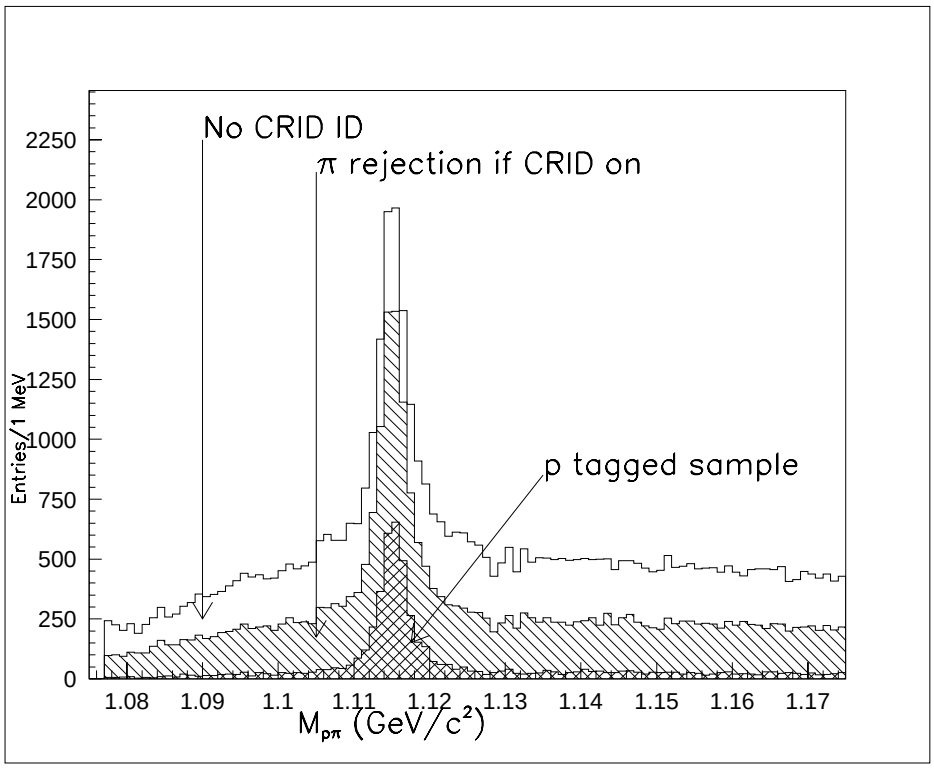

Figure 6.9: The $p\pi$ invariant mass distribution for selected data V^0 candidates (including the K_s^0 contamination). Significant background reduction can be obtained by rejecting V^0's whose high-momentum tracks are consistent with the π hypothesis. A very pure $\Lambda^0/\bar{\Lambda}^0$ sample can be obtained by requiring the high momentum track to be tagged by the CRID as a proton.

were needed. The nominal background shape used for the K_s^0 fits was a quadratic; for the Λ^0 fits a more complicated function was required due to the proximity of the kinematic edge to the mass peak. The function, $P_{bkg}(m) = a + b(m - m_0) + c(1 - e^{d((m-m_0)-0.038)})$, was found to be adequate in MC studies. In each bin of momentum, the $m_{p\pi}$ or $m_{\pi\pi}$ distributions were fitted using the sum of the P_{signal} and P_{bkg} shapes. Sample fits of the data for various momentum distributions are shown in Figure 6.10. Tables 6.1 and 6.2 show the parameter values used in the fits, and the quality of the fit to the data.

For each bin, the simulated data (data from MC generation, followed by a detailed detector simulation) was treated in the same manner as the true data. Using the fitted area of the MC peak ($N_{recon}^{V^0 \to X^+X^-}$) and the generated MC spectrum ($N_{gen}^{V^0 \to all}$), the V^0

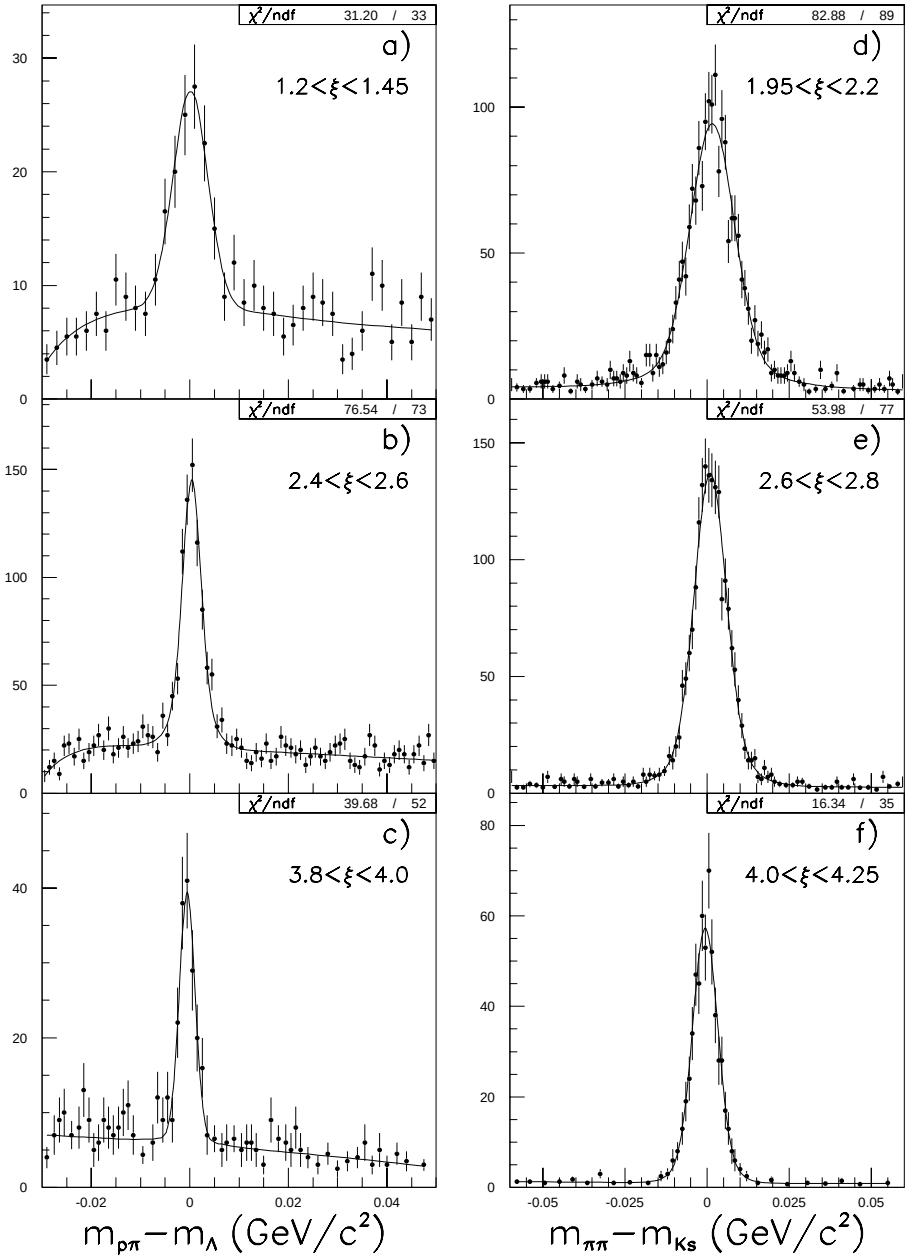

Figure 6.10: Sample invariant mass peaks from the data for $\Lambda^0/\bar{\Lambda}^0 \rightarrow p(\bar{p})\pi$ (a-c) and $K_s^0 \rightarrow \pi\pi$ (d-f) for low, medium, and high ξ bins.

ξ range	p-range (GeV/c)	f_1	σ_1 (MeV/c^2)	σ_2 (MeV/c^2)	χ^2/dof
0.70-1.20	13.73-22.64				72.1/78
1.20-1.45	10.70-13.73	0.63	8.2	20.1	59.6/74
1.45-1.70	8.33-10.70	0.69	7.5	18.4	79.0/80
1.70-1.95	6.49- 8.33	0.74	6.3	15.6	89.2/84
1.95-2.20	5.05- 6.49	0.81	5.7	13.4	82.8/89
2.20-2.40	4.14- 5.05	0.64	4.3	8.7	78.3/82
2.40-2.60	3.39- 4.14	0.77	4.4	9.3	68.4/76
2.60-2.80	2.77- 3.39	0.79	4.2	8.6	54.0/77
2.80-3.00	2.27- 2.77	0.78	3.9	7.3	56.4/68
3.00-3.20	1.86- 2.27	0.72	3.6	6.7	67.6/66
3.20-3.40	1.52- 1.86	0.68	3.5	6.2	38.8/60
3.40-3.60	1.25- 1.52	0.70	3.5	6.3	52.4/57
3.60-3.80	1.02- 1.25	0.83	3.7	7.6	60.6/52
3.80-4.00	0.84- 1.02	0.48	3.1	5.4	27.0/44
4.00-4.25	0.65- 0.84	0.83	3.8	6.8	16.3/35
4.25-4.50	0.51- 0.65	0.77	3.8	7.0	27.0/24
4.50-4.75	0.40- 0.51	1.00	4.3		12.7/18

Table 6.1: The signal parameters (obtained from MC) used in the fitting of the $K_s^0 \to \pi\pi$ signal. The background shape used was $a + bm + cm^2$. For the lowest ξ bin (highest momentum), 3 gaussians were needed to describe the peak adequately. For the highest ξ bin, a single gaussian was sufficient.

reconstruction efficiency in each bin was calculated:

$$\mathcal{R}(\xi) = \frac{N_{recon}^{V^0 \to X^+ X^-}(\xi)/N_{recon}^{events}}{N_{gen}^{V^0 \to all}(\xi)/N_{gen}^{events}}. \tag{6.2}$$

Here N_{gen}^{events} is the total number of generated MC events, and N_{recon}^{events} is the total number of reconstructed MC events that passed the hadronic event selection (Section 5.3). Several checks were performed to gain confidence in the MC simulation, and thus the V^0 reconstruction efficiency. In general there was good agreement between the data and the MC, however two important discrepancies were found. First of all, it was noted that there was a 2% excess in the average number of reconstructed tracks per event in the MC with respect to the data both before and after the track quality cuts were applied. Since the MC was tuned using the world-average measured charged multiplicity in hadronic Z^0 decays [60], we ascribe the difference to mismodelling of the overall track reconstruction efficiency. To remedy this, an algorithm was used to remove tracks randomly from the MC until the number of charged tracks was in agreement with the

ξ range	p-range (GeV/c)	f_1	σ_1 (MeV/c^2)	σ_2 (MeV/c^2)	χ^2/dof
0.70-1.20	13.73-22.64				29.1/30
1.20-1.45	10.70-13.73	0.842	3.43	16.64	31.2/33
1.45-1.70	8.33-10.70	0.390	5.05	2.28	55.3/72
1.70-1.95	6.49- 8.33	0.768	2.10	5.06	92.8/73
1.95-2.20	5.05- 6.49	0.631	1.63	3.76	50.0/73
2.20-2.40	4.14- 5.05	0.717	1.59	3.75	80.3/73
2.40-2.60	3.39- 4.14	0.692	1.49	3.04	76.5/73
2.60-2.80	2.77- 3.39	0.620	1.38	2.69	83.2/73
2.80-3.00	2.27- 2.77	0.687	1.27	2.51	109.1/73
3.00-3.20	1.86- 2.27	0.854	1.38	3.60	84.0/74
3.20-3.40	1.52- 1.86	0.439	0.97	1.93	57.5/60
3.40-3.60	1.25- 1.52	0.374	0.80	1.81	45.3/61
3.60-3.80	1.02- 1.25	1.000	1.57		43.4/58
3.80-4.00	0.84- 1.02	1.000	1.43		39.7/52
4.00-4.50	0.51- 0.84	1.000	1.50		53.6/63

Table 6.2: The signal parameters (obtained from MC) used in the fitting of the $\Lambda(\bar{\Lambda}) \rightarrow p(\bar{p})\pi$ signal. For the three highest ξ bins (lowest momentum), a single gaussian fit was sufficient to describe the peak. For the lowest ξ bin, 3 gaussians were required.

data. Secondly, while it is not reasonable to expect that the number of V^0's per event be the same for the data and the MC, it is reasonable to expect that the detector behavior be the same for both samples. For both data and MC, the number of reconstructed V^0's was studied as a function of several variables, including V^0 momentum, V^0 decay radius, and polar angles of the V^0 momentum. Agreement between the data and the MC was good except when considering the number of reconstructed V^0's as a function of reconstructed vertex radius (with respect to the IP). A large discrepancy was observed (Fig. 6.11) between the data and the MC, which indicated that some portion of the tracking system was not being modelled correctly. It is hypothesized that this is due to the problem of mis-linking VXD hits with CDC measured tracks, thereby drastically reducing the error ellipse of the mis-linked track (or, more accurately, the *mis-modelling* of this effect). This would cause the V^0's to fail the fit probability cut discussed in section 6.2. This problem does not exist for V^0's with decay radius above $R = 2cm$, as those V^0's are always reconstructed using CDC-only tracks (i.e. for V^0's with $r > 2cm$, the VXD information is not used, even if it exists). An ad hoc "V^0-tossing" procedure

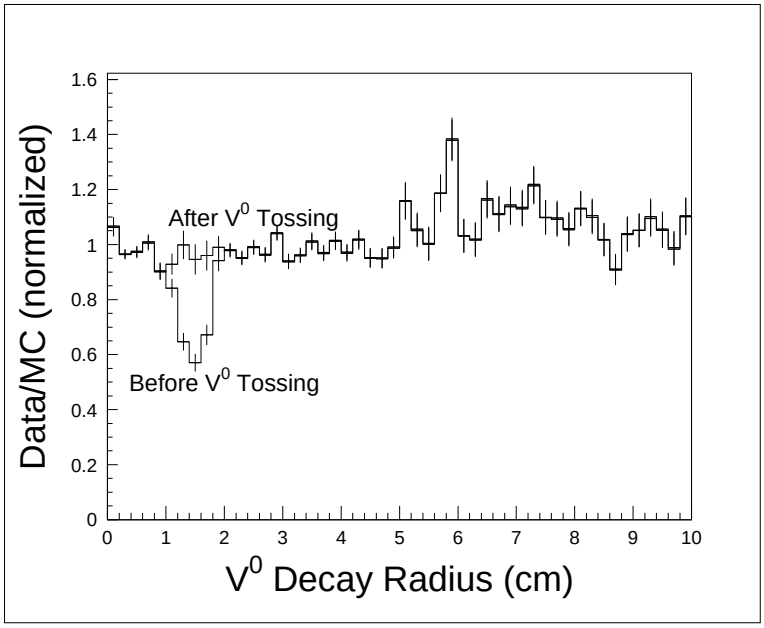

Figure 6.11: The ratio of the number of V^0 in the MC to that in the data as a function of reconstructed radius, before and after the ad hoc V^0 algorithm was used. The MC has been normalized to the total number of data V^0's.

was applied to degrade the MC V^0 reconstruction efficiency in this region by removing MC V^0's until the Data/MC radial distribution was smoothly varying. This procedure was found not to affect the other distributions mentioned above.

After these corrections were applied, the reconstruction efficiencies for $\Lambda^0/\bar{\Lambda}^0$'s and K_s^0's were calculated, and are shown in Figure 6.12. These curves have three main features: 1) the reconstruction efficiency is limited by the detector acceptance ($\sim .67$) $\times$ the charged decay branching fraction (.64 for $\Lambda^0/\bar{\Lambda}^0$'s and .68 for K_s^0's); 2) the efficiency at high momentum (low ξ) decreases due to finite detector size and two-track detector resolution; 3) the efficiency at low-momentum (high ξ) is limited by minimum p_T and flight distance requirements. The discontinuity in the $\Lambda^0/\bar{\Lambda}^0$ reconstruction efficiency is due to the imposed K_s^0 mass cut for high-ξ candidates. The smooth parameterizations shown were used in the analysis; the individual points show the magnitude of the uncertainty due to MC statistics.

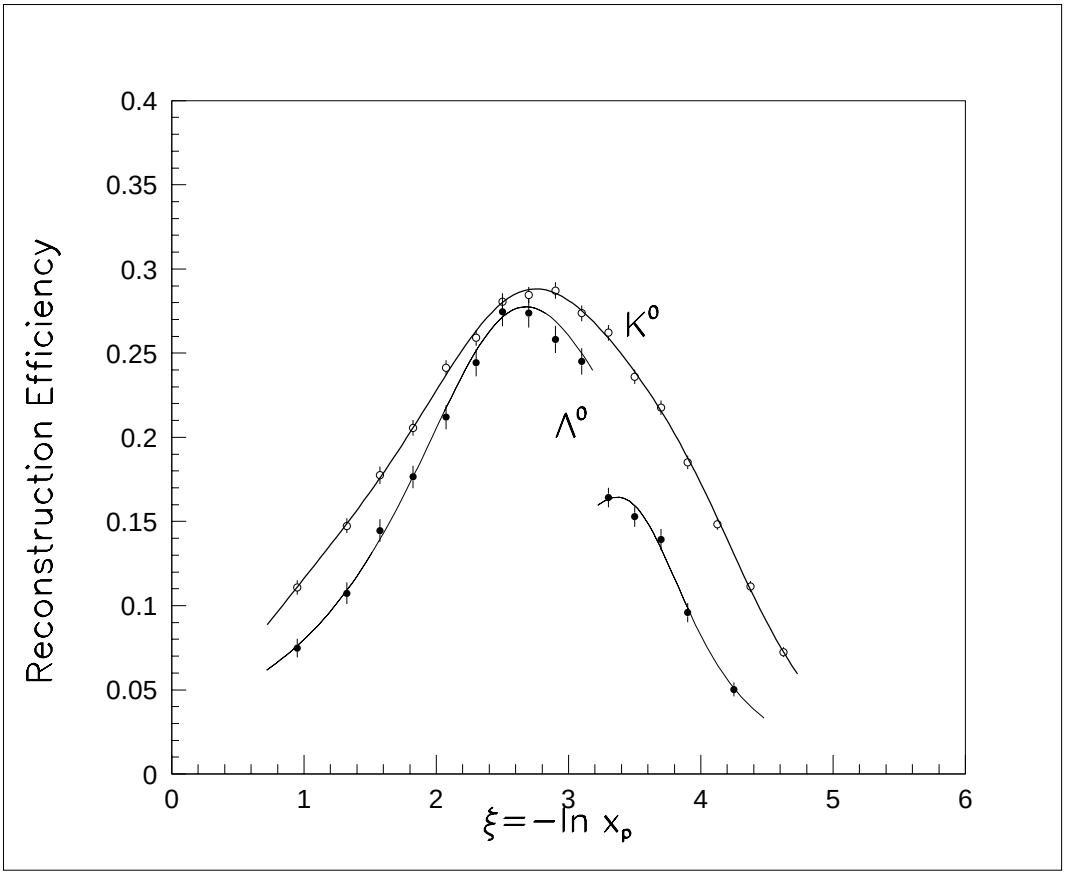

Figure 6.12: The reconstruction efficiencies for K_s^0 and $\Lambda^0/\bar{\Lambda}^0$ (from MC). The charged decay branching ratios are included in the efficiency. Note the discontinuity in the $\Lambda^0/\bar{\Lambda}^0$ reconstruction efficiency; this is due to the invariant-mass cut to remove low momentum K_s^0's.

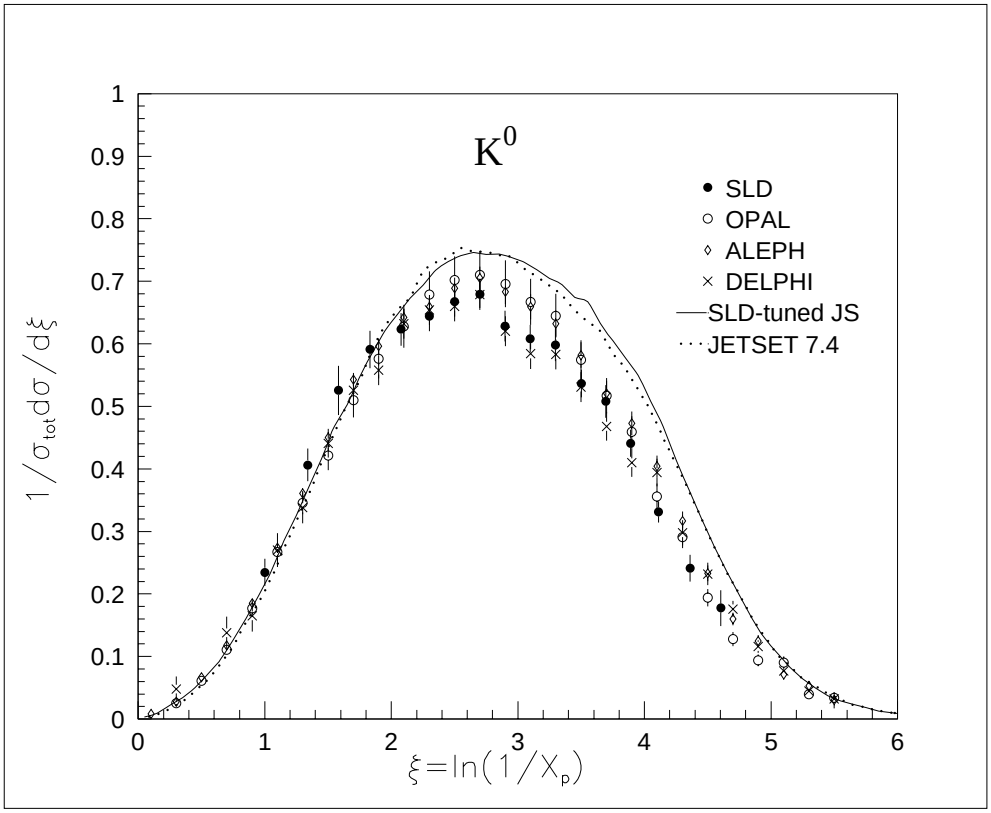

Figure 6.13: The production spectrum of K^0 in hadronic Z^0 events (filled circles). Also shown are published data from the LEP experiments, and the predictions of the "SLD-tuned" JETSET 7.4 MC (solid line), and the default JETSET 7.4 (dotted line). The correlated errors are not shown.

The inclusive cross section $1/\sigma_{tot}\, d\sigma/d\xi$ is then calculated from the number of particles observed in each momentum slice:

$$\frac{1}{\sigma_{tot}}\frac{d\sigma}{d\xi} = \frac{1}{\mathcal{R}(\xi)}\frac{1}{\Delta\xi}\frac{N_{obs}(\xi)}{N_{recon}^{events}} \tag{6.3}$$

(here, σ_{tot} is the total hadronic cross-section, N_{obs} is the integrated area under the mass peak, and $\Delta\xi$ is the bin width). As is conventional, when quoting K^0 (i.e. $K^0 + \bar{K}^0$) production spectra, the K_s^0 production spectra is multiplied by a factor of 2 to account for the undetected K_L^0 component. The resulting spectra, including point-to-point systematic errors (discussed below), are shown in Figures 6.13 and 6.14, and are listed in Tables 6.3 and 6.4.

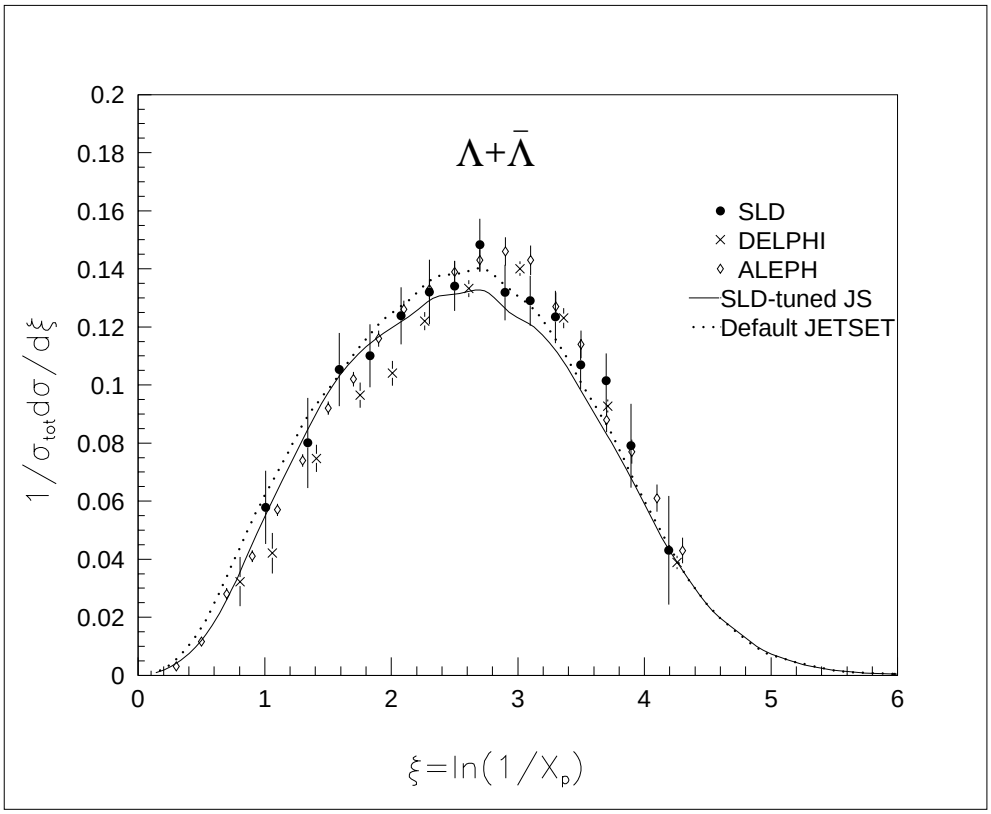

Figure 6.14: The production spectrum of $\Lambda^0+\bar{\Lambda}^0$ in hadronic Z^0 events (filled circles). Also shown are published data from the LEP experiments, and the predictions of the "SLD-tuned" JETSET 7.4 MC (solid line), and the default JETSET 7.4 (dotted line). The correlated errors are not shown.

ξ range	$\frac{1}{\sigma_{tot}}\frac{d\sigma}{d\xi} \pm (stat.)$	systematics					
		fitting	V^0 select.	MC stats.	total uncor.	MC (r)	total corr.
0.70-1.20	0.234 ± 0.019	-	-	0.009	0.009	0.001	0.008
1.20-1.45	0.406 ± 0.022	-	-	0.012	0.012	0.001	0.014
1.45-1.70	0.526 ± 0.035	-	-	0.015	0.015	0.002	0.018
1.70-1.95	0.591 ± 0.026	-	-	0.013	0.013	0.002	0.020
1.95-2.20	0.623 ± 0.020	-	-	0.012	0.012	0.003	0.021
2.20-2.40	0.644 ± 0.020	-	-	0.012	0.012	0.003	0.022
2.40-2.60	0.668 ± 0.019	-	-	0.012	0.012	0.004	0.023
2.60-2.80	0.679 ± 0.018	-	-	0.011	0.011	0.005	0.024
2.80-3.00	0.629 ± 0.017	-	-	0.011	0.011	0.005	0.022
3.00-3.20	0.608 ± 0.017	-	-	0.010	0.010	0.006	0.021
3.20-3.40	0.598 ± 0.017	-	-	0.010	0.011	0.007	0.021
3.40-3.60	0.536 ± 0.017	-	0.001	0.010	0.010	0.007	0.020
3.60-3.80	0.508 ± 0.017	-	0.002	0.010	0.010	0.008	0.019
3.80-4.00	0.441 ± 0.017	-	0.007	0.009	0.012	0.009	0.017
4.00-4.25	0.331 ± 0.015	-	0.001	0.008	0.008	0.008	0.014
4.25-4.50	0.241 ± 0.015	-	0.010	0.007	0.013	0.007	0.011
4.50-4.75	0.178 ± 0.017	-	0.022	0.007	0.023	0.006	0.009
0.70-4.75	1.904 ± 0.021				0.012		0.069

Table 6.3: The production spectrum for K^0 in hadronic Z^0 decays, along with statistical, uncorrelated, and correlated errors (discussed in text). Entries marked with a dash had less than a 5×10^{-4} contribution. The total integrated production rate (and errors) per hadronic Z^0 decay for the measured region are also shown.

6.3.1 Systematic Errors and Checks

There are four sources of systematics that were investigated in the analysis. Two of them, the overall normalization and the MC-data differences, are completely correlated over all momentum bins. The other two sources, V^0 selection systematics and fit systematics, are essentially independent.

An important contribution to the overall V^0 spectrum is the track reconstruction efficiency of the detector. As noted in section 6.2 the efficiency has been tuned using the world average measured charged multiplicity in hadronic Z^0 decays. We take a reasonable error of $\pm 1.7\%$ [60] on the world average as the error on our reconstruction efficiency, which corresponds to a *normalization* error on the K^0 and Λ^0+$\bar{\Lambda}^0$ production rates of 3.4%. This uncertainty is independent of momentum and is not shown in any

ξ range	$\frac{1}{\sigma_{tot}}\frac{d\sigma}{d\xi} \pm (stat.)$	systematics					
		fitting	V^0 select.	MC stats.	total uncor.	MC (r)	total corr.
0.70-1.20	0.058 ± 0.008	0.009	-	0.004	0.010	-	0.002
1.20-1.45	0.080 ± 0.010	0.011	-	0.005	0.012	-	0.003
1.45-1.70	0.105 ± 0.010	0.006	-	0.005	0.008	-	0.004
1.70-1.95	0.110 ± 0.008	0.005	-	0.004	0.007	-	0.004
1.95-2.20	0.124 ± 0.007	0.005	-	0.004	0.007	-	0.004
2.20-2.40	0.132 ± 0.008	0.007	-	0.004	0.008	-	0.004
2.40-2.60	0.134 ± 0.007	0.003	0.001	0.004	0.005	-	0.005
2.60-2.80	0.148 ± 0.007	0.004	0.002	0.005	0.006	-	0.005
2.80-3.00	0.132 ± 0.006	0.004	0.004	0.004	0.007	-	0.004
3.00-3.20	0.129 ± 0.006	0.003	0.003	0.004	0.006	-	0.004
3.20-3.40	0.123 ± 0.007	0.003	0.001	0.004	0.005	-	0.004
3.40-3.60	0.107 ± 0.007	0.002	-	0.004	0.005	-	0.004
3.60-3.80	0.101 ± 0.007	0.003	0.002	0.005	0.006	0.001	0.003
3.80-4.00	0.079 ± 0.008	0.002	0.011	0.005	0.012	0.001	0.003
4.00-4.50	0.043 ± 0.007	0.004	0.017	0.003	0.018	-	0.002
0.70-4.50	0.373 ± 0.008				0.012		0.013

Table 6.4: The production spectrum for $\Lambda^0 + \bar{\Lambda}^0$ in hadronic Z^0 decays, along with statistical, uncorrelated, and correlated errors (discussed in text). Entries marked with a dash had less than a 5×10^{-4} contribution. The total integrated rate production rate (and errors) per hadronic Z^0 decay for the measured region are also shown.

of the figures.

The effect due to the correction of the MC simulation for the radius-dependent V^0 reconstruction efficiency is also a correlated error; however it is not momentum independent. This "gap" in the reconstruction efficiency affects V^0's with low proper decay lengths $l/\beta\gamma$ (and thus low momentum V^0s), more than V^0's with high proper decay length. It also affects K_s^0's (and the K^0's) more than $\Lambda^0/\bar{\Lambda}^0$'s due to the differences in the lifetimes (see below). A conservative 50% variation on the number of V^0's removed from the MC was used to estimate this contribution; this contribution is shown in the "MC(r)" column in Tables 6.3 and 6.4. For each bin, this contribution was added in quadrature with the normalization error to obtain the total correlated error, shown in the last column of these tables.

Each of the cuts used to select V^0 candidates (see Section 6.1) was varied independently for both the MC and the data, and the spectra were recomputed. For each ξ-bin

the *rms* of this set of measurements was calculated and assigned as the systematic uncertainty.

For both the K^0 and the $\Lambda^0/\bar{\Lambda}^0$ candidates, the peak shapes used in the fit were varied. Single and multiple independent gaussians (gaussians without common centers and fixed widths) were used for both the data and the MC. The background shapes were also varied in the same manner, and included constants and polynomials of differing orders. Once again, for each variation the spectra were recomputed and the *rms* for each bin was assigned as a systematic uncertainty.

While not a systematic error in the classic sense, the MC statistical error for each bin in the reconstruction efficiency computation was also considered.

As a crosscheck to examine possible momentum or decay length biases in the V^0 reconstruction or selection, measurements of the particle lifetimes were made. The data was binned in proper decay length, $l/\beta\gamma$, and the above fitting procedure was repeated. The measured lifetimes, shown in Table 6.5, are in good agreement with the world averages [5].

Particle	Measured $c\tau$	World Average
K_s^0	2.62 ± 0.07 cm	2.675 cm
$\Lambda^0/\bar{\Lambda}^0$	7.25 ± 0.38 cm	7.89 cm

Table 6.5: The measured lifetimes for the K_s^0 and the Λ^0. The errors are statistical only.

6.4 Rates and Comparisons with Other Experiments

In addition to our measurements, Figures 6.13 and 6.14 show measurements made by several of the LEP collaborations [61, 62]. Our measurement for the $\Lambda^0+\bar{\Lambda}^0$ production spectrum is in good agreement with those of the other experiments. Our measurement for the K^0 production spectrum is consistent with all of the LEP measurements, although there is a suggestion that SLD and DELPHI measurements are systematically below those of ALEPH and OPAL in the range $2.8 < \xi < 3.6$.

Also shown in each of these figures are the generator-level spectra predicted by both

the SLD-tuned JETSET 7.4 generator and the Default JETSET 7.4 generator. In both cases the MC reasonably agrees with the measured $\Lambda^0+\bar{\Lambda}^0$ spectrum and overestimates the K^0 production spectrum for $\xi > 3.0$ ($p < 2.25\ GeV/c$).

The spectra were integrated over the visible regions, and the MC was used to estimate the relative contribution due to the unobserved regions. The measured, extrapolated, and total production rates for K^0 and $\Lambda^0+\bar{\Lambda}^0$ in hadronic Z^0 decays are shown in Table 6.6. The error on the extrapolated rate is due to the way the MC is normalized to the data to determine the unobserved fraction– either over the entire observable range, or just over portions where the MC and the data agree. The world averages are calculated in [52].

Particle	Observed Rate	Extrapolated Rate	Total Rate	Norm. Uncer.	World Ave.
K^0	$1.904 \pm .021 \pm .007$	$.097 \pm .003 \pm .008$	$2.001 \pm .021 \pm .011$	0.068	2.03 ± 0.04
$\Lambda^0+\bar{\Lambda}^0$	$0.373 \pm .008 \pm .012$	$.017 \pm .001 \pm .001$	$0.390 \pm .011 \pm .017$	0.013	0.37 ± 0.01

Table 6.6: The integrated production rates (per event) in Hadronic Z^0 decays.

6.5 Comparisons with QCD

As discussed in Chapter 2, QCD calculations based upon the modified leading log approximation (MLLA) predict the shape of the ξ-distribution for soft partons. Under the assumption of local parton-hadron duality (LPHD), this shape should be directly comparable with that of observed hadrons. The $\xi-$distribution is expected to be approximately gaussian in nature, with the peak position being (inversely) dependent upon the hadron mass.

Figures 6.15 and 6.16 show the ξ-distributions for the K^0 and $\Lambda^0+\bar{\Lambda}^0$, along with the best-fit gaussian to all the data points. Good agreement is observed between the curve and the $\Lambda^0+\bar{\Lambda}^0$ spectrum; the K^0 spectrum is also fit reasonably well by the gaussian, but might be better fit using a distorted gaussian [33]. As will be seen in Figure 7.4, the spectrum fall-off at low ξ is consistent with contributions from $Z^0 \rightarrow$heavy-quark decays. The fitted peak centers, along with the statistical and systematic errors from

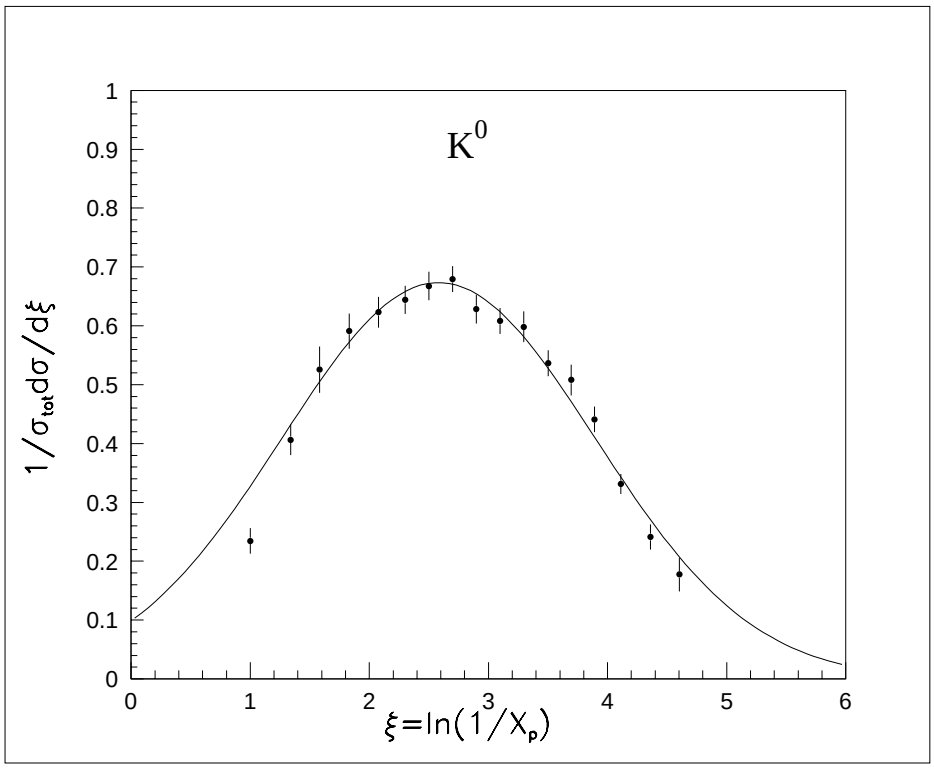

Figure 6.15: The MLLA fit to the production spectrum of K^0 in hadronic Z^0 decays.

the fits, are shown in Table 6.7. The systematics were estimated by removing data points from the "tails" of the spectrum and refitting the remaining points. For the K^0's, up to 4 data points on each side of the peak were removed, for a total of 20 different fit variations; for the $\Lambda^0+\bar{\Lambda}^0$'s, up to 3 data points were removed from each side of the distribution, for a total of 14 variations. Using these variations, an *rms* was calculated as an estimate of the systematic error. The peak value for the K^0 spectrum, $\xi^*_{K^0}$, was found to be 2.64 ± 0.06, while that for the $\Lambda^0+\bar{\Lambda}^0$ spectrum was found to be 2.63 ± 0.06. Within the accuracy of this measurement, no mass dependence is observed. Figure 6.17 shows measurements of numerous particles at the Z^0 energy; these SLD measurements are in good agreement with the other results. An approximate mass dependence is observed when considering just the baryons or just the mesons, but no overall mass dependence seems to exist for the entire set of measurements. Figure 6.18 shows the peak position values for $K^{\pm}$, K^0, and $\Lambda^0/\bar{\Lambda}^0$ for various experiments from $\sqrt{s} = 10\ GeV$ to these measurements at the Z^0 pole. A logarithmic dependence on energy is clearly visible, which is consistent with QCD predictions.

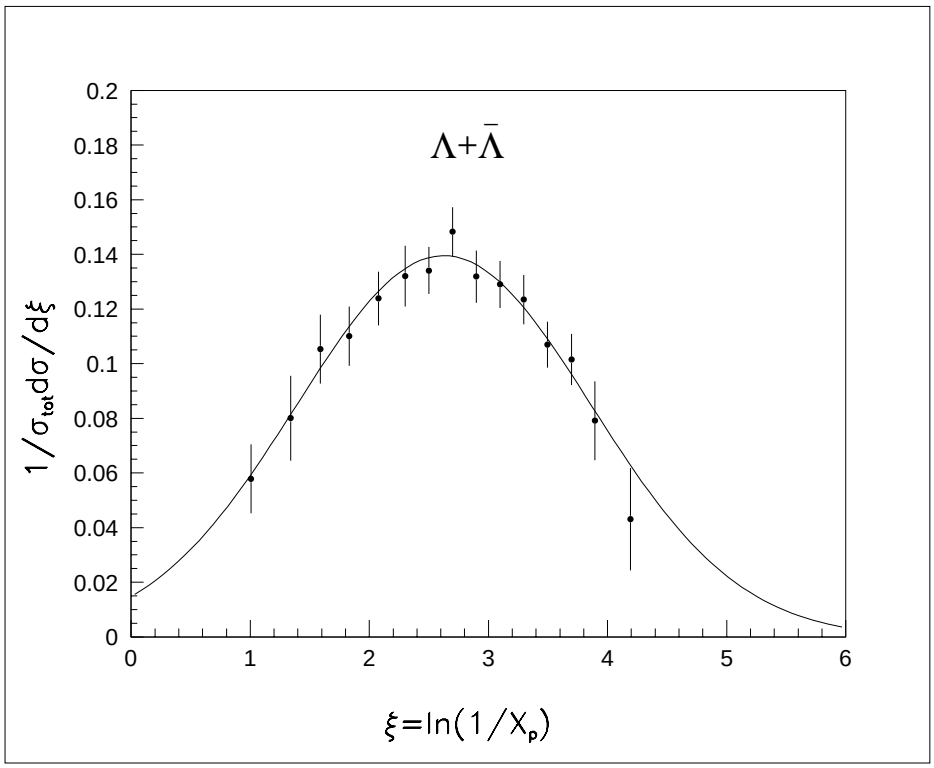

Figure 6.16: The MLLA fit to the production spectrum of $\Lambda^0\,(+\bar{\Lambda}^0)$ in hadronic Z^0 decays.

Particle	$Center \pm (stat.) \pm (rms)$	χ^2/dof
K_s^0	$2.639 \pm 0.024 \pm 0.055$	16.5/13
$\Lambda^0+\bar{\Lambda}^0$	$2.626 \pm 0.057 \pm 0.022$	3.4/11

Table 6.7: The fitted gaussian centers for the K^0 and the Λ^0 spectra, and the quality of the fit when using all of the data points.

As discussed in chapter 2, an important caveat must be considered when comparing the results to the MLLA predictions: the LPHD assumption "ties" the parton spectrum to the *primary* hadron spectrum. The primary hadron spectrum (for a given species) is modified by particles from resonance decays and particles from heavy meson/baryon decays. There are three ways to approach this: 1) measure all decay modes to a very high precision, 2) perform (large, and highly uncertain) MC subtraction to remove the estimated contribution from these sources [63]; or 3) attempt to make measurements on subsamples that have fewer sources of secondary particles. This third method is the approach taken in the next chapter.

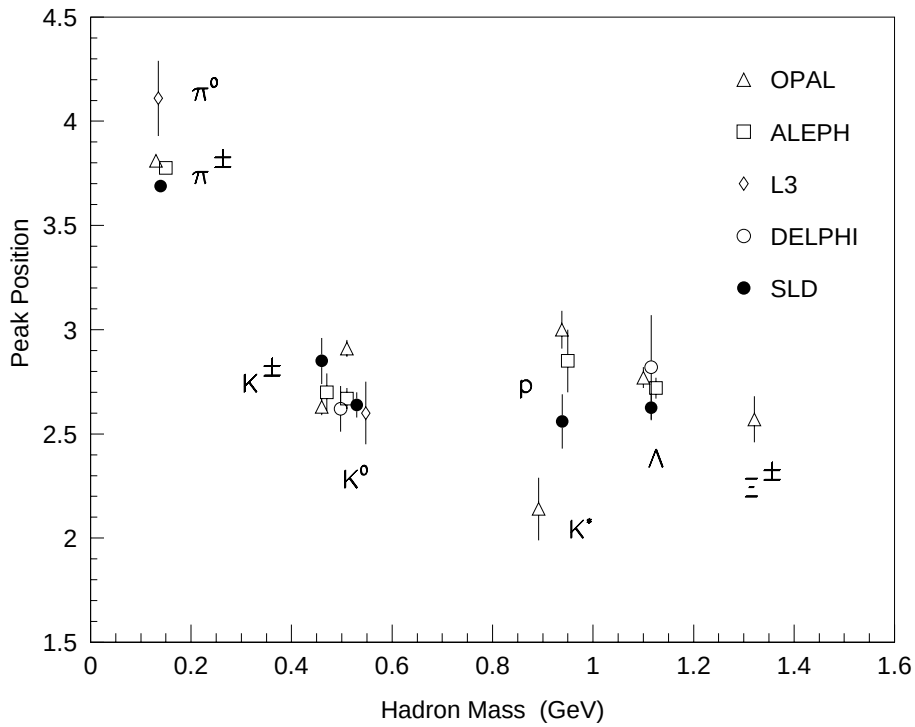

Figure 6.17: The peak positions ξ^* for different particle species measured at the Z^0 energy. In addition to the K^0 and $\Lambda^0/\bar{\Lambda}^0$ points, the preliminary SLD π, $K^{\pm}$, and $p\bar{p}$ points are also shown.

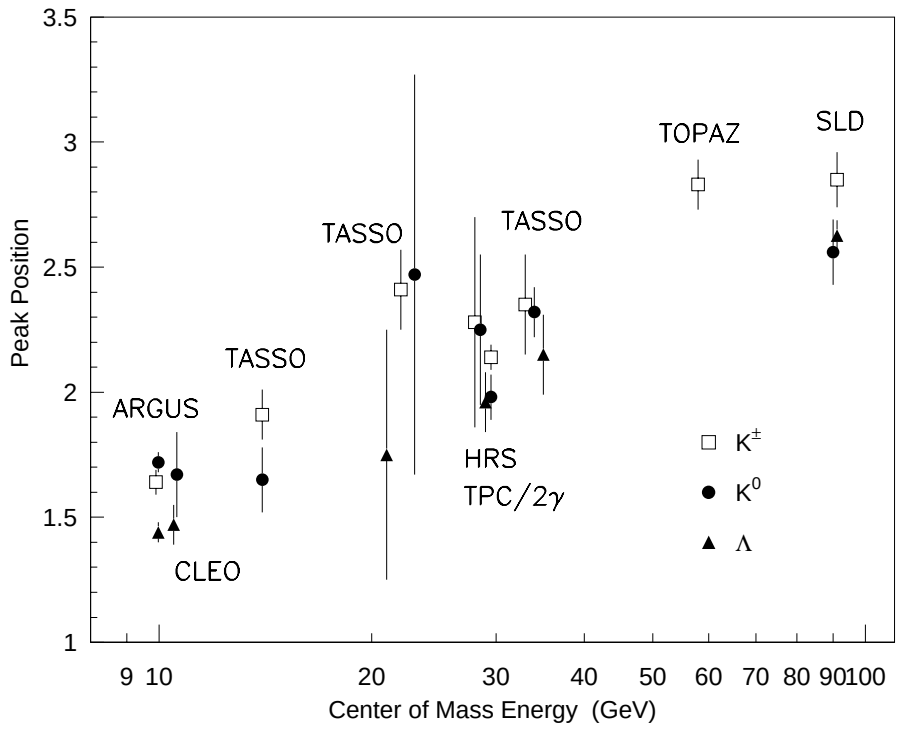

Figure 6.18: The peak positions ξ^* for $K^\pm$, K^0 and $\Lambda^0/\bar{\Lambda}^0$ measured by various experiments at different center-of-mass energies. In addition to the K^0 and $\Lambda^0/\bar{\Lambda}^0$ points, the preliminary SLD $K^\pm$ point is also shown.

Chapter 7

The Flavor and Quark-Jets Analysis

7.1 Introduction

In this chapter, the flavor tagging and quark-jet tagging techniques described in Section 5.4 are used to further explore the hadronization process. First, the analysis in the preceding chapter is applied to flavor-tagged samples, and differences in production are observed. These spectra are "unfolded" to obtain the first measurements of K^0 and $\Lambda^0+\bar{\Lambda}^0$ production in light (u, d, s), c, and b-quark events at the Z^0. Next, the quark-tagging techniques are used to examine differences in Λ^0 production for light quark and anti-quark jets, and to make the first measurements of the $q \rightarrow \Lambda^0$ and the $\bar{q} \rightarrow \Lambda^0$ fragmentation functions.

7.2 Spectra in uds, c, and b-quark Events

Using the techniques discussed in Chapter 5, the data set was divided into three flavor-enriched subsets; this resulted in a uds-enriched sample of 53526 events, a c-enriched sample of 22648 events, and a b-enriched sample of 14039 events. For each sample, the V^0 candidates were binned in ξ and the analysis described in Chapter 6 was repeated. The K_s^0 binning used was identical to that described in the previous chapter; the $\Lambda^0/\bar{\Lambda}^0$'s were binned in wider ξ-bins, which then typically required 3 gaussians to describe the peak adequately. When we treat them in the same manner as was described in the last chapter, simply correcting for the reconstruction efficiency (which to a good approximation is independent of the event flavor), we arrive at the production spectra shown in Figure 7.1. Clear differences in production among the three samples are observed. For the K^0, production is enhanced in the b-quark-enriched ($n_{sig} = 3+$)

and the c-quark-enriched ($n_{sig} = 1, 2$) samples with respect to the uds-quark-enriched ($n_{sig} = 0$) sample. For the Λ^0 ($+\bar{\Lambda}^0$) samples, a possible enhancement of the production in the c-quark-enriched ($n_{sig} = 1, 2$) sample with respect to those in the other two samples is seen. We therefore performed a complete *unfolding* of the three samples in order to obtain the production spectra for the light, c, and b quark samples.

7.2.1 The Unfolding Matrix

The expected number of particles of type X per i-tagged event n_i^e ($i = 1, 2, 3$ for $n_{sig} = 0, 1 - 2, 3+$ resp.), can be related to the true number per j-flavor event m_j^t ($j = uds$, c, b) by the three linear equations:

$$n_i^e(\xi) = \sum_j E_{ij} m_j^t(\xi), \tag{7.1}$$

where it is convenient to express the matrix

$$E_{ij} = \frac{f_j \epsilon_{ij} b_{ij}(\xi) \mathcal{R}(\xi)}{\sum_k f_k \epsilon_{ik}} \tag{7.2}$$

in terms of the V^0 reconstruction efficiency $\mathcal{R}(\xi)$ (discussed in the last chapter), the fraction of hadronic Z^0 events decaying into quark type j

$$f_j = \frac{N_{Z^0 \to j\bar{j}}}{N_{Z^0 \to all}}, \tag{7.3}$$

an event-tagging efficiency matrix

$$\epsilon_{ij} = \frac{N^r_{j \to i}}{N^r_j}, \tag{7.4}$$

where $N^r_{j \to i}$ is the number of reconstructed j-flavor events that are in the i-tagged sample and N^r_j is the total number of reconstructed j-flavor events, and a bias term

$$b_{ij}(\xi) = \frac{X^r_{j \to i}(\xi)/N^r_{j \to i}}{X^r_j(\xi)/N^r_j}. \tag{7.5}$$

Here, $X^r_{j \to i}(\xi)$ is the number of reconstructed particles of species X from quark flavor j that are found in the i-tagged sample. For the above, and all following equations, there is no implicit summation over repeated indices.

Note the definition of the Tag Purity ($\mathcal{P}_{ij}$) is related to the above matrices as follows:

$$\mathcal{P}_{ij} = \frac{f_j \epsilon_{ij}}{\sum_k f_k \epsilon_{ik}}. \tag{7.6}$$

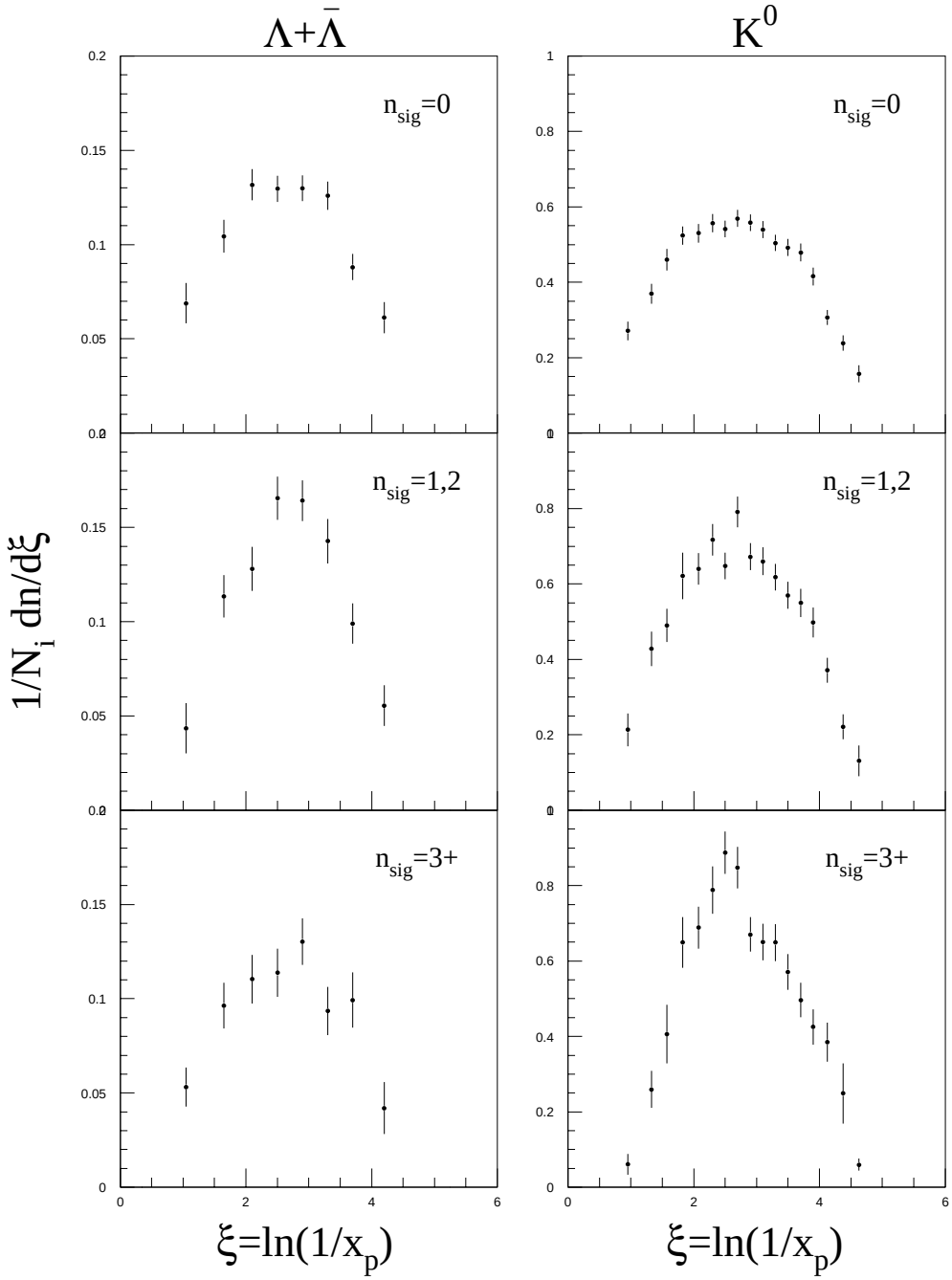

Figure 7.1: The production spectra for $\Lambda^0+\bar{\Lambda}^0$ and K^0 in the three flavor-enriched event samples. Only the statistical errors are shown.

In the absence of tagging bias ($b_{ij} = 1$), the fraction of the particles of a given species in the i-tagged sample that comes from j-flavor events would be the same as the event purities, and Equation 7.1 would be a simple relationship based upon the purities of the tag. However, the presence of K_s^0 or $\Lambda^0/\bar{\Lambda}^0$ that decay near the IP can affect the tag, so these biases must be considered carefully. Tables 7.1 and 7.2 recapitulate (respectively) the Standard Model fractions f_j, the efficiencies ϵ_{ij}, and the purities $\mathcal{P}_{ij}$ of the flavor tags.

f_{uds}	0.610
f_c	0.172
f_b	0.218

Table 7.1: The standard model production fractions for $Z^0 \to q\bar{q}$.

Tag	uds tag ϵ	c tag ϵ	b tag ϵ	$\mathcal{P}_{uds}$	$\mathcal{P}_c$	$\mathcal{P}_b$
$n_{sig} = 0$	0.844	0.440	0.076	0.848	0.125	0.027
$n_{sig} = 1,2$	0.154	0.475	0.331	0.378	0.330	0.292
$n_{sig} = 3+$	0.002	0.085	0.593	0.009	0.101	0.890

Table 7.2: Estimated tagging efficiencies and purities for selecting $uds-$, $c-$, and $b-$quark events using the n_{sig} tags.

Using the MC, the 3×3 bias matrices shown in Figures 7.2 and 7.3 were obtained for K^0 and $\Lambda^0/\bar{\Lambda}^0$ as a function of momentum. Simple parameterizations to these shapes were performed with the constraint that $\sum_i \epsilon_{ij} b_{ij}(\xi) = 1$. It should be noted that the diagonal terms for the bias elements are reasonably close to 1, and that the elements that show the most variation from unit value are the terms that have the lowest contributing populations (i.e. the product $\epsilon_{ij} b_{ij}$ is small).

The general behavior of these bias matrices can be explained by a few simple effects. First, consider only light quark events (top row of Figures 7.2 and 7.3). For perfect tracking and perfect V^0 rejection in the flavor tags, all but a few events would have no significant tracks and b_{11} would be almost exactly unity. Two effects push *uds* events out of the $n_{sig} = 0$ category. The first effect is simply "miss-tracking" – multiple scattering, misassigning VXD hits to tracks, etc. The second effect is real tracks that

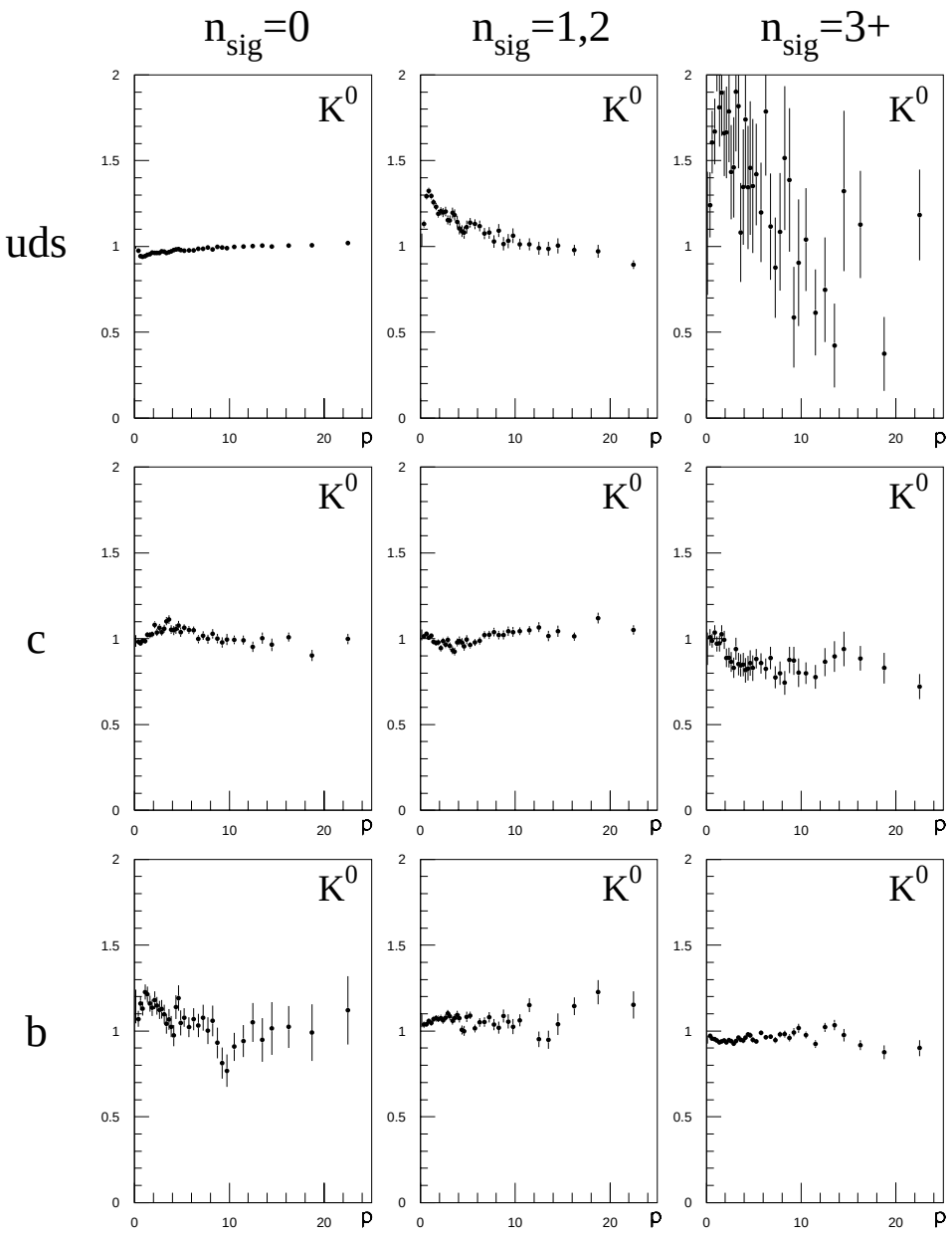

Figure 7.2: The 3×3 matrix $b_{ij}(p)$ for K^0's as a function of momentum.

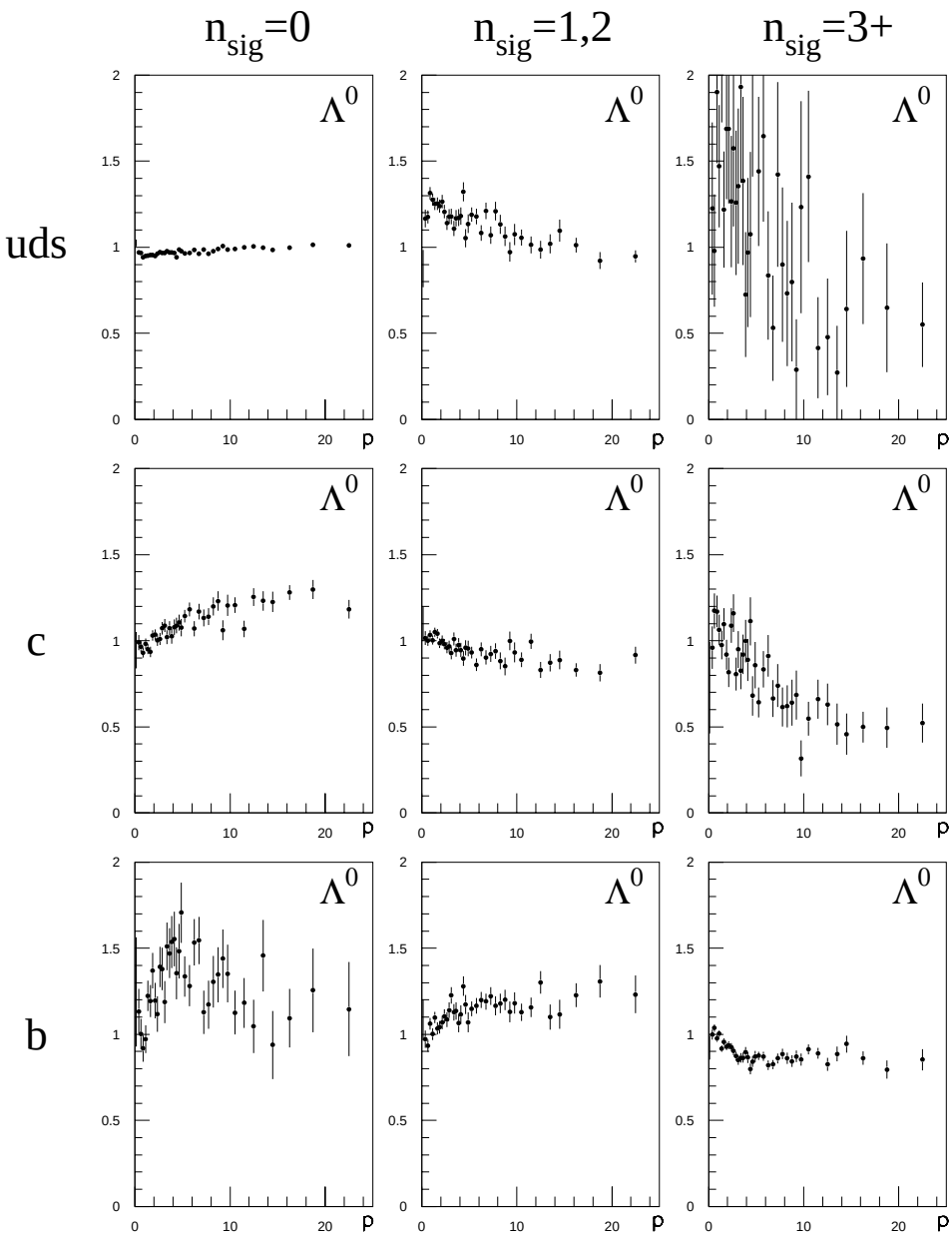

Figure 7.3: The 3×3 matrix $b_{ij}(p)$ for $\Lambda^0/\bar{\Lambda}^0$'s as a function of momentum.

are significantly separated from the IP, such as charged tracks from γ-conversions, nuclear interactions, and decays of strange particles (mostly V^0's). Especially for low-momentum V^0's, it is possible to "lose" or miss-reconstruct one of the two charged tracks. The result of this is that the V^0 contributes a significant track. Both of these effects favor events containing low momentum V^0's. The direct effect of a V^0 contributing a significant track and the indirect effect due to the fact that events tend to have several low-momentum particles (which are more-likely to be miss-tracked), contribute about equally to pushing the value of b_{11} below 1, and thus pushing b_{12}, $b_{13} > 1$. High momentum V^0 have little effect on the tag since they typically decay far from the IP. Also, events with high-momentum V^0's tend to have fewer low momentum tracks and thus b_{11} becomes greater than 1 as momentum increases.

The situation becomes more complicated for heavy-quark events. Two additional effects have to be considered: 1) tracks from heavy hadron decays with real significant separation; 2) different production rates for $\Lambda^0/\bar{\Lambda}^0$'s and K^0's in heavy particle decays (thus, one might no longer expect to see the same features in the two figures). Consider K^0's from b-quark events (bottom row of Figure 7.2). The production of K^0 above ~ 3 GeV/c is dominated by K^0 production from B-hadron decays. These higher momentum K^0's tend not to participate in the tag, as they are either reconstructed or ignored if they decay outside the VXD. Thus, when a B-hadron decays into K^0 (plus other tracks) rather than a $K^{\pm}$, this effectively loses one track that could have been used to tag the event. This causes b_{33} to be below 1 in this region, and b_{32} and b_{31} are correspondingly greater than 1. One would expect this effect to be greater for $\Lambda^0/\bar{\Lambda}^0$ by phase-space arguments: the creation of the higher-mass Λ^0 reduces the overall multiplicity of the decay. At lower V^0 momentum fragmentation becomes the dominant source, and one thus expects behavior tending toward that observed in the top row.

The effect of V^0's from decays of charmed hadrons is similar to that of B-hadron decays, except that charmed hadrons are of lower mass, and tend to produce fewer tracks in their decays. The matrix element b_{23} is therefore reduced at high-momentum by a larger amount than b_{33}. The case of $\Lambda^0/\bar{\Lambda}^0$'s in charmed events is particularly simple:

all "direct" $\Lambda^0/\bar{\Lambda}^0$'s are from charmed baryons[1] which contribute very few other charged tracks with which to tag. Thus, b_{22} is also below 1, and b_{21} is constrained to be greater than 1.

For each bin of ξ, the observed population of each of the three tag-type events is $n_i^o(\xi)$ with statistical error $\sigma_i^o(\xi)$. By inverting Equation 7.1, the "unfolded" spectra are

$$m_j^t(\xi) = \sum_i E_{ij}^{-1} n_i^e(\xi) \tag{7.7}$$

with errors

$$\sigma_j^t(\xi) = (\Sigma_i E_{ij}^{-1} \sigma_j^2)^{\frac{1}{2}}. \tag{7.8}$$

The unfolded spectra are shown in Figure 7.4, and listed in Tables 7.3 and 7.4. In order to compare among flavors, we only show the combination of the statistical error and the systematic error due to the unfolding procedure; neither the point-to-point systematics nor correlated systematics are shown. The error bars are dominated by statistics. The large errors on the $c-$quark spectra are almost entirely statistical, and are due to the high level of impurities in the $n_{sig} = 1, 2$ sample.

The unfolding procedure is subject to uncertainties in the input parameters (Eqns. 7.1-7.5). MC simulation indicated (within MC statistics) that the reconstruction efficiency $\mathcal{R}(\xi)$ was the same for all three flavors. The uncertainties in the world average values of the standard model fractions f_i are negligible with respect to the statistical errors. The errors on the 2-d impact parameter tagging efficiency have been studied by [11]; a conservative variation of ± 0.01 was applied to each term of the efficiency matrix ϵ_{ij} (with the simultaneous modification of the other terms so that the constraint condition $\sum_i \epsilon_{ij} = 1$ was satisfied); this variation was also found to be negligible. The unfolding systematics are dominated by the uncertainty of the bias term. For this term, a very conservative 20% variation on the deviation of the bias term from unity was used.

When comparing the spectra produced from the different Z^0 decay modes, several features are observed. The production of K^0 in heavy quark events is larger than

[1] which typically have shorter flight distances than charmed mesons ($c\tau \sim 50\mu$m, vs. $c\tau \sim 125 - 350\mu$m).

in light-quark events, which is expected due to weak decays of heavy hadrons. The K^0 production spectrum cuts off more sharply at low-ξ (high momentum) in $b-$quark events than in light-quark events or c events, which is expected due to the high average multiplicity of B-hadron decays. For the three $\Lambda^0\,(+\bar{\Lambda}^0)$ spectra, we observe essentially the same level of production for the three Z^0 decay modes. Within the level of our statistics, no clear spectra shape differences are observed.

The "SLD-tuned" MC reproduces the relative production rates for K^0 from the three Z^0 decay modes, and the relative "cut-offs" at high momentum (low ξ). The K^0 MC excess at high ξ is similar for all three flavors and for the global sample (Figure 6.13). For the $\Lambda^0\,(+\bar{\Lambda}^0)$ the MC describes the shapes of all flavors within the measurement errors. The $\Lambda^0\,(+\bar{\Lambda}^0)$ MC normalization appears reasonable for the for the $uds-$ and $c-$quark samples. The $\Lambda^0\,(+\bar{\Lambda}^0)$ MC normalization is approximately 30% low for the $b-$quark sample[2]. The integrated production rates for the three quark samples are listed in Table 7.5.

For MLLA comparisons, the two uds spectra are fitted with gaussians; satisfactory fits are obtained. The peak centers, errors, and fit quality are listed in Table 7.6. A significant peak difference is still not observed between the $\Lambda^0\,(+\bar{\Lambda}^0)$ sample and the K^0 sample, although the $\Lambda^0\,(+\bar{\Lambda}^0)$ sample is clearly in need of more statistics. When comparing the peak positions for the global K^0 sample and the uds K^0 sample, an upward shift of approximately 1σ in the uds sample is observed. A gaussian fit was made to all of the data points in the b-quark K^0 sample; the fit quality was poor ($\chi^2/dof = 27.9/13$). When fitting to a limited region around the peak ($1.45 \leq \xi \leq 3.80$), a satisfactory fit was obtained ($\chi^2/dof = 9.78/7$), yielding a peak position of $\xi^* = 2.62 \pm .06(stat.) \pm .05(syst.)$.

In summary, we see that spectrum shape for K^0's from the b-quark sample is different from that of the uds-quark sample, and is not describable by a single gaussian. Similar conclusions are expected for the $\Lambda^0/\bar{\Lambda}^0$'s from the b-quark sample, and both the K^0

[2]This is consistent with the level of uncertainty from recent B baryon production fraction measurements. For example, DELPHI recently reported a B baryon fraction of $.116 \pm .033$ in $Z^0 \rightarrow b\bar{b}$ events [64]

and the $\Lambda^0/\bar{\Lambda}^0$'s from the c-quark sample, but the statistics are clearly not sufficient to draw conclusions. It also appears that the presence of the b, c-quark contribution to the global sample does not greatly affect the peak position.

ξ range	uds-quark		c-quark		b-quark	
	$\frac{1}{\sigma_{tot}}\frac{d\sigma}{d\xi}$ ($\pm stat.$)	unfold syst.	$\frac{1}{\sigma_{tot}}\frac{d\sigma}{d\xi}$ ($\pm stat.$)	unfold syst.	$\frac{1}{\sigma_{tot}}\frac{d\sigma}{d\xi}$ ($\pm stat.$)	unfold syst.
0.70-1.20	0.270 ± 0.039	0.002	0.309 ± 0.175	0.008	0.038 ± 0.039	0.001
1.20-1.45	0.324 ± 0.043	0.003	0.697 ± 0.191	0.014	0.231 ± 0.065	0.004
1.45-1.70	0.449 ± 0.045	0.005	0.557 ± 0.201	0.021	0.412 ± 0.100	0.005
1.70-1.95	0.512 ± 0.049	0.006	0.602 ± 0.263	0.029	0.689 ± 0.088	0.007
1.95-2.20	0.524 ± 0.043	0.006	0.579 ± 0.186	0.031	0.737 ± 0.072	0.008
2.20-2.40	0.535 ± 0.044	0.006	0.701 ± 0.197	0.035	0.839 ± 0.081	0.011
2.40-2.60	0.582 ± 0.042	0.011	0.247 ± 0.181	0.060	1.012 ± 0.074	0.017
2.60-2.80	0.521 ± 0.045	0.009	0.863 ± 0.207	0.049	0.911 ± 0.075	0.015
2.80-3.00	0.558 ± 0.043	0.011	0.600 ± 0.185	0.053	0.729 ± 0.064	0.013
3.00-3.20	0.540 ± 0.044	0.011	0.596 ± 0.191	0.054	0.704 ± 0.068	0.012
3.20-3.40	0.520 ± 0.042	0.011	0.472 ± 0.182	0.054	0.713 ± 0.068	0.012
3.40-3.60	0.524 ± 0.042	0.012	0.388 ± 0.180	0.054	0.626 ± 0.066	0.011
3.60-3.80	0.507 ± 0.044	0.012	0.431 ± 0.185	0.053	0.529 ± 0.064	0.010
3.80-4.00	0.429 ± 0.045	0.010	0.461 ± 0.192	0.046	0.440 ± 0.066	0.008
4.00-4.25	0.331 ± 0.037	0.008	0.239 ± 0.165	0.037	0.418 ± 0.071	0.007
4.25-4.50	0.293 ± 0.040	0.007	$-.040 \pm 0.187$	0.030	0.291 ± 0.108	0.005
4.50-4.75	0.187 ± 0.043	0.005	0.055 ± 0.183	0.019	0.059 ± 0.030	0.002

Table 7.3: The unfolded production cross-sections for K^0, with the systematics due to unfolding. The point-to-point systematics and the correlated systematics are the same as in Table 6.3.

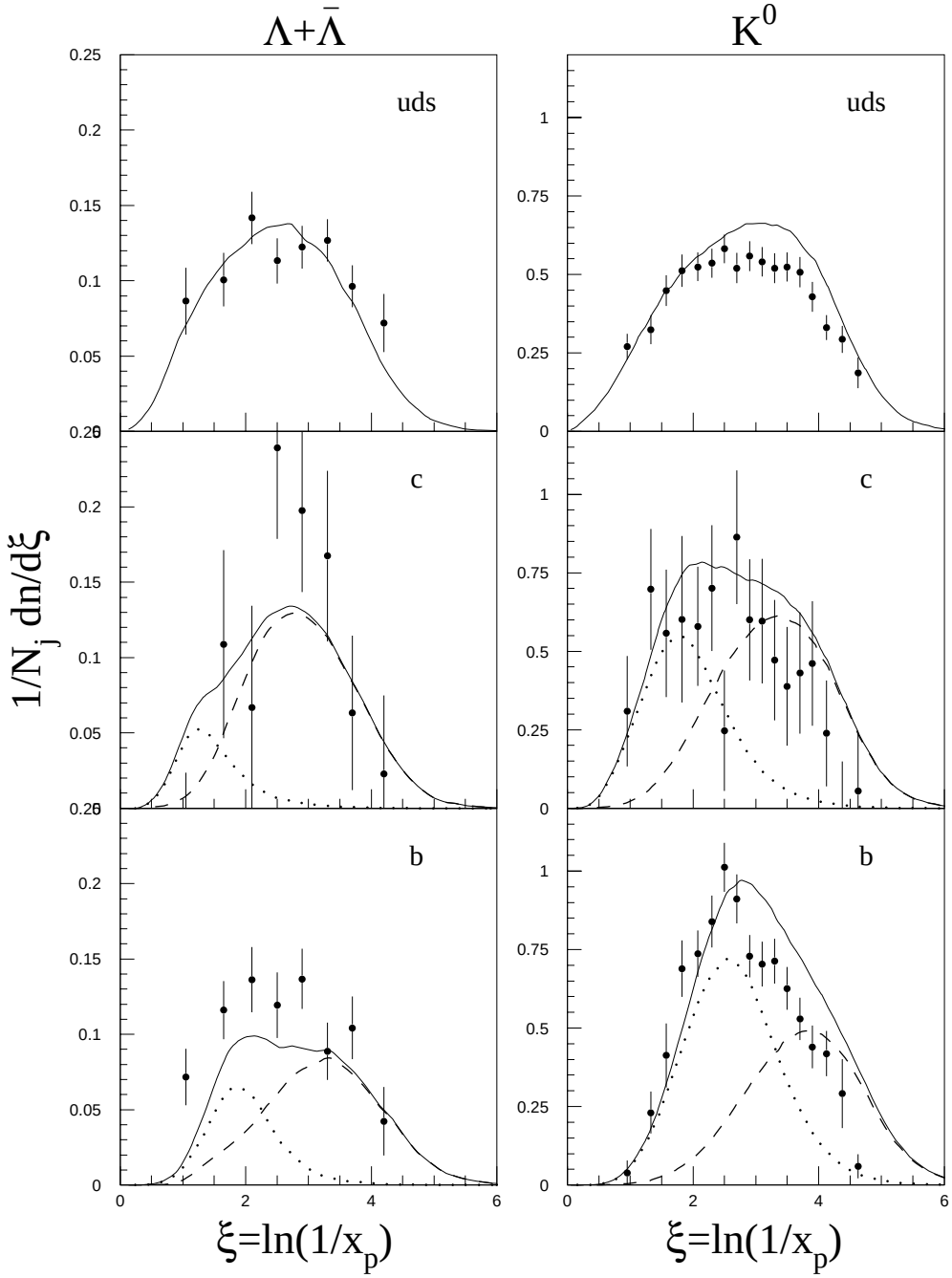

Figure 7.4: The fully-unfolded production spectra for $\Lambda^0+\bar{\Lambda}^0$ and K^0. Shown are the statistical errors and the independent point-to-point systematics. Correlated systematics and systematics that are common to a data bin in all three species' plots are not shown. The overlaid curves are from the "SLD-tuned" JETSET 7.4. For the heavy quark events, the dotted lines indicate the contributions from heavy hadron decays, the dashed lines indicate the contributions from fragmentation.

ξ range	uds-quark		c-quark		b-quark	
	$\frac{1}{\sigma_{tot}}\frac{d\sigma}{d\xi}$ ($\pm stat.$)	unfold syst.	$\frac{1}{\sigma_{tot}}\frac{d\sigma}{d\xi}$ ($\pm stat.$)	unfold syst.	$\frac{1}{\sigma_{tot}}\frac{d\sigma}{d\xi}$ ($\pm stat.$)	unfold syst.
0.70-1.40	0.086 ± 0.019	0.001	$-.047 \pm 0.069$	0.007	0.072 ± 0.015	0.002
1.40-1.90	0.101 ± 0.016	0.002	0.109 ± 0.061	0.009	0.116 ± 0.017	0.004
1.90-2.30	0.142 ± 0.016	0.003	0.067 ± 0.065	0.016	0.136 ± 0.020	0.005
2.30-2.70	0.113 ± 0.013	0.002	0.239 ± 0.059	0.011	0.119 ± 0.020	0.005
2.70-3.10	0.122 ± 0.012	0.002	0.197 ± 0.052	0.012	0.137 ± 0.018	0.005
3.10-3.50	0.127 ± 0.013	0.003	0.167 ± 0.055	0.011	0.089 ± 0.018	0.002
3.50-3.90	0.096 ± 0.012	0.002	0.063 ± 0.050	0.009	0.104 ± 0.019	0.002
3.90-4.50	0.072 ± 0.013	0.002	0.023 ± 0.050	0.006	0.042 ± 0.018	0.001

Table 7.4: The unfolded production cross-sections for $\Lambda^0+\bar{\Lambda}^0$, with the systematics due to unfolding.

Quark Sample	K^0 ($.7 \leq \xi \leq 4.75$)	$\Lambda^0+\bar{\Lambda}^0$ ($.7 \leq \xi \leq 4.5$)
uds	$1.733 \pm 0.043 \pm 0.011$	$.394 \pm 0.021 \pm 0.012$
c	$1.779 \pm 0.194 \pm 0.037$	$.329 \pm 0.082 \pm 0.017$
b	$2.029 \pm 0.070 \pm 0.012$	$.368 \pm 0.024 \pm 0.013$

Table 7.5: The production rates for K^0 and $\Lambda^0+\bar{\Lambda}^0$ (per event) in the three quark samples. The systematic errors shown including the point-to-point systematics and the unfolding systematics. Not shown are the overall normalization (correlated error) of 3.4% for the $\Lambda^0+\bar{\Lambda}^0$ and 3.7% for the K^0.

Particle	$Center \pm (stat.) \pm (syst.)$	χ^2/dof
K^0 (uds)	$2.711 \pm 0.060 \pm 0.042$	6.3/13
$\Lambda^0+\bar{\Lambda}^0$ (uds)	$2.556 \pm 0.186 \pm 0.020$	3.2/4

Table 7.6: The fitted gaussian centers for the K^0 and the $\Lambda^0+\bar{\Lambda}^0$ spectra from $Z^0 \rightarrow q\bar{q}$ ($q = u, d, s$) events.

7.3 Λ^0 Production in Quark and Antiquark Jets

In this section the quark-tagging techniques are used to make preliminary measurements of the quark and anti-quark fragmentation functions into the Λ^0 baryon. A comparison of the two production rates as a function of momentum lends evidence for the "leading-particle" production hypothesis.

7.3.1 $\Lambda^0/\bar{\Lambda}^0$'s in Enriched Samples, and the Unfolding Procedure.

Samples of hemispheres enriched in primary light ($n_{sig} = 0$) q and $\bar{q}$ jets were obtained using the techniques described in Chapter 5. The V^0 selection techniques were applied to both samples, considering only the $\Lambda^0/\bar{\Lambda}^0$ hypothesis. The Λ^0 candidates in the q-tagged sample and the $\bar{\Lambda}^0$ candidates in the $\bar{q}$-tagged sample were combined into a "$q \to \Lambda^0$" sample. The Λ^0 candidates in the $\bar{q}$-tagged sample and the $\bar{\Lambda}^0$ candidates in the q-tagged sample were combined into a "$\bar{q} \to \Lambda^0$" sample. These samples consisted of 33510 V^0 candidates and 33636 V^0 candidates, respectively.

For each sample, the V^0 candidates were binned in $x_p = p_{V^0}/p_{beam}$ and the mass peaks were fitted. Due to the sparcity of the data, very wide bins were used, and 3 gaussians were typically required to describe the peak adequately. The procedure described in Chapter 5 was modified as follows: for each momentum bin, the mass distributions for the $q \to \Lambda^0$ and $\bar{q} \to \Lambda^0$ data samples were fitted with a common peak center and width, which were determined by fitting the sum of the two samples. The results are listed in Tables 7.7 and 7.8, including the statistical errors; the systematic errors are the same as those shown in Table 6.4, when averaged to account for the differences in bin widths. Using the "SLD-tuned" JETSET 7.4 MC with detector simulation, the contributions to these spectra from heavy quark contamination were estimated[3]; a conservative systematic uncertainty of 25% was applied. This contribution was subtracted, and the two spectra were "unfolded" for the purity of the tag, which was calculated to be $71.6 \pm 1.0\%$ (see Figure 5.10). Tables 7.7 and 7.8 also list the

[3]We estimate the fraction of "heavy quark" V^0 contamination to be the same as the fraction of heavy quark contamination in the uds-tagged sample: $\sim 12.5\%$ from c-quark decays and $\sim 2.7\%$ from b-quark decays.

estimated number from heavy quark decays, the subtracted values, and finally the "unfolded" values.

x_p bin	Raw Data ($\pm stat.$)	Est. HQ Contrib.	Subtracted Value	Unfolded Value
0.01-0.02	28.3± 6.7	3.4± 2.2	24.9± 7.1	16.6± 13.1
0.02-0.03	89.0±10.2	11.1± 4.4	77.9±11.1	75.2± 20.0
0.03-0.05	164.3±14.0	20.9± 7.0	143.4±15.6	148.9± 28.0
0.05-0.07	507.0±36.3	63.0±17.7	444.0±40.3	453.3± 72.8
0.07-0.10	560.5±37.1	88.8±24.1	471.7±44.2	431.7± 80.2
0.10-0.15	535.4±37.9	64.7±18.1	470.7±42.0	499.9± 76.2
0.15-0.18	388.3±43.8	51.3±14.7	337.0±46.2	410.8± 82.0
0.18-0.30	577.7±57.1	61.1±17.2	516.6±59.6	598.6±109.7
0.30-1.00	402.1±47.3	41.3±12.2	360.8±48.9	473.6± 90.0

Table 7.7: The data for the $q \to \Lambda^0$ tagged sample, the estimated contribution due to heavy baryon decays, the data values after the MC subtraction, and the final values after purity unfolding.

x_p bin	raw data ($\pm stat.$)	Est. HQ Contrib.	Subtracted Value	Unfolded Value
0.01-0.02	46.9± 8.1	9.3± 3.9	37.6± 9.0	45.9± 15.6
0.02-0.03	98.0±10.3	16.0± 5.7	82.0±11.8	84.7± 20.9
0.03-0.05	164.5±13.3	29.6± 9.2	134.9±16.2	129.4± 28.8
0.05-0.07	520.3±36.2	90.6±24.6	429.7±43.8	420.4± 77.2
0.07-0.10	645.2±39.1	112.5±30.1	532.7±49.4	572.7± 86.8
0.10-0.15	528.3±38.4	102.0±27.4	426.3±47.2	397.1± 83.0
0.15-0.18	270.6±42.3	45.8±13.3	224.8±44.3	150.9± 79.5
0.18-0.30	489.9±67.6	98.0±26.4	391.9±72.5	309.9±126.5
0.30-1.00	217.6±59.0	28.4± 8.9	189.2±59.6	76.4±103.9

Table 7.8: The data for the $\bar{q} \to \Lambda^0$ tagged sample, the estimated contribution due to heavy baryon decays, the data values after the MC subtraction, and the final values after purity unfolding.

The spectra for the two samples at each stage of the analysis were used to form a "Lambda Baryon Production Asymmetry", herein referred to as A_{Λ^0}. This quantity is defined for each x_p bin as

$$A_{\Lambda^0}(x_p) = \frac{N_{q\to\Lambda^0}(x_p) - N_{\bar{q}\to\Lambda^0}(x_p)}{N_{q\to\Lambda^0}(x_p) + N_{\bar{q}\to\Lambda^0}(x_p)}. \tag{7.9}$$

Figure 7.5 and Table 7.9 show this asymmetry for the the tagged samples, after the

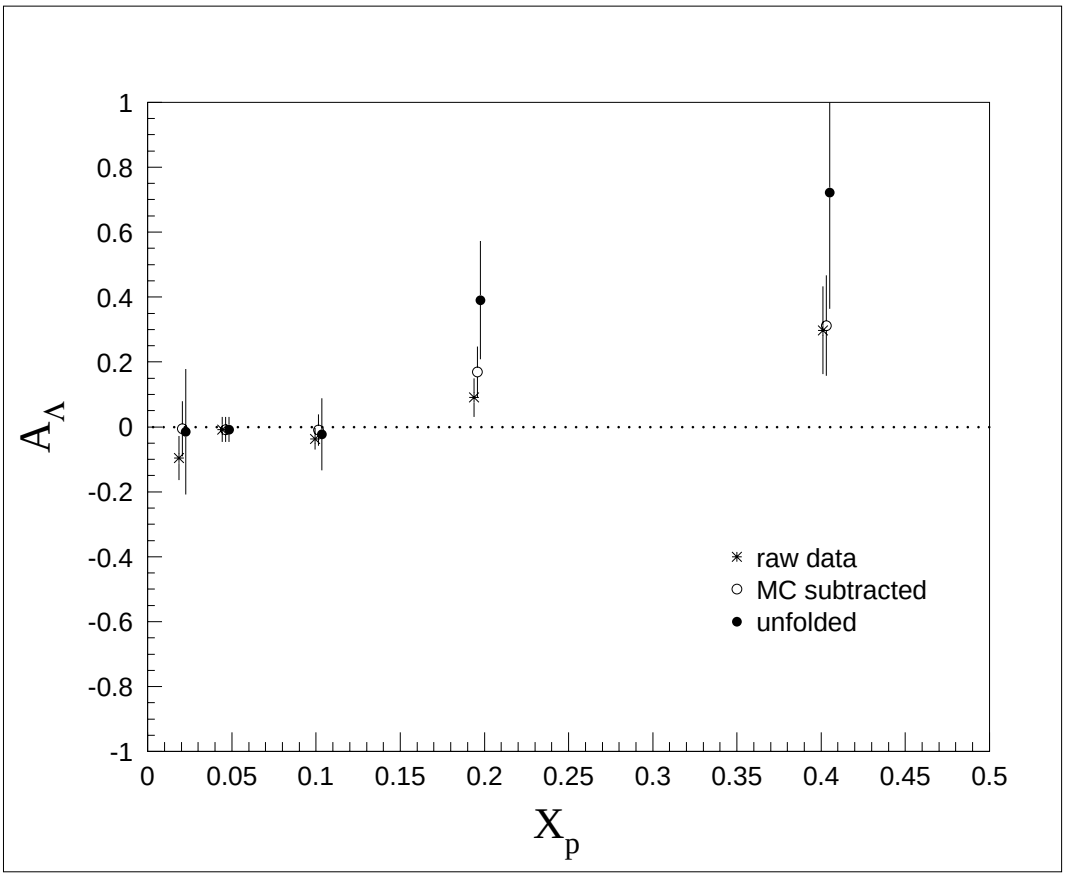

Figure 7.5: The Lambda Baryon Production Asymmetry as a function of x_p before and after corrections. The data have been rebinned and the data points have been staggered for clarity. The common systematic errors are not shown.

subtraction of the heavy quark contribution, and finally after correcting for sample purity (the correction for purity amounts to a scaling of the data and errors by an amount $1/(2p-1)$, where p is the purity of the tag). A clear deviation away from 0 at high x_p is observed, reflecting differing production rates in the two samples. This may be interpreted as evidence for "Leading Particle" production in light quark jets - i.e. that particles at very high momentum contain the primary quark produced by the $Z^0 \rightarrow q\bar{q}$ decay. The asymmetry is due to the fact that a primary anti-quark be contained in a leading $\bar{\Lambda}^0$, but not a Λ^0, and vice-versa.

The unfolded spectra from Tables 7.7 and 7.8 were corrected for detector acceptance, and the resulting spectra for Λ^0's produced in q and $\bar{q}$ jets are shown in Figure 7.6 and Table 7.10. We see that the production is approximately equal at low momentum, but deviating at high momentum. The production of Λ^0 in $\bar{q}$ jets is consistent with zero at

x_p bin	A_{Λ^0}		
	Raw Data	MC Sub.	Unfolded
0.01-0.02	-0.247±0.138	-0.202±0.178	-0.468±0.412
0.02-0.03	-0.048±0.078	-0.026±0.101	-0.059±0.235
0.03-0.05	-0.001±0.059	0.030±0.081	0.070±0.188
0.05-0.07	-0.013±0.050	0.016±0.068	0.038±0.158
0.07-0.10	-0.070±0.045	-0.061±0.066	-0.140±0.152
0.10-0.15	0.007±0.051	0.050±0.071	0.115±0.164
0.15-0.18	0.179±0.093	0.200±0.115	0.463±0.267
0.18-0.30	0.082±0.084	0.137±0.107	0.318±0.248
0.30-1.00	0.298±0.135	0.312±0.155	0.722±0.358

Table 7.9: The Baryon Production Asymmetries for the raw data, after MC subtraction of the heavy quark contributions, and after unfolding for tag purity.

very high momenta.

x_p bin	$q \to \Lambda^0$ $\frac{1}{\sigma_{tot}}\frac{d\sigma}{dx_p} \pm (stat.)$	$\bar{q} \to \Lambda^0$ $\frac{1}{\sigma_{tot}}\frac{d\sigma}{dx_p} \pm (stat.)$	common sys.
0.01-0.02	0.514 ± 0.407	1.420 ± 0.481	± 0.018
0.02-0.03	0.895 ± 0.238	1.007 ± 0.248	± 0.009
0.03-0.05	0.706 ± 0.133	0.614 ± 0.136	± 0.006
0.05-0.07	1.205 ± 0.193	1.117 ± 0.205	± 0.006
0.07-0.10	0.762 ± 0.142	1.011 ± 0.153	± 0.006
0.10-0.15	0.724 ± 0.110	0.575 ± 0.120	± 0.007
0.15-0.18	1.138 ± 0.227	0.418 ± 0.220	± 0.007
0.18-0.30	0.648 ± 0.119	0.335 ± 0.137	± 0.010
0.30-1.00	0.193 ± 0.037	0.031 ± 0.042	± 0.010

Table 7.10: The production cross-sections for Λ^0 in quark and antiquark jets.

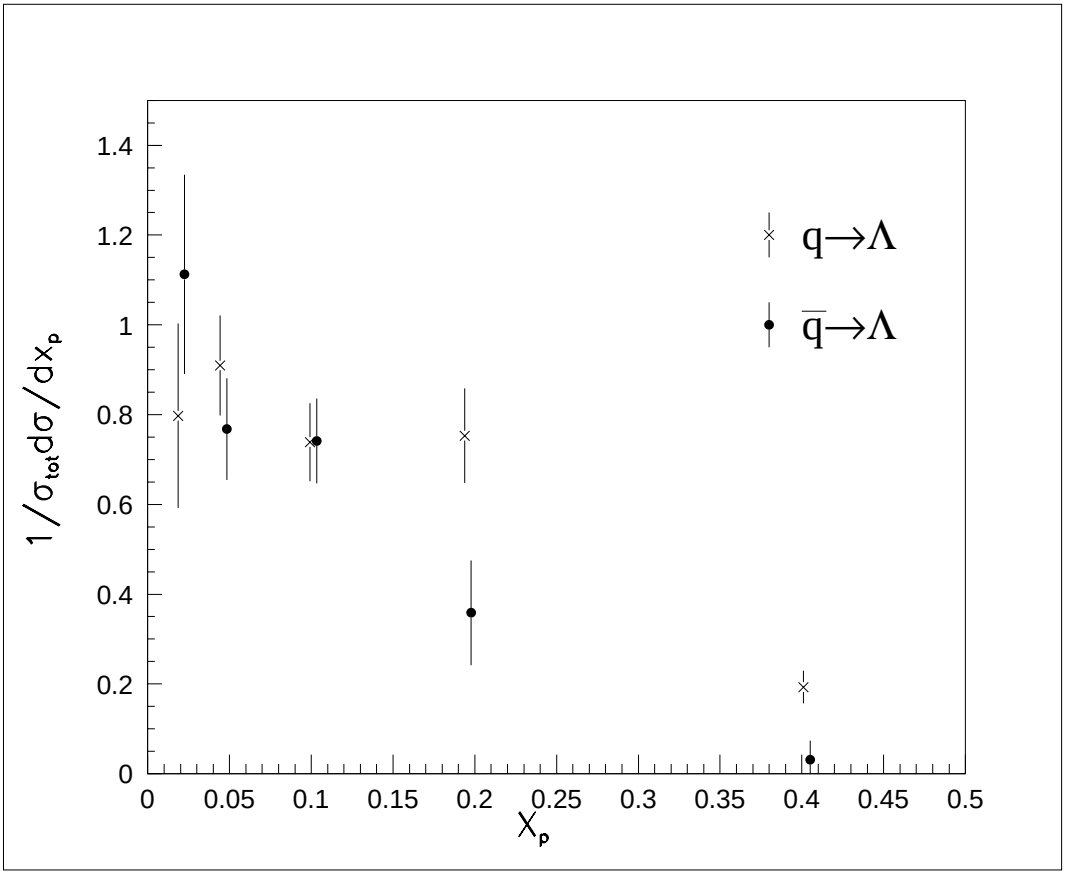

Figure 7.6: The production of Λ^0 in quark and antiquark jets. The data have been rebinned and the data points have been staggered for clarity. The common systematic errors are not shown.

Chapter 8

Summary of Results

In this dissertation, we have presented a measurement of the production of the strange meson K^0 and the strange baryon $\Lambda^0/\bar{\Lambda}^0$ in hadronic Z^0 decays collected by the SLC Large Detector (SLD). The analysis is based upon the approximately 150,000 hadronic events obtained in runs of the SLAC Linear Collider (SLC) between 1993 and 1995. The two particles were isolated using their characteristic long lifetimes and decay modes into two charged particles. We measured their production rates and spectra in the global event sample, and made comparisons with other experiments. We expanded this analysis to study the production dependences on primary quark flavor, and made comparisons of Λ^0 production in light (uds) quark and anti-quark jets.

In our "global" event sample, we selected V^0 candidates by first combining oppositely charged pairs of tracks and then applying selection criteria in order to improve the signal-to-background ratio. The invariant mass of the V^0 was calculated ($M_{p\pi}$ for the $\Lambda^0/\bar{\Lambda}^0$ candidates and $M_{\pi\pi}$ for the K_s^0 candidates) and the invariant-mass distributions were fit to obtain the areas under the signal peaks. Using Monte Carlo generated events with a detailed detector simulation, the reconstruction efficiencies for the V^0 candidates were calculated. Combining this information, the production spectra for $\Lambda^0+\bar{\Lambda}^0$ and K^0 ($2\times$ the K_s^0 production spectrum) were obtained. The measured spectra are in agreement with measurements performed by other experiments at the same center-of-mass energy. Comparisons of the spectra to QCD predictions were made; within the measurement errors no disagreements were observed. The predictions by the JETSET event generator, a popular model of hadron formation, are too high for K^0 production at low momenta (below 2.5 GeV/c), but are adequate for higher momenta. The predicted $\Lambda^0+\bar{\Lambda}^0$ spectrum is consistent with our measurements. The generator-level

MC was used to estimate the unmeasured fraction of each spectrum, and with this information the total integrated production rates were obtained. The results are:

$$2.00 \pm 0.07 \quad K^0 \quad \text{per hadronic } Z^0 \text{ decay, and}$$

$$0.39 \pm 0.02 \quad \Lambda^0 + \bar{\Lambda}^0 \quad \text{per hadronic } Z^0 \text{ decay,}$$

which are in good agreement with the average of the LEP measurements: 2.03 ± 0.04 for the K^0, and 0.37 ± 0.01 for the $\Lambda^0 + \bar{\Lambda}^0$. The dominant source of our error is a $\sim 4\%$ normalization error due to our uncertainty of the track reconstruction efficiency. As a cross-check of our procedures, the lifetimes of the K_s^0 and $\Lambda^0/\bar{\Lambda}^0$ were measured, and found to be consistent with world-average values.

By utilizing two important features of the SLC/SLD, namely SLD's precision CCD vertex detector and the very small and stable beam spots of the SLC, the hadronic data sample was divided into high-purity samples of "light" (uds) and "b" ($b\bar{b}$) events, and a lower-purity sample of "c" ($c\bar{c}$) events. The V^0 analysis was repeated for each sample, and differences in the spectra were observed. An unfolding procedure was applied to obtain the first measurement of K^0 and $\Lambda^0 + \bar{\Lambda}^0$ production rates and spectra in $Z^0 \to light$, $Z^0 \to c\bar{c}$, and $Z^0 \to b\bar{b}$ events. Differences in K^0 production are observed among the three flavors, in both spectrum shape and integrated rate. This is expected, as heavy quarks fragment into fast heavy hadrons, which then decay weakly into a large number of particles including strange particles. Within measurement errors, we see no differences in $\Lambda^0 + \bar{\Lambda}^0$ production among the three flavor samples. The integrated production rates per flavor event (over the measured momentum region) for the K^0 and $\Lambda^0 + \bar{\Lambda}^0$ are:

Quark Sample	K^0 $(0.4 \leq p \leq 22.6\, GeV/c)$	$\Lambda^0 + \bar{\Lambda}^0$ $(0.5 \leq p \leq 22.6\, GeV/c)$
uds	1.73 ± 0.04	$.39 \pm 0.02$
c	1.78 ± 0.20	$.33 \pm 0.08$
b	2.03 ± 0.07	$.37 \pm 0.03$

where the common normalization uncertainty of $\sim 4\%$ is not included in the errors. The K^0 and Λ^0 spectra in light events are consistent with QCD predictions, and are

not appreciably different from those in the global sample. Thus, it appears that in the global sample, the modifications of the spectra due to the heavy quark component are small.

Lastly, by utilizing the highly-polarized electron beam produced by SLC (average polarization of 72.3% for the 1993-95 physics runs), we examine for the first time Λ^0 baryon production in jets tagged as light (uds) quarks and light antiquarks. We form a Λ^0 baryon production asymmetry

$$A_{\Lambda^0}(x_p) = \frac{N_{q\to\Lambda^0}(x_p) - N_{\bar{q}\to\Lambda^0}(x_p)}{N_{q\to\Lambda^0}(x_p) + N_{\bar{q}\to\Lambda^0}(x_p)}, \tag{8.1}$$

and observe a positive asymmetry at high scaled momentum $x_p = p_{\Lambda^0}/p_{beam}$, indicating that more high-momentum Λ^0's are being produced in quark jets than in antiquark jets. Using the MC, we estimated and subtracted out a small heavy quark contribution to the spectra, which does not modify the asymmetry substantially. We then performed an unfolding to correct for the quark-jet tag purity. After this unfolding, we see that the data are consistent with all Λ^0 above $\sim$ 14 GeV/c being produced solely in quark jets. We attribute this production difference to the "leading particle" hypothesis, which suggests that the higher momentum particles are more likely to be the carriers of the primary quark. While having been observed in heavy-quark jets at the Z^0 (as heavy quarks are rarely produced in fragmentation), this is the first such observation for Z^0 decays into light quarks.

Appendix A

SLD Collaboration

K. Abe,[29] I. Abt,[14] C.J. Ahn,[26] T. Akagi,[27] N.J. Allen,[4] W.W. Ash,[27]†
D. Aston,[27] K.G. Baird,[25] C. Baltay,[33] H.R. Band,[32] M.B. Barakat,[33]
G. Baranko,[10] O. Bardon,[16] T. Barklow,[27] A.O. Bazarko,[11] R. Ben-David,[33]
A.C. Benvenuti,[2] T. Bienz,[27] G.M. Bilei,[22] D. Bisello,[21] G. Blaylock,[7]
J.R. Bogart,[27] T. Bolton,[11] G.R. Bower,[27] J.E. Brau,[20] M. Breidenbach,[27]
W.M. Bugg,[28] D. Burke,[27] T.H. Burnett,[31] P.N. Burrows,[16] W. Busza,[16]
A. Calcaterra,[13] D.O. Caldwell,[6] D. Calloway,[27] B. Camanzi,[12]
M. Carpinelli,[23] R. Cassell,[27] R. Castaldi,[23][a] A. Castro,[21] M. Cavalli-Sforza,[7]
E. Church,[31] H.O. Cohn,[28] J.A. Coller,[3] V. Cook,[31] R. Cotton,[4]
R.F. Cowan,[16] D.G. Coyne,[7] A. D'Oliveira,[8] C.J.S. Damerell,[24] M. Daoudi,[27]
R. De Sangro,[13] P. De Simone,[13] R. Dell'Orso,[23] M. Dima,[9] P.Y.C. Du,[28]
R. Dubois,[27] B.I. Eisenstein,[14] R. Elia,[27] E. Etzion,[4] D. Falciai,[22]
M.J. Fero,[16] R. Frey,[20] K. Furuno,[20] T. Gillman,[24] G. Gladding,[14]
S. Gonzalez,[16] G.D. Hallewell,[27] E.L. Hart,[28] Y. Hasegawa,[29] S. Hedges,[4]
S.S. Hertzbach,[17] M.D. Hildreth,[27] J. Huber,[20] M.E. Huffer,[27] E.W. Hughes,[27]
H. Hwang,[20] Y. Iwasaki,[29] D.J. Jackson,[24] P. Jacques,[25] J. Jaros,[27]
A.S. Johnson,[3] J.R. Johnson,[32] R.A. Johnson,[8] T. Junk,[27] R. Kajikawa,[19]
M. Kalelkar,[25] H. J. Kang,[26] I. Karliner,[14] H. Kawahara,[27] H.W. Kendall,[16]
Y. Kim,[26] M.E. King,[27] R. King,[27] R.R. Kofler,[17] N.M. Krishna,[10]
R.S. Kroeger,[18] J.F. Labs,[27] M. Langston,[20] A. Lath,[16] J.A. Lauber,[10]
D.W.G. Leith,[27] M.X. Liu,[33] X. Liu,[7] M. Loreti,[21] A. Lu,[6] H.L. Lynch,[27]
J. Ma,[31] G. Mancinelli,[22] S. Manly,[33] G. Mantovani,[22] T.W. Markiewicz,[27]
T. Maruyama,[27] R. Massetti,[22] H. Masuda,[27] E. Mazzucato,[12]

A.K. McKemey,[4] B.T. Meadows,[8] R. Messner,[27] P.M. Mockett,[31]
K.C. Moffeit,[27] B. Mours,[27] G. Müller,[27] D. Muller,[27] T. Nagamine,[27]
U. Nauenberg,[10] H. Neal,[27] M. Nussbaum,[8] Y. Ohnishi,[19] L.S. Osborne,[16]
R.S. Panvini,[30] H. Park,[20] T.J. Pavel,[27] I. Peruzzi,[13][b] M. Piccolo,[13]
L. Piemontese,[12] E. Pieroni,[23] K.T. Pitts,[20] R.J. Plano,[25] R. Prepost,[32]
C.Y. Prescott,[27] G.D. Punkar,[27] J. Quigley,[16] B.N. Ratcliff,[27] T.W. Reeves,[30]
J. Reidy,[18] P.E. Rensing,[27] L.S. Rochester,[27] J.E. Rothberg,[31] P.C. Rowson,[11]
J.J. Russell,[27] O.H. Saxton,[27] S.F. Schaffner,[27] T. Schalk,[7] R.H. Schindler,[27]
U. Schneekloth,[16] B.A. Schumm,[15] A. Seiden,[7] S. Sen,[33] V.V. Serbo,[32]
M.H. Shaevitz,[11] J.T. Shank,[3] G. Shapiro,[15] S.L. Shapiro,[27] D.J. Sherden,[27]
K.D. Shmakov,[28] C. Simopoulos,[27] N.B. Sinev,[20] S.R. Smith,[27] J.A. Snyder,[33]
P. Stamer,[25] H. Steiner,[15] R. Steiner,[1] M.G. Strauss,[17] D. Su,[27] F. Suekane,[29]
A. Sugiyama,[19] S. Suzuki,[19] M. Swartz,[27] A. Szumilo,[31] T. Takahashi,[27]
F.E. Taylor,[16] E. Torrence,[16] J.D. Turk,[33] T. Usher,[27] J. Va'vra,[27]
C. Vannini,[23] E. Vella,[27] J.P. Venuti,[30] R. Verdier,[16] P.G. Verdini,[23]
S.R. Wagner,[27] A.P. Waite,[27] S.J. Watts,[4] A.W. Weidemann,[28] E.R. Weiss,[31]
J.S. Whitaker,[3] S.L. White,[28] F.J. Wickens,[24] D.A. Williams,[7]
D.C. Williams,[16] S.H. Williams,[27] S. Willocq,[33] R.J. Wilson,[9]
W.J. Wisniewski,[5] M. Woods,[27] G.B. Word,[25] J. Wyss,[21] R.K. Yamamoto,[16]
J.M. Yamartino,[16] X. Yang,[20] S.J. Yellin,[6] C.C. Young,[27] H. Yuta,[29]
G. Zapalac,[32] R.W. Zdarko,[27] C. Zeitlin,[20] Z. Zhang,[16] and J. Zhou,[20]

[1] *Adelphi University, Garden City, New York 11530*

[2] *INFN Sezione di Bologna, I-40126 Bologna, Italy*

[3] *Boston University, Boston, Massachusetts 02215*

[4] *Brunel University, Uxbridge, Middlesex UB8 3PH, United Kingdom*

[5] *California Institute of Technology, Pasadena, California 91125*

[6] *University of California at Santa Barbara, Santa Barbara, California 93106*

[7] *University of California at Santa Cruz, Santa Cruz, California 95064*

(8) *University of Cincinnati, Cincinnati, Ohio 45221*

(9) *Colorado State University, Fort Collins, Colorado 80523*

(10) *University of Colorado, Boulder, Colorado 80309*

(11) *Columbia University, New York, New York 10027*

(12) *INFN Sezione di Ferrara and Università di Ferrara, I-44100 Ferrara, Italy*

(13) *INFN Lab. Nazionali di Frascati, I-00044 Frascati, Italy*

(14) *University of Illinois, Urbana, Illinois 61801*

(15) *Lawrence Berkeley Laboratory, University of California, Berkeley, California 94720*

(16) *Massachusetts Institute of Technology, Cambridge, Massachusetts 02139*

(17) *University of Massachusetts, Amherst, Massachusetts 01003*

(18) *University of Mississippi, University, Mississippi 38677*

(19) *Nagoya University, Chikusa-ku, Nagoya 464 Japan*

(20) *University of Oregon, Eugene, Oregon 97403*

(21) *INFN Sezione di Padova and Università di Padova, I-35100 Padova, Italy*

(22) *INFN Sezione di Perugia and Università di Perugia, I-06100 Perugia, Italy*

(23) *INFN Sezione di Pisa and Università di Pisa, I-56100 Pisa, Italy*

(25) *Rutgers University, Piscataway, New Jersey 08855*

(24) *Rutherford Appleton Laboratory, Chilton, Didcot, Oxon OX11 0QX United Kingdom*

(26) *Sogang University, Seoul, Korea*

(27) *Stanford Linear Accelerator Center, Stanford University, Stanford, California 94309*

(28) *University of Tennessee, Knoxville, Tennessee 37996*

(29) *Tohoku University, Sendai 980 Japan*

(30) *Vanderbilt University, Nashville, Tennessee 37235*

(31) *University of Washington, Seattle, Washington 98195*

(32) *University of Wisconsin, Madison, Wisconsin 53706*

(33) *Yale University, New Haven, Connecticut 06511*

† *Deceased*

[a] *Also at the Università di Genova*

[b] *Also at the Università di Perugia*

References

[1] H. Fritzsch, M. Gell-Mann and H. Leutwyler, *Phys. Lett.* **B47** (1973) 365,
D. J. Gross and F. Wilczek , *Phys. Rev. Lett.* **30** (1973) 1343,
H. Politzer, *Phys. Rev. Lett.* **30** (1973) 1346.

[2] Ya. I. Azimov, Yu. L. Dokshitzer, V. A. Khoze, and S. I. Troyan, *Zeit. Phys.* **C27** (1985) 65.

[3] See e.g. A. DeAngelis, CERN-PPE/90-129.

[4] See e.g. F. Halzen and A. Martin *Quarks and Leptons: An Introductory Course in Modern Particle Physics* J. Wiley and Sons, 1984.

[5] The Particle Data Group, *Phys. Rev.* **D50**, Part I (1994).

[6] B. W. Lynn and C. Verzegnassi, *Phys. Rev.* **D35** (1987) 3326.

[7] P. Clarke, *RAL-90-055* (1990).

[8] A. Lath, Ph.D Thesis, Mass. Institute of Technology (1994), *SLAC Report 454.*

[9] SLD Collaboration: K. Abe *et al.*, *SLAC-PUB-95-7000*, (1995).

[10] A. Blondel, B. W. Lynn, F. M. Renard, and C. Verzegnazzi, *Nucl. Phys.* **B304** (1988) 438.

[11] M. Hildreth, Ph.D Thesis, Stanford University (1995), *SLAC Report 458*,
SLD Collaboration: K. Abe *et al.*, SLAC-PUB-6687, *Submitted to Phys. Rev D.*

[12] D. C. Williams, Ph.D Thesis, Mass. Institute of Technology (1994), *SLAC Report 445*,
SLD Collaboration: K. Abe *et al.*, Phys. Rev. Lett. **74** (1995) 2895.

[13] M. Gell-mann, *Phys. Lett.* **8** (1964), 214.
G. Zweig, *CERN 8409/TH* (1964).

[14] M. Y. Han and Y. Nambu, *Phys. Rev.* **139B** (1965) 1006.

[15] E. Bloom *et al.*, *Phys. Rev. Lett.* **23** (1969) 930.
M. Breidenbach *et al.*, *Phys. Rev. Lett.*, **23** (1969) 935.

[16] G. Hansen *et al.*, *Phys. Rev. Lett.* **35** (1975)1609.

[17] TASSO Collaboartion: R. Brandelik *et al.*, *Phys. Lett.* **B86** (1979) 243.

[18] SLD Collaboration: K. Abe *et al*, *Phys. Rev.* **D51** (1995) 962.

[19] J. Lauber, Ph.D Thesis, University of Colorado (1993), *SLAC Report 413*, SLD Collaboration: K. Abe. *et al.*, *Phys. Rev. Lett.* **71** (1993) 2528.

[20] T. Sjostrand, *Comp. Phys. Comm.* **39** (1986), 347.

[21] J. Ellis, M. K. Galliard,G. C. Ross, *Nucl. Phys.* **B111** (1976) 253.

[22] A. Ali *et al.*, *Nucl. Phys.* **B167** (1980) 229.

[23] K. J. F. Gaemers, J. A. M. Vermaseren, *Z. Physik* **C7** (1980) 81.

[24] G. Altarelli and G. Parisi, *Nucl. Phys.* **B126** (1977), 298.

[25] R. D. Field and R. P. Feynmann, *Nucl. Phys.* **B136** (1992), 1.

[26] F. E. Page and S. D. Protopopescu, in *Physics of the Superconducting Supercollider-1986* (1987) 320.

[27] X. Artru and G. Mennessier *Nucl. Phys.* **B70** (1974) 93.

[28] B. Anderson *et al.*, *Z. Phys.* **C1** (1979) 105.

[29] B. Anderson *et al.*, *Phys. Reports* **97** (1983) 33.

[30] B. Foster(ed), *Electron-Positron Annihilation Physics*, 1990.

[31] T. Sjostrand, M. Bengtsson, *Comp. Phys. Commun.* **43** (1987) 3.

[32] G. Marchesini, B. R. Webber, *Nucl. Phys.* **B310** (1988) 453.

[33] Yu. L. Dokshitzer, V. S. Fadin, and V. A. Khoze, *Zeit. Phys.* **C18** (1983) 37.
Ya. I. Azimov, Yu. L. Dokshitzer, V. A. Khoze, and S. I. Troyan, *Zeit. Phys.* **C31** (1987) 213.
Yu. L. Dokshitzer, V. A. Khoze, A. H. Mueller and S. I. Troyan, *Basics of Perturbative QCD* Editions Frontieres, (1991).
Yu. L. Dokshitzer, V. A. Khoze, and S. I. Troyan, *Z. Phys.* **C55** (1992) 107.

[34] A summary of these measurements may be found in N. Brummer, Ph.D. Thesis, Leiden, *NIKHEF-H* RX-1473 (1994).

[35] D. Dupen, *SLAC-62*, (1966).

[36] M. Swartz, *SLAC-PUB-4656* (1988).

[37] SLD Collaboration: K. Abe *et al.*, *Phys. Rev. Lett.*, **70** (1993) 2515.

[38] SLD Collaboration: K. Abe *et al.*, *Phys. Rev. Lett.*, **73** (1995) 24.

[39] SLD Collaboration: G. Agnew *et al.*, *SLD Design Report* SLAC-0273 (1984).

[40] K. Pitts, Ph.D Thesis, University of Oregon (1994), *SLAC Report 446*.

[41] M. Strauss, *SLAC Pub 6686* (1994).

[42] M. Hildreth *et al.*, *SLAC Pub 6656* (1994).

[43] T. Pavel, Ph.D Thesis, Stanford University (1996), in preparation.

[44] S. Willocq *et al.*, **SLAC-6693**, (1995).

[45] SLD Collaboration: K. Abe *et al.*, *Nucl. Inst. and Meth.* **A328** (1993) 472.

[46] SLD Collaboration: K. Abe *et al.*, *Nucl. Instr. and Meth.* **A300** (1991) 501.

[47] P. Jacques *private communication.*

[48] P. N. Burrows *et al.*, *SLD Note 229* (1993) (unpublished).

[49] R. Brun *et al.*, *CERN DD/EE/84-1* (1987).

[50] P. N. Burrows, *Z. Phys.* **C41** (1988) 375.

[51] OPAL Collaboration: M. Z. Akrawy *et al.*, *Z. Phys.* **C55** (1990) 505.

[52] P. N. Burrows and H. Masuda, *SLD Physics Note 36* (1995) (unpublished).

[53] C. Peterson *et al.*, *Phys. rev.* **D27** (1983) 105.

[54] SLD Collaboration: K. Abe *et al.*, *Phys. Rev.* **D53** (1996) 1023.

[55] K. Hayes, in *Proceedings of the Third MarkII Workshop on SLC Physics*, SLAC-315 (1987).

[56] Mark II Collaboration: R. G. Jacobsen *et al.*, *Phys. Rev. Lett.* **67** (1991) 3347.

[57] R. G. Jacobsen, Ph.D. Thesis, Stanford University (1991), *SLAC Report 381.*

[58] H. A. Neal, Jr. II, Ph.D Thesis, Stanford University (1995), *SLAC Report 473.*

[59] *CERN D506 - Version 92.1* (March 1992).

[60] SLD Collaboration: K. Abe, et al., Phys. Rev. Lett. **72** (1994).

[61] ALEPH Collaboration: D. Buskulic *et al.*, *Z. Physik* **C64** (1994) 361.
DELPHI Collaboration: P. Abreu *et al.*, *Z. Physik* **C65** (1995) 587.
OPAL Collaboration: R. Akers *et al.*, CERN-PPE/95-024 *submitted to Z. Physik C* (1995).
L3 Collaboration: M. Acciarri *et al.*, *Phys. Lett.* **B328**(1994) 223.

[62] ALEPH Collaboration: D. Buskulic *et al.*, *Z. Physik* **C64** (1994) 361.
DELPHI Collaboration : P. Abreu *et al.*, *Phys. Lett.* **B318** (1993) 249.
OPAL Collaboration: R. Akers *et al.*, OPAL Physics Note PN138 (1995) (unpublished).
L3 Collaboration: M. Acciarri *et al.*, *Phys. Lett.* **B328** (1994) 223.

[63] DELPHI Collaboration: P. Abreu *et al.*, CERN-PPE-95/28 (1995), *submitted to Nucl. Phys. B.*

[64] DELPHI Collaboration: P. Abreu *et al.*, CERN-PPE-96/06 (1996).